

Article

Hydrophilicity Affecting the Enzyme-Driven Degradation of Piezoelectric Poly-L-Lactide Films

Lea Gazvoda ^{1,2}, Bojana Višić ^{3,4}, Matjaž Spreitzer ¹ and Marija Vukomanović ^{1,*} 

¹ Advanced Materials Department, Jožef Stefan Institute, 1000 Ljubljana, Slovenia; lea.udovc@ijs.si (L.G.); matjaz.spreitzer@ijs.si (M.S.)

² Jožef Stefan International Postgraduate School, 1000 Ljubljana, Slovenia

³ Condensed Matter Physics Department, Jožef Stefan Institute, 1000 Ljubljana, Slovenia; bojana.visic@ijs.si

⁴ Institute of Physics Belgrade, University of Belgrade, Pregrevica 118, 11080 Belgrade, Serbia

* Correspondence: marija.vukomanovic@ijs.si; Tel.: +386-1-477-3547

Abstract: Biocompatible and biodegradable poly-L-lactic acid (PLLA) processed into piezoelectric structures has good potential for use in medical applications, particularly for promoting cellular growth during electrostimulation. Significant advantages like closer contacts between cells and films are predicted when their surfaces are modified to make them more hydrophilic. However, there is an open question about whether the surface modification will affect the degradation process and how the films will be changed as a result. For the first time, we demonstrate that improving the polymer surface's wettability affects the position of enzyme-driven degradation. Although it is generally considered that proteinase K degrades only the polymer surface, we observed the enzyme's ability to induce both surface and bulk degradation. In hydrophilic films, degradation occurs at the surface, inducing surface erosion, while for hydrophobic films, it is located inside the films, inducing bulk erosion. Accordingly, changes in the structural, morphological, mechanical, thermal and wetting properties of the film resulting from degradation vary, depending on the film's wettability. Most importantly, the degradation is gradual, so the mechanical and piezoelectric properties are retained during the degradation.

Keywords: poly-L-lactic acid; enzymatically catalyzed degradation; piezoelectricity; bulk erosion; surface erosion



Citation: Gazvoda, L.; Višić, B.; Spreitzer, M.; Vukomanović, M. Hydrophilicity Affecting the Enzyme-Driven Degradation of Piezoelectric Poly-L-Lactide Films. *Polymers* **2021**, *13*, 1719. <https://doi.org/10.3390/polym13111719>

Academic Editor: Roman A. Surmenev

Received: 29 April 2021
Accepted: 21 May 2021
Published: 24 May 2021

Publisher's Note: MDPI stays neutral with regard to jurisdictional claims in published maps and institutional affiliations.



Copyright: © 2021 by the authors. Licensee MDPI, Basel, Switzerland. This article is an open access article distributed under the terms and conditions of the Creative Commons Attribution (CC BY) license (<https://creativecommons.org/licenses/by/4.0/>).

1. Introduction

Poly-L-lactic acid (PLLA), a biosynthetic thermoplastic polyester, is widely used in the biomedical field because it is biocompatible and biodegradable [1,2]. It can also be formed into different shapes (2D coatings and films, micro- and nano-powders, 3D scaffolds, etc.) with different properties, depending on the requirements [3]. Accordingly, PLLA is used in drug-delivery systems [4], tissue engineering [5], wound dressing [6], implantation [7] and many more [8,9].

A very poorly explored and particularly important aspect of PLLA's application in biomedicine is associated with the possibility of processing it into a piezoelectric material. Due to its helix structure, PLLA exhibits shear piezoelectricity [10]. When PLLA is oriented and crystalline, usually as fibers or films, the chains are strained, the molecular dipoles are aligned, and a voltage difference is observed [11]. Such a structure, formulated as a piezoelectric scaffold, can be applied for piezo-stimulation and promoting cell proliferation. The low piezoelectric effect of PLLA (compared to piezoceramics) is comparable to the piezoelectricity of natural biomacromolecules (i.e., collagen) [12] and can be efficient enough to relate with biological systems [13]. It makes this polymer particularly appropriate for regenerative medical use to accelerate the wound-healing process. When applied for wound healing, the safe biodegradation of piezoelectric PLLA films is very important. The process needs to be steady, and the biodegradation (followed by a change of mechanical,

structural, morphological and piezoelectric properties) should follow the kinetics of the tissue regeneration so that at the end, no material residues are left in the system when the new tissue is formed.

When PLLA is in contact with biological media, cleavage of the ester bonds occurs in the bulk matter, usually by hydrolysis, into lactic acid, carbon dioxide and water [14]. Under in vivo conditions, due to the inflammation process during the injury, the degradation process is enhanced by the enzymes present that degrade the polymer matrix [1]. Since PLLA is more hydrophobic, swelling of the polymer film occurs with the diffusion of water inside the polymer bulk, which triggers the degradation inside the material [14]. However, when enzymes are present, it is generally considered that surface degradation is favorable since the diffusion of enzymes inside the film is aggravated [15]. Proteinase K catalyzes the degradation of PLLA several times faster in amorphous than in crystalline regions [16]. At the surface, degradation is limited to just the amorphous parts [15]. Crystalline residues, remaining after the degradation of the connected amorphous areas, are released into the surrounding liquid medium or accumulate on the surface and increase crystallinity [15]. Polymer crystallinity and chain orientation have been determined to have an important role in the process of enzyme-induced PLLA degradation. H. Tsuji et al. showed that the initially higher crystallinity of the PLLA films slows the degradation process and that the higher polymer-chain orientation also limits the enzyme intake into the bulk [15]. In addition, Rangari et al. observed that during the hydrolysis of the amorphous part on the surface in uniaxially prepared crystalline PLLA films, crystallinity plays the dominant role in determining the extent of the degradation, compared to the orientation of the polymer chains [16].

Understanding the degradation mechanism in biologically relevant surroundings is a key issue for using a piezoelectric polymer in biomedical applications. Although there is a detailed study of the structural changes that follow enzymatic degradation (change in crystallinity, chain orientation, chain mobility, etc.), very little knowledge is available on the change in the piezoelectric and mechanical properties of PLLA films during the degradation process. All the information regarding PLLA degradation is available for polymers with a hydrophobic surface. However, the hydrophobic surface is the main disadvantage of PLLA, potentially resulting in a low cell affinity and an inflammatory response [17]. A particular lack of information was observed for the case of the degradation of surface-modified PLLA hydrophilic films. With that in mind, we focused our investigations on two questions:

- (i) How will the degradation be affected if the surface of the PLLA film is modified from hydrophobic to hydrophilic (more favorable to cells)?
- (ii) What will happen to the mechanical and piezoelectric properties of the PLLA once the film is immersed in a liquid medium containing proteinase K (as an imitation of the inflammation response at the site of a wound)?

Therefore, in this study, we compare the enzymatically catalyzed degradation process of a uniaxial drawn piezoelectric PLLA film with and without surface modification, and with it the mechanical and piezoelectric changes that occur during the degradation process to achieve a more stable and gradual loss of piezoelectric properties during the process. Films with improved wettability should have greater potential for medical applications due to the proposed better affinity of the cells for the film.

2. Materials and Methods

2.1. Materials

Poly-L-lactic acid (PLLA) having a molecular weight with an approximate value of 150 kDa (Goodfellow, Cambridge, Ltd., UK), bovine serum albumin (BSA) (Fisher scientific, Leics, UK), methylene blue (MB) (Alfa Aesar, Thermo Fisher GmbH, Kandel, Germany) were used. Enzyme proteinase K was purchased from ITW Reagents (AppliChem GmbH, A3830,0500, Darmstadt, Germany) and was used as received. TRIS buffer, sodium hydroxide (NaOH), methanol (MeOH), hydrochloride acid (HCl), were purchased from

Sigma-Aldrich Chemie GmbH, Steinheim, Germany. Distilled water was purified using a Milli-Q system (Purelab Option-Q, ELGA, High Wycombe, UK).

2.2. Processing PLLA Films

Piezoelectric polymer films were prepared using the following procedure, optimized in our previous study [18]. PLLA granules (1 g) were melt-pressed between two metal plates at 200 °C under a pressure of 56 kN for 3 min and immediately quenched in cold water (4 °C) (amorphous sheet). To prepare piezoelectric films, the amorphous sheet was cut into a dumbbell-shape film and uniaxially stretched with a homemade tensile stretcher to a draw ratio of 5 at a temperature above the glass transition (90 °C), using a drawing rate of 40 mm/min. Surface modification, such as alkaline etching, was performed to prepare hydrophilic films. Films were submerged overnight in a 0.04 M NaOH medium, prepared in a water/MeOH mixture (70/30 V/V) to cleave the ester bonds on the surface.

2.3. Enzymatic Degradation

The drawn films were immersed in 0.1 mg/mL proteinase K solution with pH 8.5. The enzyme solution was prepared using a 0.5 M TRIS buffer, adding HCl to adjust the pH value. 5 mL of enzyme solution containing films was maintained at 37 °C in a water bath while gently shaken. The degradation study was carried out for 10 days. Films were washed with water and left to dry before the analyses. Enzymatic activity during the degradation process was monitored using an absorbance multiplate reader (Synergy H1, BioTek, Bad Friedrichshall, Germany). A sample of 500 µL of enzymatic medium taken from the degrading sample was added to 500 µL of 1 mg/mL BSA protein and digested for 2 h. Absorbance at 290 nm was continuously measured to determine the half-time needed for protein degradation. Measurements were made in two parallel samples for enzymes with different polymer films and a bare enzyme. Further enzymatic activity was stopped by heating the sample at 90 °C. A total of 15 µL of the sample with 3 µL of added loading buffer were put on 15% polyacrylamide gel to separate the degraded BSA proteins based on size using SDS-page electrophoresis.

2.4. Characterization Methods

Gravimetric determination, crystallinity and orientation changes were calculated using the following equation:

$$\Delta X (\%) = 100\% \times (X_{t0} - X_t) / X_{t0}, \quad (1)$$

where ΔX represents the weight changes (w), crystallinity (X) and orientation ratio (D) from the beginning (t_0) to a certain time of degradation (t).

Orientation was determined using a Fourier-transform infrared spectrometer in attenuated total reflectance (ATR) mode (PerkinElmer Spectrum 100, Waltham MA, USA). Spectra were recorded in the 600–4000 cm^{-1} wavenumber range with a spectral resolution of 4 cm^{-1} and the accumulation of 10 spectra using a polarizer. Changes in the orientation were determined using the previous equation, where D represents the ratio between changes of the vertical (\parallel) and horizontal (\perp) absorbance (A) of the C=O peak (1756 cm^{-1}) using the following equation [19,20]:

$$D = A_{\parallel} / A_{\perp}. \quad (2)$$

Crystallinity was determined using a NETZSCH STA 449 (Jupiter) thermal analyzer for differential scanning calorimetry (DSC) in an Ar/O atmosphere (40/10). A total of 3–4 mg of each sample were put in platinum crucibles and heated from 40 °C to 200 °C with a 20 °C/min heating rate due to the temperature calibration under these conditions. The enthalpy of cold crystallization (ΔH_c) and the enthalpy of melting (ΔH_m) were determined

by calculating the surface under the peak of the crystallization or melting, respectively. Bulk crystallinity was determined with the following expression:

$$\chi_c (\%) = 100\% \times (\Delta H_m - \Delta H_c) / \Delta H_{100\%}, \quad (3)$$

where the value for $\Delta H_{100\%}$ is taken as 93.6 J/g, which is a theoretical value for 100% crystalline PLLA films in the α crystalline form [21].

Morphological changes during degradation were observed with a scanning electron microscope (JSM-7600 F, Jeol Ltd., Tokyo, Japan). To observe changes in the hydrophilic properties, methylene-blue staining was used to observe the color change due to more carboxylic groups on the surface [22]. Water wetting angles were measured using a Theta Lite contact-angle meter, Biolin Scientific.

Dynamic mechanical properties of the PLLA samples were studied under tension mode on the films in a rectangular shape (9 mm long, 3–3.5 mm wide and 0.1 mm thick). The measurements were performed with a Mettler Toledo DMA/SDTA861e. The dynamic responses were tested from 0 °C to 130 °C at the heating rate of 3 K/min. The dynamic force amplitude was 1 N, and the validity of Hooke's law (linearity measurement) was tested on every sample to determine the displacement amplitude, which was 2–5 μm . The chosen frequency was 1 Hz. The storage modulus, loss modulus and $\tan \delta$ were recorded as a function of the sample temperature. Since the measurements were made in the tension mode, the storage modulus corresponds to Young's modulus.

The piezoelectric properties were measured according to the description in a previous article [18]. Polymer films were cut at an angle of 45° from the stretching axis, seeing that the shear stress has a maximum value when measured at this angle [23]. The measurement was made using a PiezoMeter System PM300 (Piezotest Pte. Ltd., International Plaza, Singapore), which was adapted for thin-film d_{31} measurements. First, gold electrodes were sputtered on both surfaces of the polymer film. Then the film was clamped on both sides to stretch the film (frequency of 110 Hz and force 0.15–0.5 N). The voltage was measured with a voltmeter (Tenma multimeter) over a reference capacitor of 1000 pF. The piezoelectric coefficients g_{14} and d_{14} were calculated.

3. Results

PLLA films were made with a hydrophilic surface using alkali etching to improve their water wettability, which is favored for interactions with cells [24]. Before being applied for the degradation study, the stretched, oriented, and etched films remained stained after immersion in the methylene-blue solution, indicating a larger amount of carboxylic end groups on the surface (Figure 1a). Degradation was performed using a proteinase-K-buffered solution under simulated physiological conditions (gently shaking at 37 °C). After aging for 5 and 10 days in the enzyme solution, the polymeric films had macroscopically observable damage (Figure 1b). Normally, for PLLA polymers, proteinase K acts as a hydrolysis catalyzer, and degradation follows the surface mechanism [15]. For the case of non-etched, hydrophobic films, we initially observed the occurrence of surface erosion, along with some evidence of bulk erosion induced by autocatalysis (day 10). This result was more following the available literature on hydrophobic PLLA film degradation without any enzyme present [17]. However, in the case of more hydrophilic PLLA films, it was observed that the films were macroscopically more compact, without signs of bulk erosion, indicating a contribution of the surface modification to the degradation process and the following mechanism (Figure 1b).

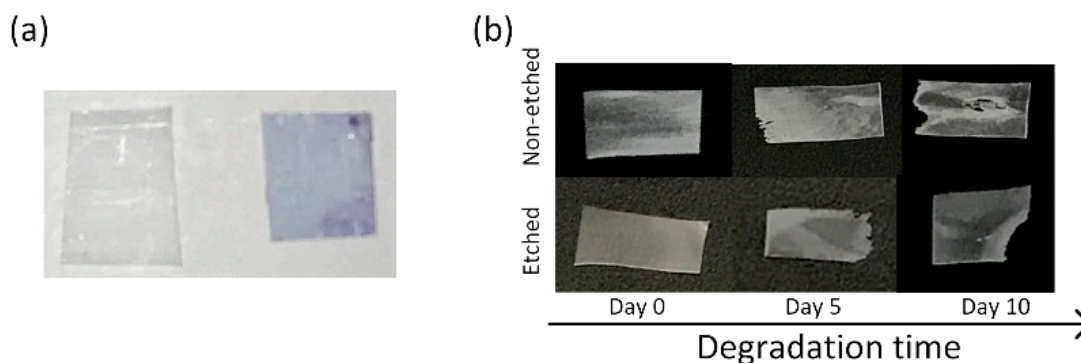


Figure 1. (a) Methylene blue staining of non-etched (left) and etched (right) PLLA films; (b) samples of enzymatic degradation of the non-etched (top) and etched (bottom) films after 0, 5 and 10 days.

3.1. Enzymatic Activity

Since all of the polymeric films were degraded in the same solution for the whole 10 day period, the enzyme activity was periodically monitored to follow the progress of degradation. By lowering the pH value, as a result of the release of lactic acid residues into the medium during the degradation progress, the activity of the proteinase K was also expected to decrease. The detected degradation products (based on an SDS-page test) (Figure 2a) and the half time of the enzyme's degradation activity (Figure 2b) show a lowering of the activity along with the film's degradation. The enzyme activity was also decreased in a reference enzyme solution (without films); however, this drop was more pronounced when films were present. Figure 2c presents the activity of the initial enzyme solution with the reference BSA protein, observed with a continuous absorbance measurement, from where the half time of the total protein degradation was determined. After 10 days of degradation, the enzyme activity is significantly reduced compared to day 1 (from 5 to 50 min), even without the films being present. This was expected since no fresh enzymes were added during the degradation. Despite the observed decreases, it should be noted that the enzyme was active for the whole period during which the degradation progress was observed. Accordingly, all the observed changes in the aged PLLA films could be assigned to the process of degradation.

3.2. Structural Changes (Crystallinity and Orientation)

After 10 days of degradation, the weight losses, indicating the progress of the degradation, were similar for both the etched (35%) and non-etched (37%) films. Additionally, the drops in the pH, directly correlated with the degradation process, were comparable for the etched and non-etched films (from 8.5 to 4.6) since the equally released lactic acid residues lower the initial pH value. The initial hydrophilicity was changed only on the surface of the films, which could affect the location of the degradation; however, the total progress of the degradation remained the same.

The main differences in the degradation of the etched and non-etched films were the crystallinity and orientation. These properties were detected by comparing the FTIR spectra of the enzymatically degraded films with the spectra of the film reference (corresponding to films aged in a medium without the enzyme present), as presented in Figure 3. Typical changes in the surface crystallinity are observed closely at normalized spectra in the wavelength range $900\text{--}980\text{ cm}^{-1}$. Following previous studies [16,18], the increase in the intensity of the peak at 922 cm^{-1} represents an increase in the crystallinity of the PLLA, which we also observed in the case of the non-etched (hydrophobic) films (Figure 3, left).

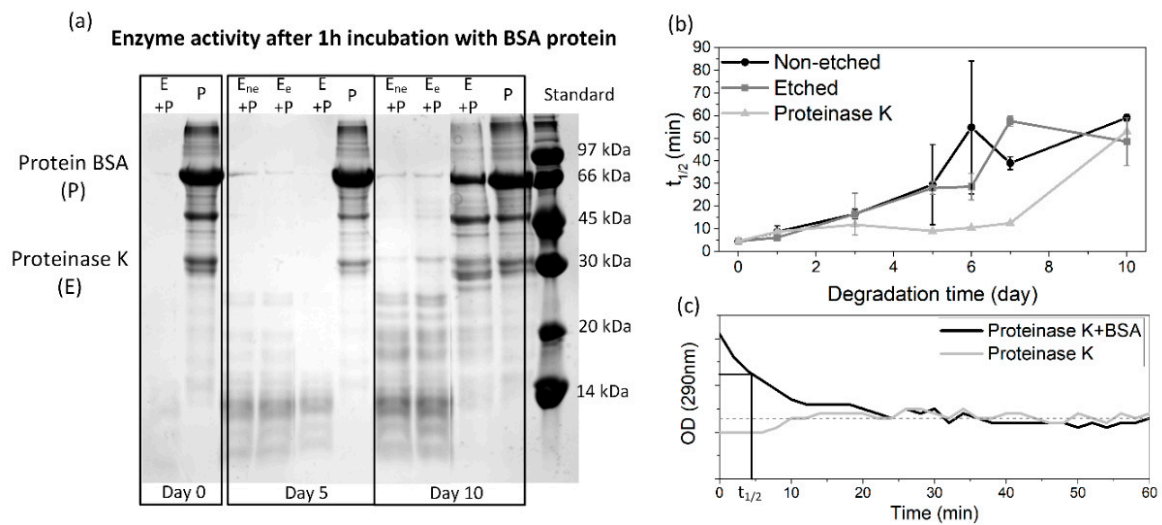


Figure 2. (a) SDS-page results for the enzymatic activity of the initial solution and after 5 and 10 days of degradation for enzymes in non-etched (E_{ne}), etched (E_{ee}) and control solutions (E), where activity was verified with degradation of the BSA protein (P); (b) calculated half time needed for BSA protein degradation for enzymes in non-etched, etched and control solutions, determined from measured optical density at 290 nm for each solution, where graph (c) presents the absorbance measurements for initial proteinase K solution with a marked half time of total degradation ($t_{1/2}$).

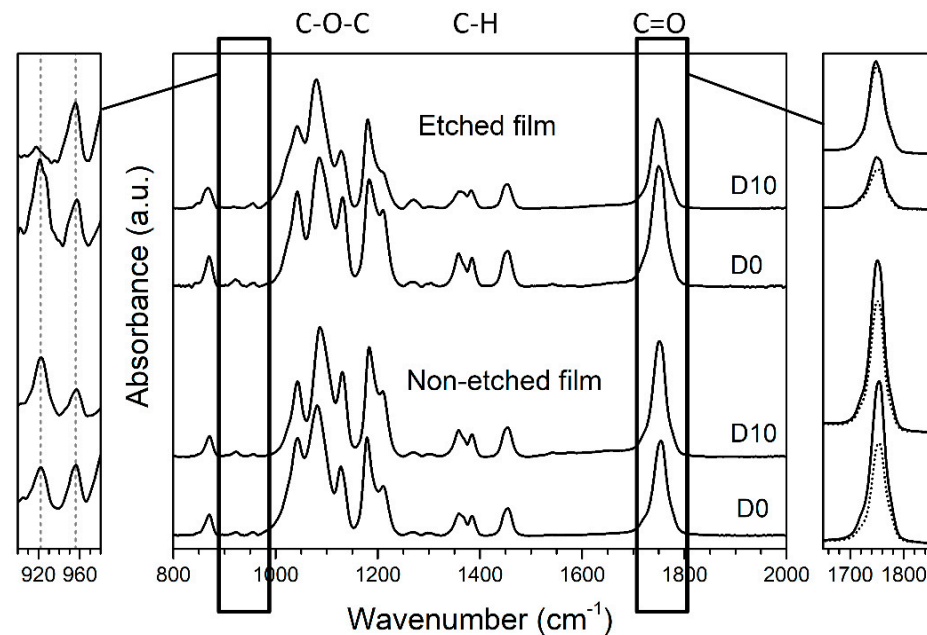


Figure 3. ATR FT-IR spectra (normalized to maximum peak absorbance) for non-etched and etched PLLA films (middle), degraded for 10 days in enzymatic solution (D10), compared to initial PLLA film (D0). On the (left), an enlarged, normalized spectrum between 900 and 980 cm⁻¹ is presented to observe changes in the intensity of peaks that are specific for more crystalline (921 cm⁻¹) or more amorphous (956 cm⁻¹) films. On the (right), a polarizer was used to determine the changes in orientation of the C=O peak, comparing the intensities of horizontal (solid line) and vertical (dotted line) orientations without normalization of the spectra.

Orientation for the polymeric chains within the film was confirmed based on an observable peak at 1755 cm⁻¹ that corresponds to the C=O stretching in the ester carbonyl group. As noted earlier, high anisotropy is obtained for oriented polymeric films when comparing the vertical and horizontal positions [19]. For our oriented PLLA films, the intensities of the C=O and C–O–C peaks are enhanced in the drawing direction (horizontal)

compared to the perpendicular direction (vertical) and shifted to slightly lower values (Figure 3, right). Comparable changes in the C=O and C–O–C peaks were also observed by T. Nobeshima et al. [20]. Regarding the influence of the water wettability, the orientation was decreased for both the hydrophobic non-etched and hydrophilic etched films during degradation (Table 1 and Figure 3).

Table 1. Summarized properties of degraded PLLA films over 10 days in solution with proteinase K.

Up to 10 Days of Degradation	PLLA Non-Etched	PLLA-Etched
pH change	From 8.5 to 4.6	From 8.5 to 4.6
Weight loss	37 wt %	35 wt %
Crystallinity change (DSC)	+27%	+5%
Orientation change (FT-IR: 1750 cm^{-1})	−24% of the initial ratio	−18% of the initial ratio
Piezo change	After 5 days:	After 5 days:
d_{14}	2.68 pC/N (68.8% of initial)	2.32 pC/N (50.4% of initial)
g_{14}	0.092 Vm/N	0.066 Vm/N
	After 10 days	After 10 days
d_{14}	Non-measurable with applied method	Non-measurable with applied method
g_{14}	Non-measurable with applied method	Non-measurable with applied method

Similar structural changes were revealed during the XRD study (Figure 4). As with the FTIR analysis, the XRD results clearly indicate the large increase in crystallinity of the non-etched samples. The polymer is in the α' phase since the specific (200)/(110) peak appears at the 2-theta position lower than 16.6° , following a previous report [25]. After 10 days, the additional, more ordered α phase is observed only for the etched film, detected as an additional XRD peak at 16.9° (Figure 4b).

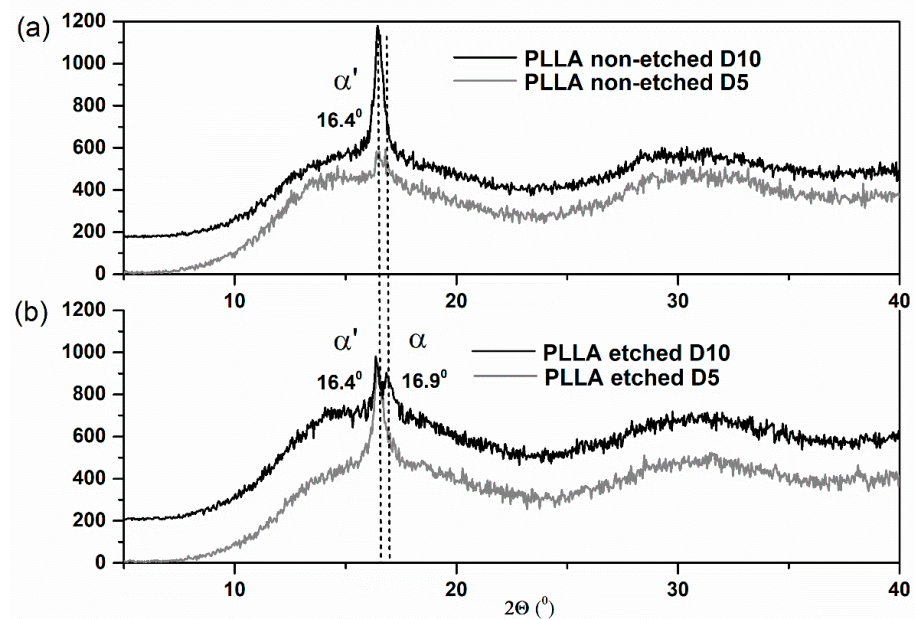


Figure 4. XRD patterns of hydrophobic non-etched (a) and hydrophilic etched (b) PLLA films obtained after 5 and 10 days of degradation by proteinase K (labeled with D5 and D10).

Investigating the thermal properties of PLLA films also revealed different responses to enzyme-catalyzed degradation for the etched and non-etched samples (Table 1, Table 2 and Figure 5). For the etched samples, the melting peaks are broad for all the measured

samples, indicating the presence of both crystalline forms: α' and α . Degradation promotes recrystallization (α' to α) since they are both detected in the final degradation stage, as seen in the XRD data. The crystallinity of the etched films, measured using DSC, is initially high (since etching removes part of the amorphous regions), and it was not changed much during the degradation. However, for non-etched samples, even though it starts at a lower value, the crystallinity increased significantly after 10 days of degradation, as also observed from the FTIR and XRD analyses. While the glass and melting temperatures (T_g and T_m) were shifted for non-etched films during degradation, similar changes were not observed in the etched films. H. Tsuji et al. also observed increased T_g values for the oriented and un-oriented films; therefore, T_g changes respond to the degradation process, like changes in the highly ordered structure, such as crystallinity or orientation [15].

Table 2. DSC data for etched and non-etched PLLA films for different periods of degradation.

Up to 10 Days of Degradation	T_g	ΔH cryst. (J/g)	T_c	ΔH melt (J/g)	T_m	Crystallinity %
PLLA-non-etched	69 °C	21	117 °C	51	173 °C	31
PLLA-non-etched D5	72 °C	35	118 °C	50	173 °C	16
PLLA-non-etched D10	75 °C	/	/	55	167 °C	58
PLLA-etched	71 °C	/	/	49	172 °C	52
PLLA-etched D5	72 °C	/	/	57	170 °C	61
PLLA-etched D10	72 °C	5	109 °C	59	170 °C	57

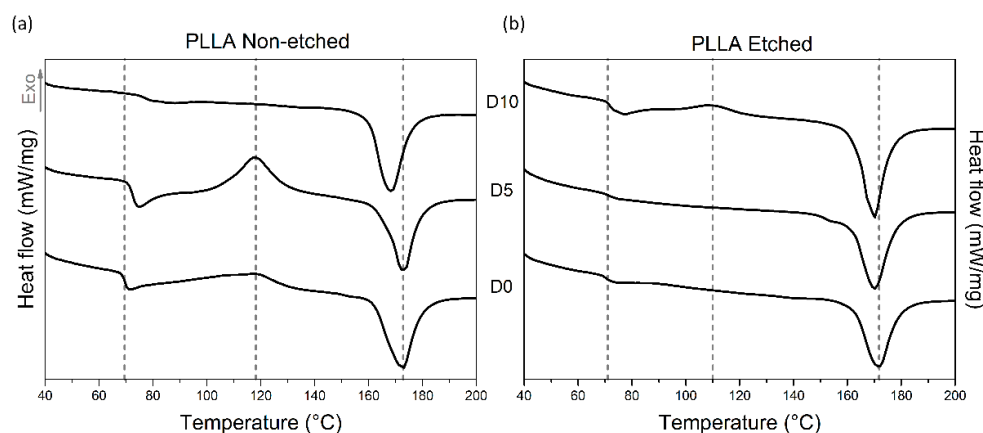


Figure 5. DSC curves of hydrophobic non-etched (a) and hydrophilic etched (b) PLLA films obtained after different periods of degradation by proteinase K, labeled by D0, D5 and D10.

3.3. Mechanical Properties

DMA measurements were performed for degraded samples to determine the changes in the mechanical properties. Since the non-etched films were very torn and porous after 10 days of degradation, measurements were not feasible. Therefore, the mechanical properties were measured only for the 5 day degradation period. On the other hand, in the case of the hydrophilic etched films, the compactness of the film was less damaged by degradation, so the mechanical measurements were normally made after 5 and 10 days of degradation.

Both etched and non-etched PLLA films have the same initial Young's modulus measured at 23 °C (2.4 GPa), comparable to values observed in the literature for PLA polymer [26], which confirms that alkali etching was performed only on the surface without compromising the inner parts (Figure 6a). After the enzymatic degradation, the values are significantly lowered for the non-etched samples, even after 5 days of degradation,

where the modulus is lowered by 92% (190 MPa), while it is only 1% for the etched samples (Figure 6a). As the degradation induces swelling and increased porosity in the bulk of the hydrophobic films (where degradation occurs), they cause a drop in the mechanical properties (observed through a drop in the storage modulus). These changes are not so pronounced in the case of the etched films before and after degradation since the dominant degradation events are taking place at the surface. In the case of the etched, hydrophilic PLLA films, Young's modulus drop occurs very slowly, only 16% for a degradation time of 10 days, clearly showing the lack of dominant bulk-erosion effects observed in non-etched films.

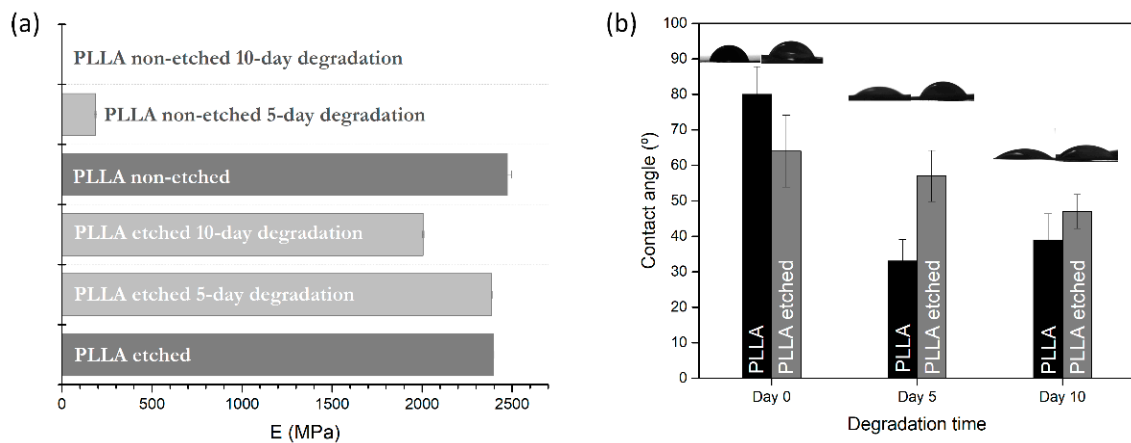


Figure 6. (a) changes in Young's modulus (at 23 °C) and (b) changes in wetting angle for water drop on polymer, for non-etched and etched samples after 0, 5 and 10 days of degradation.

3.4. Wetting-Angle Changes

Contact-angle measurements were made for pristine films and the films obtained after degradation. Interesting changes were observed for the non-etched films, where the wetting angle decreases more drastically than for the etched sample after 5 and 10 days of degradation (Figure 6b).

Alkali etching improved the hydrophilicity of the polymer surface by 25%, which resulted in more carboxylic end groups on the surface. During the degradation, a small lowering (−20%) of the initial wetting angle was observed in the etched films. The change could be associated with the change in the roughness observed in the SEM images for the etched films. On the other hand, due to the significant increase in the roughness and porosity of the non-etched hydrophobic films after degradation, their wetting angles decreased by 50%.

3.5. Piezoelectric Properties

Piezoelectric properties are highly dependent on the polymeric structure, the orientation of the polymer chains and the degree of crystallinity. Therefore, it was expected that the previously observed changes would affect them. According to those changes, proteinase-K-induced changes in the piezoelectric properties were lowered to 68% of the initial values for the non-etched sample and 50% for the etched polymer films (Table 1) after 5 days of aging. Further measurements after 10 days of degradation could not be performed since the degradation, with a mechanically unstable and porous film over the whole surface, did not allow measurements using the applied method.

3.6. Morphological Properties

After 10 days of degradation for the non-etched hydrophobic films, the main changes were observed in the cross-sections that reveal their inner (bulk) parts (Figure 7(a2,a3,b2,b3)). The initially dense and smooth layered structure in the cross-section of the starting films

before degradation (Figure 7(a2,a3)) turned into a porous, sphere-like structure obtained after the degradation progressed (Figure 7(b2,b3)). Both surfaces of the films, before and after the degradation (Figure 7(a1,b1)), are generally smooth, with a bubble structure observed on top of the degraded samples (Figure 7(b1)), indicating degradation events inside the film's bulk, such as progressive and intensive water swelling.

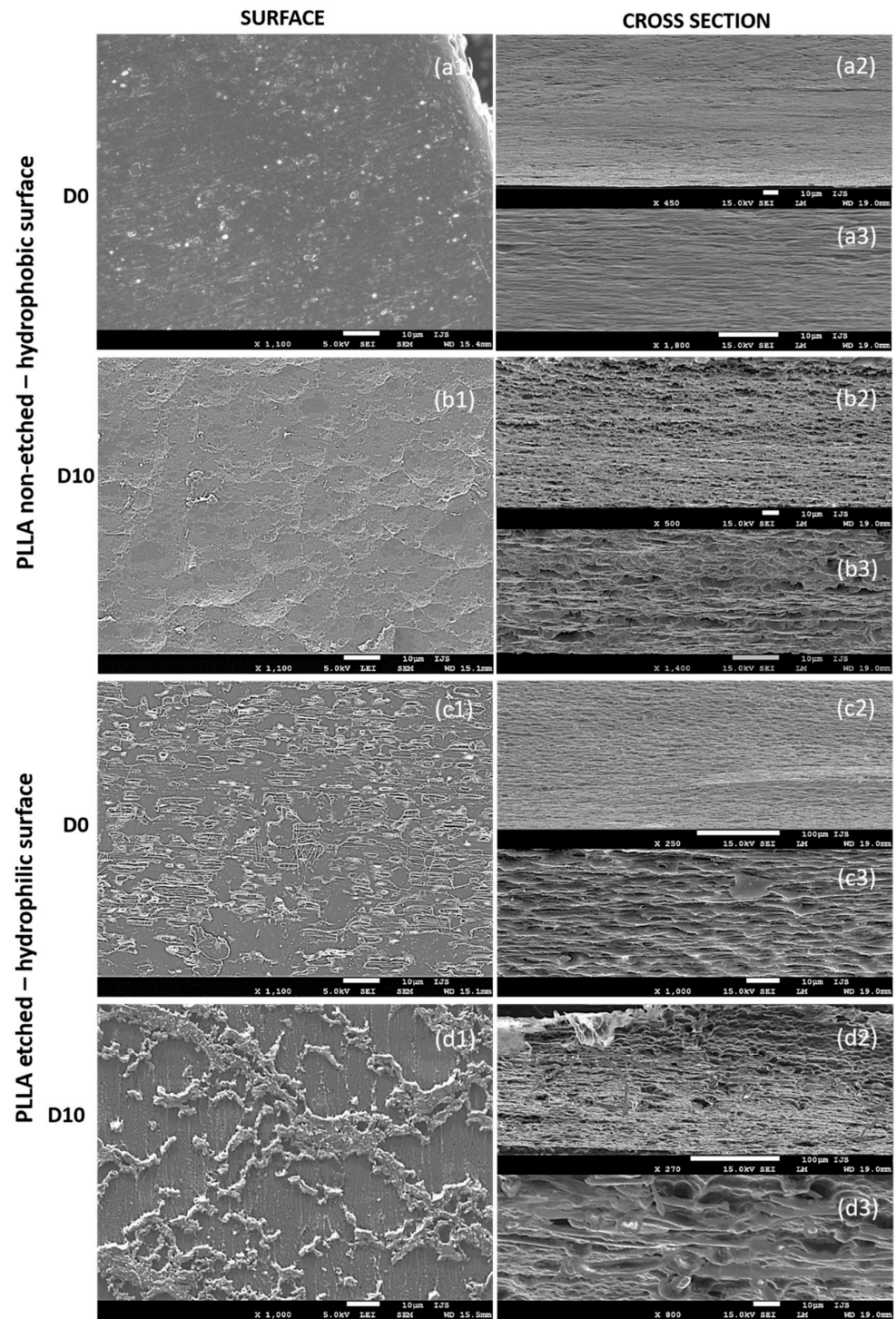


Figure 7. SEM images showing surfaces (1) and cross-sections (2, 3) of PLLA films with non-etched hydrophobic (a1–a3,b1–b3) and etched hydrophilic (c1–c3,d1–d3) surfaces before (D0) and after (D10) degradation with proteinase K.

Due to alkali etching, the hydrophilic films initially had a rougher surface with visible amorphous islands having short-edged chains (Figure 7(c1)). Such a structure is ideal for enzymatic degradation. As the degradation progressed, the roughness of the surface changed (Figure 7(d1)), indicating surface-erosion events. The inner parts of the films (observed in cross-sections, Figure 7(c2,c3,d2,d3)) did not change significantly and showed signs of delayed water swelling.

4. Discussion

Piezoelectric PLLA films were designed to optimize their applicability in electrostimulation, such as promoting mammalian cell growth. For the occurrence of effective electrical stimulation, film-cell contact is crucial, and surface properties are important. Therefore, to improve its properties for intended medical use and to ensure better cell affinity, hydrophilicity was improved by 25% using alkali etching of the polymer film, which resulted in more carboxylic end groups on the surface. The idea of the current study was to investigate the structural, mechanical, electric and surface properties of piezoelectric PLLA, with a hydrophobic and hydrophilic surface, in the presence of proteinase K as a degrading enzyme and a model of *in vitro* inflammation. This study is important since it can predict or explain further interactions of the surface-modified PLLA with living surroundings.

PLLA is a hydrophobic polymer that in general degrades through a hydrolysis reaction that occurs inside the bulk, driven by the swelling mechanism [14]. In the case of enzyme-driven degradation, when the enzyme proteinase K is present, surface erosion is reported as the main mechanism of degradation [15,16]. The reason is associated with the limited intake of the enzyme inside a polymer film.

According to our results, the structural, morphological, mechanical and piezoelectric changes obtained during the proteinase-K-induced degradation in PLLA films, two different degradation mechanisms are revealed due to the surface modification. In the case of the non-etched hydrophobic films, changes were mainly taking place in the polymer bulk. Due to the smooth surface and the strained, oriented chains observed with the electron microscope, enzyme-polymer contact is less probable; therefore, surface degradation is limited, and water diffusion inside the bulk is faster. Swelling occurs, which allows the enzymes to enter inside, meaning that bulk erosion is preferential. Enzymes cleave the tied and free amorphous parts from inside the bulk since proteinase K cannot degrade crystalline parts, resulting in increased overall crystallinity. Similar observations were made by Rangari et al., who also reported a slight increase in the crystallinity for oriented PLLA films due to the enzyme-catalyzed degradation of amorphous parts [16] but at the surface. The observed changes in crystallinity for the non-etched samples can be explained by the degradation of the free end and tie amorphous parts and possible accumulation of the cleaved crystalline parts trapped inside the film (increased crystallinity for day 10), as the degradation occurs there. However, the loss of crystallinity observed for day 5 can be associated with chain relaxation during the swelling mechanism. In both cases, for etched and non-etched films, the orientation of the polymeric films is lowered, which is expected since the swelling of the polymer in a water solution is inevitable after some time, making reorganization and mobility of the chains possible.

When observing etched films, their surface is hydrophilic with more amorphous end chains directly exposed to the outer water surroundings with the proteinase K enzyme. During the degradation, the film changes predominantly at the surface-with-surface erosion as the preferred mechanism. Therefore, only small changes are observed for bulk crystallinity and mechanical properties. Since the dense film is under amorphous clusters (as observed 7d1), the accumulation of crystalline residues is also less likely, and the loss of crystallinity is observed only on the surface.

F. Iñiguez-Franco et al. showed that increasing the hydrophilic properties of PLLA film using a chain extender, which incorporates more hydrophilic chain ends to form a branched structure, can result in hydrogen bonding between them and prevent the diffusion of water molecules inside the polymer matrix to start the bulk process [27]. This explanation can

be used to understand the changes we observed with the hydrophilic samples. In our case, the diffusion of water inside the films was slower, and enzyme travel inside the bulk was prevented. Therefore, enzymatically catalyzed hydrolysis occurs only at the surface (FTIR-921 cm^{-1} peak drop), inducing surface erosion. The loss of crystallinity for the etched sample occurred due to cleavage of the tie amorphous chain parts at the surface, releasing crystalline residues into the solution. Similar phenomena during degradation were previously explained by H. Tsuji et al. [15] on surface-eroded hydrophobic PLLA films. We also observed lowering the temperature of cold crystallization for the etched sample compared to non-etched films, which implies better orientation of the amorphous chains since the presence of oriented amorphous chains induces crystallization at a lower temperature. An interesting partial change from the α' to the α structural phase was observed only for etched films and further indicates the difference in degradation induced by surface wettability. This phenomenon could be explained by the recrystallization of polymer chains due to annealing in the medium at 37 °C since water can act as a plasticizer for PLLA. This was explained by H. Tsuji et al. as a possible event during degradation [15]. Since most of the degradation events in our etched films occur on the surface, this should also be the case for recrystallization.

The use of PLLA films for piezo-stimulation depends on their mechanical properties. PLLA is a semi-crystalline polymer; therefore, its properties depend largely on its crystalline phase. However, the balance of crystalline and amorphous regions is desirable since it enables the elasticity required for deformation in ultrasound that generates the voltage needed for promoting cell growth during stimulation. A difference in mechanical properties also implied a bulk-degradation event for non-etched and a surface-erosion event for the etched films during degradation. A huge loss of modulus, observed for non-etched films, could be connected to the swelling of the polymer film, as observed before [28], which could indicate that the degradation process was greater than that, which was evident with the weight loss. Due to swelling, there is an internal cleavage of the molecular bonds inside the film, which affects their compactness and strength, promoting degradation without the evident weight loss [1]. A similar situation was not detected in the etched films as their degradation took place at the surface.

Piezoelectricity in PLLA is a consequence of oriented and crystalline polymer chains inside the film [11]. A simple method like uniaxial drawing was used for preparing piezoelectric PLLA films. The drawing process above T_g aligns the chain molecules in the same direction in the entire film, inducing structural changes, such as crystallinity, due to the strain-induced crystallization [18]. Compared to the literature (10 pC/N) [29], smaller values for d_{14} were obtained for our films (4–4.6 pC/N); however, negligible changes were observed after the surface modification with etching to improve the hydrophilic properties of the film (results presented in a previous article [18]). It is very important that the films retained their piezoelectric properties despite all the structural and mechanical changes during degradation. Changes in the piezoelectric properties after the degradation were observed for the first time. The preservation of piezoelectric properties is a consequence of changes in crystallinity and orientation. Bulk changes are not so pronounced in hydrophilic films, where most of the degradation events and the consequent modifications are taking place at the surface. However, the detected recrystallization, loss of surface crystallinity and relaxing orientation cause the loss of half of the initial piezoelectricity (50.4%, Table 1). In hydrophobic films, most of the degradation events and the following changes occur inside the films. Although there is a decrease in the orientation and an observed increase in the porosity, a smaller drop in the piezoelectric properties (68.8% of initial value remain, Table 1) was observed, possibly due to an increase in the crystallinity and the reorientation of fibers after drying the sample. However, our estimation is for the non-etched film to have a lower piezoelectric value during the degradation since the polymer is swollen from the start, compared to the etched sample, where the swelling was not observed after 5 days of degradation.

A combination of a hydrophilic surface with gradual changes to the films during degradation that maintains their piezoelectric properties is the optimal design for polymeric films initially developed for interactions with mammalian cells. With such a design, we could expect that the high affinity of cells for hydrophilic surfaces will enable close contact between the cells and films and provide the effective electrostimulation required for applying piezo-films in regeneration processes, particularly in wound healing.

5. Conclusions

Proteinase K can induce both bulk and surface degradation in PLLA films. The surface properties of the polymer films play a significant role in their degradation. As shown in the present study, their change is a powerful tool and makes it possible to change where the degradation occurs and defines the dominant degradation mechanism. If films are hydrophilic, enzyme-driven degradation occurs at the film surface, where they degrade the accumulated amorphous areas. On the other hand, if they are hydrophobic, water uptake and polymer swelling make it possible to transfer the enzyme to the bulk where the degradation occurs. When the surface chemistry is well balanced by degradation progress, so the mechanical, structural and piezoelectric changes to the films occur gradually, and very effective interactions with the cells are expected. The observed correlations are very important for further predictions during the interactions of piezoelectric PLLA films with living surroundings, particularly during electro-stimulated regeneration and wound healing, where the gradual loss of piezoelectric properties is useful for following the tissue regeneration.

Author Contributions: Research conceptualization, L.G. and M.V.; mechanical measurements and interpretation, B.V.; data curation, L.G., B.V. and M.V.; writing—original draft preparation, L.G.; writing—review and editing, B.V., M.V. and M.S.; visualization, L.G., B.V. and M.V.; supervision, M.V.; funding acquisition, M.V. and M.S. All authors have read and agreed to the published version of the manuscript.

Funding: The work was funded by the Slovenian Research Agency (ARRS) with grants J2-8169, N2-0150 and PR-08338 and research programs P2-0091 and PR-0099.

Institutional Review Board Statement: Not applicable.

Informed Consent Statement: Not applicable.

Data Availability Statement: The data presented in this study are available on request from the corresponding author.

Acknowledgments: The authors are grateful to Mario Kurtjak and David Fabian from Advanced Materials Department, IJS, for performing FTIR and piezoelectric measurements. Sara Pintar from Biochemistry and Molecular Biology Department, IJS, for performing gel electrophoresis.

Conflicts of Interest: The authors declare no conflict of interest. The funders had no role in designing the study; in the collection, analyses, or interpretation of data; in the writing of the manuscript, or in the decision to publish the result.

References

1. De Silva, D.; Kaduri, M.; Poley, M.; Adir, O.; Krinsky, N.; Shainsky-Roitman, J.; Schroeder, A. Biocompatibility, biodegradation and excretion of polylactic acid (PLA) in medical implants and theranostic systems. *Chem. Eng. J.* **2018**, *340*, 9–14. [[CrossRef](#)] [[PubMed](#)]
2. Pappu, K.L.; Pickering, V.K. Thakur, Manufacturing and characterization of sustainable hybrid composites using sisal and hemp fibres as reinforcement of poly (lactic acid) via injection moulding. *Ind. Crop. Prod.* **2019**, *137*, 260–269. [[CrossRef](#)]
3. Rajabi, A.H.; Jaffe, M.; Arinzeh, T.L. Piezoelectric materials for tissue regeneration: A review. *Acta Biomater.* **2015**, *24*, 12–23. [[CrossRef](#)] [[PubMed](#)]
4. Jelonek, K.; Li, S.; Kaczmarczyk, B.; Marcinkowski, A.; Orchel, A.; Musial-Kulik, M.; Kasperczyk, J. Multidrug PLA-PEG filomicelles for concurrent delivery of anticancer drugs—The influence of drug-drug and drug-polymer interactions on drug loading and release properties. *Int. J. Pharm.* **2016**, *510*, 365–374. [[CrossRef](#)]
5. Mushtaq, F.; Torlakcik, H.; Vallmajo-martin, Q.; Can, E.; Zhang, J.; Röhrig, C.; Shen, Y.; Yu, Y.; Chen, X.; Müller, R.; et al. Magnetolectric 3D scaffolds for enhanced bone cell proliferation. *Appl. Mater. Today* **2019**, *16*, 290–300. [[CrossRef](#)]

6. Gomaa, S.F.; Madkour, T.M.; Moghannem, S.; El-sherbiny, I.M. New polylactic acid/cellulose acetate-based antimicrobial interactive single dose nanofibrous wound dressing mats. *Int. J. Biol. Macromol.* **2017**, *105*, 1148–1160. [[CrossRef](#)]
7. Barroca, N.; Marote, A.; Vieira, S.I.; Almeida, A.; Fernandes, M.H.V.; Vilarinho, P.M.; Odete, A.B. Electrically polarized PLLA nanofibers as neural tissue engineering scaffolds with improved neuritogenesis. *Colloids Surf. B Biointerfaces* **2018**, *167*, 93–103. [[CrossRef](#)]
8. Shin, D.; Hong, S.W.; Hwang, Y.-H. Recent Advances in Organic Piezoelectric Biomaterials for Energy and Biomedical Applications. *Nanomaterials* **2020**, *10*, 123. [[CrossRef](#)]
9. Ates, B.; Koytepe, S.; Ulu, A.; Gurses, C.; Thakur, V.K. Chemistry, Structures, and Advanced Applications of Nanocomposites from Biorenewable Resources. *Chem. Rev.* **2020**, *120*, 9304–9362. [[CrossRef](#)]
10. Tajitsu, Y. Basic study of controlling piezoelectric motion of chiral polymeric fiber. *Ferroelectrics* **2009**, *389*, 83–94. [[CrossRef](#)]
11. Lovell, C.S.; Fitz-Gerald, J.M.; Park, C. Decoupling the effects of crystallinity and orientation on the shear piezoelectricity of polylactic acid. *J. Polym. Sci. Part B Polym. Phys.* **2011**, *49*, 1555–1562. [[CrossRef](#)]
12. Minary-Jolandan, M.; Yu, M. Nanoscale characterization of isolated individual type I collagen fibrils: Polarization and piezoelectricity. *Nanotechnology* **2009**, *20*, 085706. [[CrossRef](#)] [[PubMed](#)]
13. Murillo, G.; Blanquer, A.; Vargas-estevez, C.; Barrios, L.; Ibáñez, E.; Nogués, C.; Esteve, J. Electromechanical Nanogenerator-Cell Interaction Modulates Cell Activity. *Bioelectronics* **2017**, *29*. [[CrossRef](#)]
14. von Burkersroda, F.; Schedl, L.; Gopferich, A. Why degradable polymers undergo surface erosion or bulk erosion. *Biomaterials* **2002**, *23*, 4221–4231. [[CrossRef](#)]
15. Tsuji, H.; Ogiwara, M.; Saha, S.K.; Sakaki, T. Enzymatic, alkaline, and autocatalytic degradation of poly (L-lactic acid): Effects of biaxial orientation. *Biomacromolecules* **2006**, *7*, 380–387. [[CrossRef](#)]
16. Rangari, D.; Vasanthan, N. Study of Strain-Induced Crystallization and Enzymatic Degradation of Drawn Poly (l-lactic acid) (PLLA) Films. *Macromolecules* **2012**, *45*, 7397–7403. [[CrossRef](#)]
17. Casalini, T.; Rossi, F.; Castrovinci, A.; Perale, G. A Perspective on Polylactic Acid-Based Polymers Use for Nanoparticles Synthesis and Applications. *Front. Bioeng. Biotechnol.* **2019**, *7*, 1–16. [[CrossRef](#)]
18. Udovc, L.; Spreitzer, M.; Vukomanovic, M. Towards hydrophilic piezoelectric poly-L-lactide films: Optimal processing, post-heat treatment and alkaline etching. *Polym. J.* **2020**, *52*, 299–311. [[CrossRef](#)]
19. Vogel, C.; Wessel, E.; Siesler, H.W. FT-IR Spectroscopic Imaging of Anisotropic Poly (3-hydroxybutyrate)/Poly (lactic acid) Blends with Polarized Radiation. *Macromolecules* **2008**, *41*, 2975–2977. [[CrossRef](#)]
20. Nobeshima, T.; Sakai, H.; Ishii, Y.; Uemura, S.; Yoshida, M. Polarized FT-IR Study of Uniaxially Aligned Electrospun Poly (DL-Lactic Acid) Fiber Films. *J. Photopolym. Sci. Technol.* **2016**, *29*, 353–356. [[CrossRef](#)]
21. Farah, S.; Anderson, D.G.; Langer, R. Physical and mechanical properties of PLA, and their functions in widespread applications—A comprehensive review. *Adv. Drug Deliv. Rev.* **2016**, *107*, 367–392. [[CrossRef](#)] [[PubMed](#)]
22. Yanagida, H.; Okada, M.; Masuda, M.; Ueki, M.; Narama, I.; Kitao, S.; Koyama, Y.; Furuzono, T.; Takakuda, K. Cell adhesion and tissue response to hydroxyapatite nanocrystal-coated poly (L-lactic acid) fabric. *JBIOSEC* **2009**, *108*, 235–243. [[CrossRef](#)] [[PubMed](#)]
23. Bernard, F.; Gimeno, L.; Viala, B.; Gusarov, B.; Cugat, O. Direct Piezoelectric Coefficient Measurements of PVDF and PLLA under Controlled Strain and Stress. *Proceedings* **2017**, *1*, 335. [[CrossRef](#)]
24. Webb, K.; Hlady, V.; Tresco, P.A. Relative importance of surface wettability and charged functional groups on NIH 3T3 fibroblast attachment, spreading, and cytoskeletal organization. *J. Biomed. Mater. Res.* **2009**, *41*, 422–430. [[CrossRef](#)]
25. Chen, X.; Kalish, J.; Hsu, S.L. Structure Evolution of a α' -Phase Poly (lactic acid). *J. Polym. Sci. Part B Polym. Phys.* **2011**, *49*, 1446–1454. [[CrossRef](#)]
26. Leluk, K.; Frackowiak, S.; Ludwiczak, J.; Rydzkowski, T.; Thakur, V.K. The Impact of Filler Geometry on Polylactic Acid-Based Sustainable Polymer Composites. *Molecules* **2021**, *26*, 149. [[CrossRef](#)]
27. Iñiguez-franco, F.; Auras, R.; Ahmed, J.; Selke, S.; Rubino, M.; Dolan, K.; Soto-valdez, H. Control of hydrolytic degradation of Poly(lactic acid) by incorporation of chain extender: From bulk to surface erosion. *Polym. Test.* **2018**, *67*, 190–196. [[CrossRef](#)]
28. Subramani, R.; Izquierdo-alvarez, A.; Bhattacharya, P.; Meerts, M. The Influence of Swelling on Elastic Properties of Polyacrylamide Hydrogels. *Front. Mater.* **2020**, *7*, 1–13. [[CrossRef](#)]
29. Fukada, E. New Piezoelectric Polymers. *Jpn. J. Appl. Phys.* **1998**, *37*, 2775–2780. [[CrossRef](#)]

Cite this article

Gradišar Centa U, Sterniša M, Višič B et al. (2021)
Novel nanostructured and antimicrobial PVDF-HFP/PVP/MoO₃ composite.
Surface Innovations 9(5): 256–266,
<https://doi.org/10.1680/jsuin.20.00073>

Invited Feature Article

Paper 2000073
Received 01/10/2020; Accepted 08/12/2020
Published online 15/12/2020
Published with permission by the ICE under the
CC-BY 4.0 license.
(<http://creativecommons.org/licenses/by/4.0/>)

Keywords: anti-bacterial/
nanocomposites/surface characterisation

Novel nanostructured and antimicrobial PVDF-HFP/PVP/MoO₃ composite

Urška Gradišar Centa MSc

PhD student, Condensed Matter Physics Department, Jožef Stefan Institute, Ljubljana, Slovenia (Orcid:0000-0001-5206-141X) (corresponding author: urska.gradisar@ijs.si)

Meta Sterniša PhD

Teaching Assistant and Researcher, Department of Food Science and Technology, Biotechnical Faculty, University of Ljubljana, Ljubljana, Slovenia (Orcid:0000-0002-2414-3618)

Bojana Višič PhD

Assistant Research Professor, Solid State Physics Department, Institute of Physics Belgrade, Belgrade, Serbia; Center for Solid State Physics and New Materials, Jožef Stefan Institute, Ljubljana, Slovenia (Orcid:0000-0002-2065-0727)

Žiga Federl BSc

Student, Faculty of Mathematics and Physics, University of Ljubljana, Ljubljana, Slovenia

Sonja Smole Možina PhD

Professor, Department of Food Science and Technology, Biotechnical Faculty, University of Ljubljana, Ljubljana, Slovenia (Orcid:0000-0001-7949-8128)

Maja Remškar PhD

Professor, Condensed Matter Physics Department, Jožef Stefan Institute, Ljubljana, Slovenia (Orcid:0000-0002-8919-1768)

Contact surfaces represent a liability for the transmission of microbial contamination, leading to high consumption of detergents and biocides for their care and further increasing the already problematic antimicrobial resistance of microorganisms. This issue could be addressed by the use of antimicrobial nanocomposite coatings. In this research, a polymer nanocomposite of inert poly(vinylidene fluoride-co-hexafluoropropylene) (PVDF-HFP) and water-soluble polyvinylpyrrolidone (PVP) polymers with molybdenum trioxide (MoO₃) nanowires (NWs) was designed and characterised for its surface properties and antimicrobial potential. The nanocomposite has an inhomogeneous structure with a positively charged and hydrophilic surface. The nanofiller reduces the surface roughness, changes the zeta potential from negative to positive, increases the wetting angle and thermal stability of the blend and maintains the polar β -phase in PVDF-HFP. The high specific surface area of the NWs leads to rapid release into water and causes pH decrease, followed by hydrolysis of PVP polymer and formation of carboxyl acid and ammonium salt. The antimicrobial activity of the nanocomposite inactivates both bacteria and fungi, indicating that the novel nanocomposite is a stable nanostructured coating unfavourable for microorganism colonisation. The antimicrobial activity of this nanocomposite is activated by water, which makes it an intriguing candidate for antimicrobial coating of contact surfaces.

Notation

A	surface area of the foils
C	average number of cells counted
D	dilution factor
E	electric field
E^*	elastic modulus
N	number of viable cells per square centimetre of the tested foil
R_a	average surface roughness of the foils
$\tan \delta$	loss tangent
T_s	sample temperature
V	volume of the solution used to wash the foils
v	measured electrophoretic velocity
ϵ	electrical permittivity of the electrolytic solution
η	viscosity
ζ	zeta potential

1. Introduction

Contact surfaces pose a risk for the transmission of microbial contamination. Moisture from the air and organic molecules created by frequent contact with hands provides the right environment for microorganisms to colonise, grow and form a biofilm. In order to

survive, microorganisms form biofilms that protect them from the negative effects of the environment, including biocides.¹ Antimicrobial coatings are a promising approach to preventing the adhesion and growth of microorganisms on different surfaces in hospitals and other public spaces (e.g. door handles, passenger hand straps on buses, buttons in elevators, handrails of shopping carts, tables in dining rooms and work surfaces in kitchens).² Therefore, the development of new surface treatments has become a topic of great interest, and more attention is being paid to the development of antimicrobial coatings.

Various synthetic approaches based on the immobilisation of microbes or the release of antimicrobial substances, such as metal derivatives and nanomaterials, polyammonium salts, natural antimicrobials and antibiotics, have been used in antimicrobial coatings.^{3–7} However, the increasing problem of growing microbial resistance to antimicrobial agents has led to the search for new ones with a non-specific mechanism of action that can be achieved by using different metals. Silver (Ag), zinc (Zn) and titanium (Ti) and their oxides have been extensively studied for such purposes. When inorganic nanoparticles are incorporated into polymer nanocomposites, their physico-chemical properties

differ from those of the individual components and lead to the development of novel multifunctional materials with a variety of applications, including the possibility of use as an antimicrobial coating. For example, polymer/nanosilver composite multilayer coatings have shown controlled release of biocidal silver ions and relatively good biocompatibility and environmental safety.⁸ Biocompatible poly(*N*-isopropylacrylamide) coatings with incorporated zinc oxide (ZnO) nanoparticles were reported as an alternative to nanosilver. These showed a bactericidal behaviour towards *Escherichia coli* at a low zinc oxide concentration (approximately 0.74 µg/cm²).⁹ Nanotitania/polyurethane composite coatings also showed antibacterial activity against *E. coli*, as 99% of the bacteria were inactivated in less than 1 h under solar irradiation.¹⁰ Unfortunately, silver and zinc oxide nanoparticles are toxic to human cells,¹¹ while ultraviolet (UV) light is needed to activate the antimicrobial properties of titanium dioxide (TiO₂).¹⁰

Various molybdenum (Mo) oxides have already been proposed as an alternative to these inorganic particles for use in public and healthcare environments because of their low cytotoxicity, biocompatibility and good antimicrobial activity.¹² A good antimicrobial potential of molybdenum oxides has also been shown in other studies.^{13–17} The antimicrobial activity has been attributed to an acidic surface reaction in the presence of water that produces molybdic acid, which dissociates into hydronium (H₃O⁺) and molybdate (MoO₄²⁻) ions.¹⁴ Moreover, antimicrobial activity has been shown to be dependent on the energy gap of molybdenum trioxide (MoO₃) nanorods¹⁵ and on a specific molybdenum trioxide crystallographic phase.¹² A further comparison of commercial and synthesised forms showed the better activity of the synthesised orthorhombic structure.¹²

In addition to the antimicrobial potential of the nanofiller used for the antimicrobial composite, the properties of novel nanocomposite coating must also meet other requirements. The embedded nanomaterials (or the ions dissolved from them) need to come into physical contact with the bacteria to affect them, and part of the host material must be chemically inert to form the coating matrix. Therefore, a mixture of a water-soluble polymer containing water-soluble nanomaterials and water-insoluble polymers as the coating matrix would be a preferred design.

Within the scope of this research, a polymer nanocomposite was designed from a mixture of poly(vinylidene fluoride-co-hexafluoropropylene) (PVDF-HFP) and water-soluble polyvinylpyrrolidone (PVP) polymers with the addition of molybdenum trioxide nanowires (NWs). PVDF-HFP was chosen as the chemically inert part of the nanocomposite, characterised by low crystallinity (approximately 50%), low-temperature glass transition (−35°C) and high thermal stability (up to 143°C).^{18–21} PVP is a biocompatible and water-soluble polymer with low chemical toxicity, high water solubility and the ability to act as a dispersant.²² This particular combination of polymers has been reported as a possible novel high-temperature proton-exchange membrane²³ and for applications in wound healing.²⁴ Modified

PVDF-HFP membranes with grafting of *N*-vinyl-2-pyrrolidone and iodine (I) immobilisation²² and quaternised pyridinium groups²⁵ have been shown to have good antimicrobial activity.

The nanocomposite was prepared in the form of a thin, self-standing foil as a model of a contact coating. The surface morphology on the nanoscale, the structural properties and the wetting angle, as well as the optical vibration and dynamic mechanical properties, were evaluated, and the antimicrobial activity of this nanocomposite against bacteria and fungi was determined.

2. Experimental section

2.1 Nanomaterial used and preparation of the nanocomposite

Molybdenum trioxide NWs with a diameter of 100–150 nm and a length of up to 3 µm have a high degree of porosity and a specific surface area of 12 m²/g. They are synthesised by oxidation of Mo₆S₂I₈ NWs (Nanotul Ltd, Slovenia) at 285°C for 24 h.²⁶ Molybdenum trioxide NWs grow in an orthorhombic crystal structure (JCPDS 76-1003). The solubility of molybdenum trioxide is 2.03 ± 0.09 mg/ml in pure water. The authors showed that 6 h exposure of HaCaT cells to molybdenum trioxide at a concentration of 1 mg/ml had no effect on the survival of these cells – that is, no cytotoxic effect was observed.²⁷

For the preparation of the nanocomposite, PVDF-HFP, from Sigma-Aldrich, USA, and PVP K30, from Sigma-Aldrich, USA, were dissolved separately in dimethylformamide (DMF), from Carlo Erba Reagents, Italy, and mixed using a magnetic stirrer for 2 h at 400 revolutions per min (rpm) at 80°C. In the next step, the molybdenum trioxide NWs were added to PVP and the dispersion was mixed for 2 h. Finally, PVP with molybdenum trioxide was mixed with the dissolved PVDF-HFP for another 2 h. The same mass ratio of 69:23:8 (PVDF-HFP:PVP:molybdenum trioxide) was used to prepare all foils. They were prepared by casting of the nanocomposite solution onto a Teflon plate and drying for 2 h at 80°C. For comparison, a PVDF-HFP/PVP polymer blend without molybdenum trioxide was prepared by mixing (2 h) separately dissolved polymers in DMF and then cast and dried under the same conditions as the PVDF-HFP/PVP/molybdenum trioxide nanocomposite.

2.2 Physico-chemical characterisation

The morphology of the nanocomposite films was investigated with a Supra 36 VP field-emission scanning electron microscope (SEM), from Carl Zeiss, Germany. The samples were placed on adhesive carbon (C) tape and sputtered with a 10 nm gold (Au) layer, with the aim of increasing the conductivity of the electrons during the investigation. The Raman spectra and the topography of the nanocomposites were recorded with an alpha300 confocal Raman microscope from WITec, Germany, using green laser (532.3 nm) and equipped with an atomic force microscope (AFM). The power of the laser beam measured on the sample was 0.3 mW.

The concentration of molybdenum trioxide dissolved from the nanocomposite foils was determined by UV–Vis spectroscopy using a PerkinElmer Lambda 950 spectrometer (USA) and a quartz cuvette. The nanocomposite foil with a mass concentration of 5 mg/ml was added to water in a glass beaker at room temperature (RT) while mixed with a magnetic stirrer at 300 rpm for 6 h. For the calibration curve, the absorbance amplitude of the peak at 210 nm in several molybdenum trioxide–water solutions with known concentrations was used. The surface zeta potential was measured with an Anton Paar SurPass electrokinetic analyser (Austria) with an adjustable gap cell and sample dimensions of 20 × 10 mm. The time for four measuring cycles was 5 min. The electrolyte used was a 0.001 M potassium chloride (KCl) solution in ultrapure water. The zeta potential was automatically calculated from the electrophoretic mobility, based on the Smoluchowski equation, $v = (\epsilon E/\eta)\xi$, where v is the measured electrophoretic velocity, η is the viscosity, ϵ is the electrical permittivity of the electrolytic solution and E is the electric field.²⁸

The wetting angle of the coatings for distilled water was measured at three points of each sample with an optical tensiometer Attension Theta Lite TL100 (Sweden) and the sessile drop method. All measurements were performed at RT, and the results are presented as the mean value with the associated standard deviation. The dynamic contact angle (CA) of water on the polymer blend and nanocomposite foil was determined according to the Wilhelmy plate method²⁹ with a Krüss K100 processor tensiometer (Krüss, Germany). The surface tension of demineralised water was obtained from the Krüss LabDesk database (72.8 mN/m).³⁰ A new sample and fresh water were used for each test cycle. The sample was first immersed in the liquid with the film normal perpendicular to the direction of immersion and then pulled out in reverse. The measurement began when the liquid buoyancy force acting on the sample was first detected and the sample reached an immersion depth of 2 mm. The immersion speed and pull-out speed were 6 mm/min. The sensitivity of force detection was set to 0.001 N. The maximum immersion depth was 7 mm. The advancing and receding CAs were determined with the Krüss LabDesk software.

The pH values were measured with a SevenExcellence multiparameter meter, from Mettler Toledo, Switzerland, with an InLab Expert Pro-ISM probe. The polymer blend and the nanocomposite foil with a mass concentration of 5 mg/ml were added to water in a glass beaker at RT. The samples were mixed with a magnetic stirrer at 300 rpm, and the pH was measured at 1 min intervals. While dissolving, they were submerged under the water surface.

The dynamic mechanical properties of the coatings were investigated with a DMA/SDTA861 dynamic mechanical analyser, from Mettler Toledo, Switzerland, in tension mode. The validity of Hooke's law – that is, the range in which the material behaves elastically – was measured with a displacement between 1 and 20 µm.

2.3 Antimicrobial test

The antimicrobial activity against Gram-positive bacteria (*Staphylococcus aureus* ŽMJ72 and *Listeria monocytogenes* ŽM58), Gram-negative bacteria (*E. coli* ŽM370 and *Pseudomonas aeruginosa* ŽM519), yeasts (*Candida albicans* ŽMJ32 and *Pichia anomala* ŽMJ6) and moulds (*Penicillium verrucosum* ŽM23 and *Aspergillus flavus* ŽM25) was evaluated. All microorganisms were from the culture collection of the Laboratory for Food Microbiology at the Department of Food Science, Biotechnical Faculty (designations ŽM and ŽMJ). The bacteria were stored in tryptic soy broth (Biolife, Italy) and the fungi in malt extract broth (Biolife, Italy) with 15% glycerol (Kemika, Croatia) at –80°C, revitalised on tryptic soy agar (TSA; Biolife, Italy) or malt extract agar (MEA; Biolife, Italy) and incubated at 37°C for 24 h for the bacteria or at 30°C for the yeasts and at 25°C for 5–7 days for the moulds (I-105 CK incubator, Kambič, Slovenia). Standardised inocula with a cell concentration of 5 log colony-forming units (CFU)/ml were prepared.

The antimicrobial potential of the material was evaluated using a modified ISO 22196 method.³¹ An inert foil (polyethylene (PE)) was used as negative control, while the PVDF-HFP/PVP polymer blend was used for comparison with the PVDF-HFP/PVP/molybdenum trioxide nanocomposite. The inoculum of individual bacteria, yeast or mould was applied to PE, the PVDF-HFP/PVP polymer blend and the PVDF-HFP/PVP/molybdenum trioxide nanocomposite foils and covered with a PE foil to keep them humid. All three foil types were tested in three parallel experiments. After the test periods (0, 3 and 6 h for all test microorganisms and an additional 24 h for the fungi), the microorganisms were washed from the coatings with a neutraliser (soybean casein digest broth with lecithin and polyoxyethylene sorbitan monooleate), mixed on an orbital shaker for 10 min, diluted in saline solution and plated using the pour plate method with TSA for the bacteria and MEA for the fungi. The number of viable cells was calculated as $N = (100 \times C \times D \times V)/A$, where N is the number of viable cells per square centimetre of the tested foil, C is the average number of cells counted, D is the dilution factor, V is the volume of the solution used to wash the foils (10 ml) and A is the surface area of the foils (400 mm²). The results for each microorganism at each time point were compared with analysis of variance and post hoc Tukey test in the SPSS software program.

3. Results

3.1 Surface topography of the PVDF-HFP/PVP blend and PVDF-HFP/PVP/molybdenum trioxide nanocomposite

The surface topography of the investigated materials is shown in Figure 1. The molybdenum trioxide NWs have relatively homogeneous sizes, with a length of up to a few micrometres and a diameter of 100–150 nm (Figure 1(a)). The surface of the PVDF-HFP/PVP blend (Figure 1(b)) is nanostructured with rounded PVP islands with diameters of 200–500 nm. The PVDF-HFP/PVP/molybdenum trioxide nanocomposite (Figure 1(c)) has

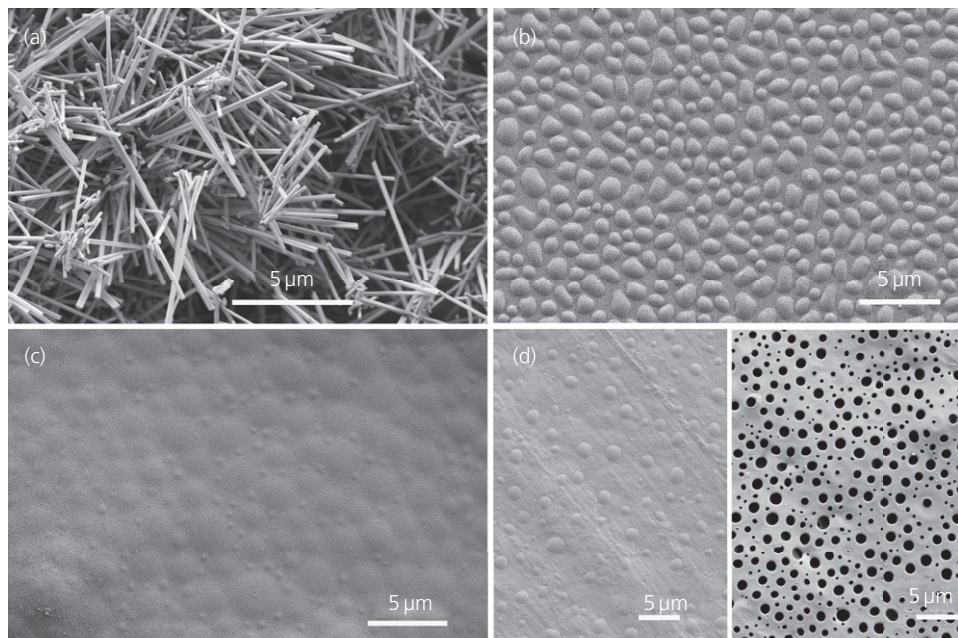


Figure 1. SEM images of (a) molybdenum trioxide NWs, (b) PVDF-HFP/PVP polymer blend, (c) PVDF-HFP/PVP/molybdenum trioxide nanocomposite and (d) PVDF-HFP/PVP polymer blend after 6 h in water and (e) PVDF-HFP/PVP/molybdenum trioxide nanocomposite after 6 h in water

a domain surface structure with a diameter of a few micrometres and PVP islands in the submicrometre range. After 6 h exposure of the polymer blend and the nanocomposite foils to water, partial removal of the PVP islands from the surface of the polymer blend was observed (Figure 1(d)), but they were completely removed from the surface of the molybdenum trioxide nanocomposite, leaving a porous surface (Figure 1(e)).

The surface topography of the polymer matrix (Figure 2(a)) and the polymer nanocomposite (Figure 2(b)) on the nanometre scale was revealed using an environmental AFM. The bright PVP islands in the matrix are about 200 nm high, whereas in the nanocomposite, the height was twice reduced and smaller islands are visible. The addition of molybdenum trioxide NWs reduced

the surface roughness of the polymer nanocomposite with respect to that of the polymer matrix.

3.2 Vibration analysis of the PVDF-HFP/PVP blend and PVDF-HFP/PVP/molybdenum trioxide nanocomposite

Raman spectroscopy was used to study the polymer blend (Figure 3(a)) and the effect of molybdenum trioxide NWs (Figure 3(b)) on their vibration states. The positions of the Raman peaks are listed in Tables 1 and 2 and attributed to specific components. It is important to note that the Raman peak at 839 cm⁻¹ indicates the presence of the polar β-phase of PVDF-HFP,³⁴ which increased strongly in the polymer blend (Figure 3(a), spectrum C). In the spectrum recorded between the PVP islands (Figure 3(b),

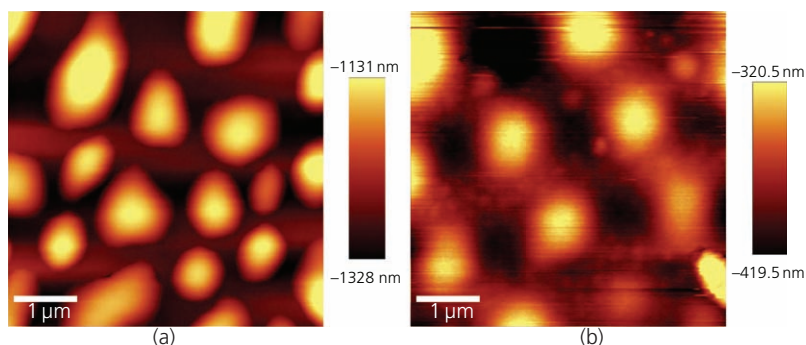


Figure 2. AFM images: (a) PVDF-HFP/PVP polymer blend; (b) PVDF-HFP/PVP/molybdenum trioxide nanocomposite

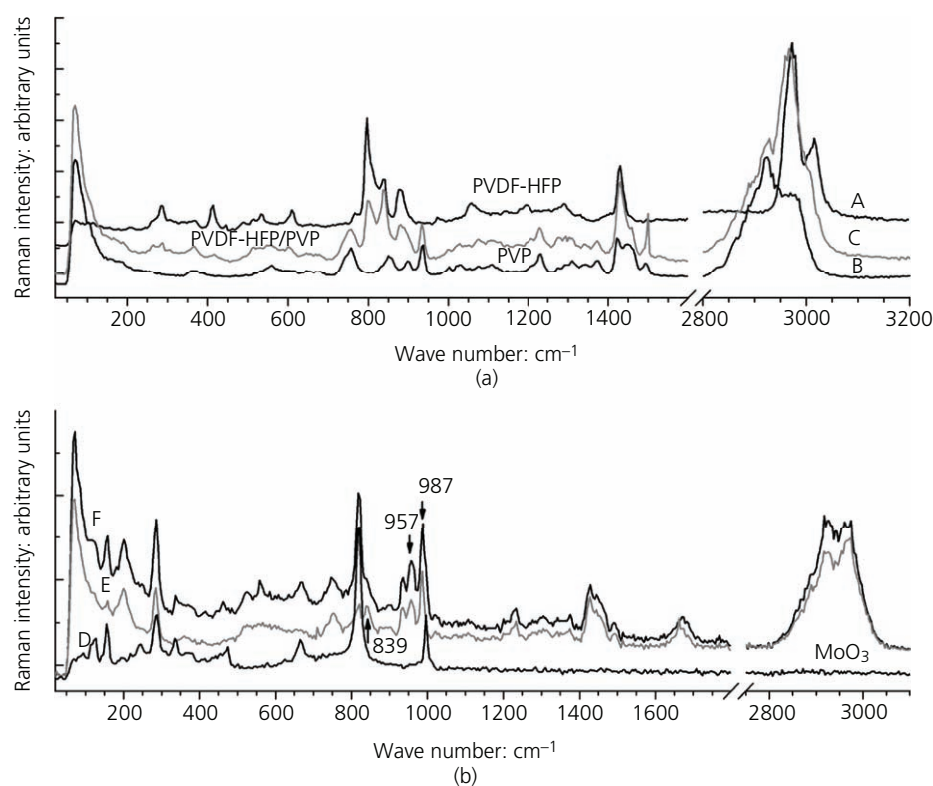


Figure 3. Raman spectra: (a) polymers (A, PVDF-HFP; B, PVP) and polymer blend (C, PVDF-HFP/PVP); (b) molybdenum trioxide (D) and PVDF-HFP/PVP/molybdenum trioxide nanocomposite (E, between islands; F, island)

Table 1. Positions of Raman peaks in the spectra of the PVDF-HFP/PVP blend, pure PVP and pure PVDF-HFP

PVDF-HFP/PVP blend		PVP		PVDF-HFP	
Position: cm ⁻¹	Relative intensity: %	Position: cm ⁻¹	Literature ^{32,33}	Position: cm ⁻¹	Literature ²⁸
71	100	70	72	—	—
285	78	—	—	283	284
558	63	560	556	413	—
747	64	—	746	610	—
757	53	758	758	797	—
839	63	850	—	839	839 β-phase
—	—	898	—	—	—
—	—	—	—	876	—
934	53	937	934	1058	—
—	—	—	—	1194	—
1233	50	1232	1233, 1228	—	—
—	—	—	—	1290	—
1429	62	1422	1421	—	1430
1445	59	1447	—	—	1445
1490	53	1492	1494	—	—
1668	54	1660	1665, 1663	—	—
2924	78	2922	2928	—	—
2974	78	2969	—	2972	2971
—	—	—	—	3015	—

spectrum E), the presence of the molybdenum trioxide peaks is less expressed than in the spectrum recorded on the PVP islands (Figure 3(b), spectrum F), where the molybdenum trioxide peaks dominate. This indicates that most of the molybdenum trioxide is

located on the PVP islands. The polar β-phase in PVDF-HFP is distinctive in spectrum E (between the islands), while in spectrum F (on the islands), it appears as a weak shoulder on the strong molybdenum trioxide peak centred at 819 cm⁻¹. However, in both

Table 2. Position of Raman peaks in the spectra of the PVDF-HFP/PVP/molybdenum trioxide nanocomposite taken on the PVP islands, on the area between the PVP islands and on pristine molybdenum trioxide NWs, with peaks assigned

Islands		Between islands		Molybdenum trioxide			Assignment
Position: cm ⁻¹	Relative intensity: %	Position: cm ⁻¹	Relative intensity: %	This study		Literature ^{34–36}	
				Position: cm ⁻¹	Relative intensity: %	Position: cm ⁻¹	
72	100	72	100				PVP
124	60	124	72	127	64	130	Molybdenum trioxide
158	74	158	70	156	69	159–161	Molybdenum trioxide
201	73	200	73	197	58	199	Molybdenum trioxide
217	sh	217	sh	218	59	219	Molybdenum trioxide
248	sh	249	sh	246	62	249	Molybdenum trioxide
286	78	285	73	289	71	295	PVDF-HFP, molybdenum trioxide
337	59	—	—	335	64	339–340	Molybdenum trioxide
474	56	—	—	474	61	470–482	Molybdenum trioxide
668	62	—	—	665	63	666–667	Molybdenum trioxide
817	85	821	69	821	100	820–823	Molybdenum trioxide
839	63	839	68	—	—	—	PVDF-HFP β-phase
935	64	935	68	—	—	—	PVP
957	68	957	70	—	—	—	New peak
987	77	987	78	—	—	—	New peak

sh, peak shoulder

nanocomposite spectra (E and F), two new peaks are observed at 957 and 987 cm⁻¹. The peak at 957 cm⁻¹ is assigned to O=Mo=O symmetric polarised stretching modes,³² while the narrow intense peak at 987 cm⁻¹ is generally assigned to the terminal oxygen (Mo⁶⁺=O) stretching mode.^{33,35,36}

3.3 Mechanical properties of the PVDF-HFP/PVP blend and PVDF-HFP/PVP/molybdenum trioxide nanocomposite

The curves of the elastic modulus (E^*) and the loss tangent ($\tan \delta$) of the polymer blend (a, b) and the polymer nanocomposite (c, d) are shown in Figure 4. The spectra are rather featureless, with broad glass-transition peaks at $-55 \pm 3^\circ\text{C}$ (full width at half maximum

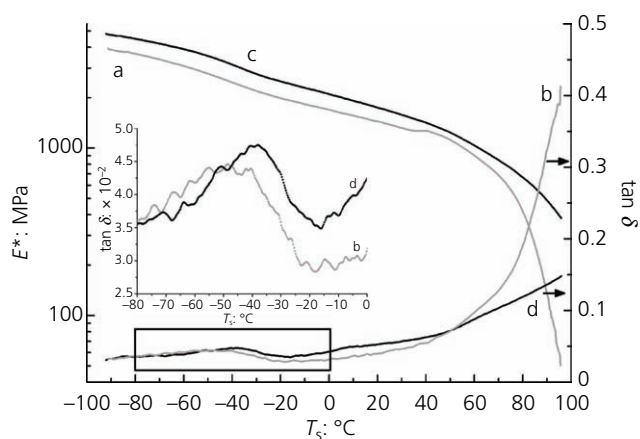


Figure 4. Elastic modulus E^* and $\tan \delta$: a, b, PVDF-HFP/PVP blend; c, d, PVDF-HFP/PVP/molybdenum trioxide nanocomposite

(FWHM): $37 \pm 1^\circ\text{C}$) (blend) and at $-38 \pm 3^\circ\text{C}$ (FWHM: $26 \pm 1^\circ\text{C}$) (nanocomposite). The broadness of the peaks indicates the inhomogeneity of the polymer blend. The smaller FWHM of the convolution peak of the nanocomposite indicates that the molybdenum trioxide filler reduces the degree of inhomogeneity, corresponding to the smoother surface of the nanocomposite in relation to that of the pure polymer blend revealed by the AFM (Figure 2). The related glass-transition temperatures of the constituent polymers are -35°C (PVDF-HFP¹⁹) and 170°C (PVP³⁷). For PVDF-HFP, a transition temperature of 50°C was also observed.¹⁹ Above this temperature (50°C), where the $\tan \delta$ curves in Figure 4 intersect, the pure polymer blend entered the elastic flow region, while the nanocomposite shows higher thermal stability with a rubber-like plateau extending to the final temperature (95°C) of the measurement. This thermal stabilisation of the PVDF-HFP part of the blend by the molybdenum trioxide nanofiller is evidence of the interaction between the molybdenum trioxide NWs and the PVDF-HFP chains during crystallisation of the polymer blend.³⁸ The addition of molybdenum trioxide to the polymer blend increased the complex elastic modulus E^* of the polymer nanocomposite over the entire temperature range.

3.4 Wetting angle and surface charge of the PVDF-HFP/PVP blend and PVDF-HFP/PVP/molybdenum trioxide nanocomposite

The degree of the surface hydrophilicity of the PVDF-HFP/PVP blend and the PVDF-HFP/PVP/molybdenum trioxide nanocomposite foils was investigated by static and dynamic CA measurements. Figure 5 shows the water CAs of the polymer blend (Figure 5(a)) and the polymer nanocomposite (Figure 5(b)). The molybdenum trioxide NWs increased the CA of the nanocomposite ($87.1 \pm 0.1^\circ$) compared with that of the polymer blend ($83.5 \pm 0.1^\circ$). The surfaces

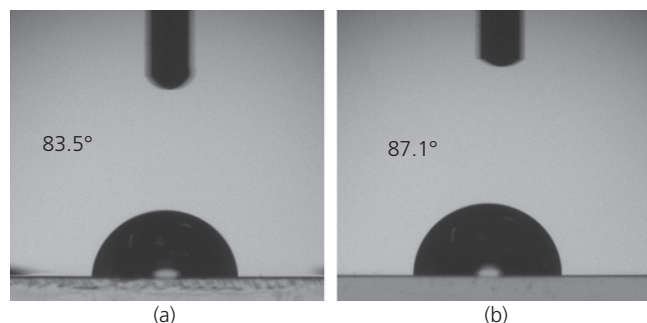
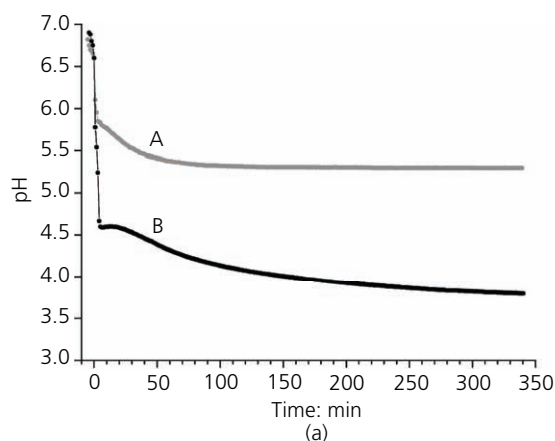


Figure 5. CA test: (a) PVDF-HFP/PVP polymer blend; (b) PVDF-HFP/PVP/molybdenum trioxide nanocomposite

of the samples are chemically heterogeneous and have nanostructures at the atomic scale. For this reason, the dynamic CA was also measured using the Wilhelmy plate method.³⁹ The advancing CA was $87.5 \pm 0.2^\circ$ for the nanocomposite and $83.8 \pm 0.2^\circ$ for polymer blend. In both cases, the receding CA was 0° . The addition of nanoparticles can modify the wettability of polymer surfaces, as they can alter the chemical composition of the surface or the surface morphology – for example, surface roughness.⁴⁰ The surface roughness of the nanocomposite was twice smaller than that of the polymer blend, and therefore, the authors observed a slightly larger value of the CA. Increasing the surface roughness decreases the

Table 3. Results and parameters of the zeta-potential measurements

	pH	Zeta potential: mV	Gap height: μm
PVDF-HFP/PVP polymer blend	6.57 ± 0.02	-26.3 ± 0.6	98.04
PVDF-HFP/PVP/molybdenum trioxide nanocomposite	5.62 ± 0.01	$+10 \pm 3$	100.57



CA.⁴¹ The values of the advancing angles indicate that the nanocomposite is slightly less hydrophilic than the pure polymer blend, although it can still be considered hydrophilic ($CA < 90^\circ$).

Since the electric charge of a material surface is considered one of the most important physical factors influencing biological interactions,⁴² the surface charges of the PVDF-HFP/PVP blend and the PVDF-HFP/PVP/molybdenum trioxide nanocomposite were determined (Table 3). It was found that the polymer blend without molybdenum trioxide is negatively charged, while the addition of molybdenum trioxide NWs causes a change in the surface zeta potential to a positive value.

3.5 Solubility kinetics of the PVDF-HFP/PVP blend and PVDF-HFP/PVP/molybdenum trioxide nanocomposite in water

The polymer blend of water-soluble PVP and water-insoluble PVDF-HFP and the polymer nanocomposite PVDF-HFP/PVP with added water-soluble molybdenum trioxide at a concentration of 5 mg/ml were added to distilled water at RT, and the pH of the solutions was measured every minute for 340 min. The pH values of the solutions are shown in Figure 6(a). In the case of the polymer blend without molybdenum trioxide (curve A), the pH value reached a saturation value of 5.3 in 90 min. In the case of the molybdenum trioxide nanocomposite (curve B), the pH value dropped to 4.6 in the first 5 min and approached 3.8 after 6 h. The temporal development of the concentration of dissolved molybdenum trioxide NWs is presented in Figure 6(b). After a relatively short time, about 90 min, the concentration of molybdenum trioxide dissolved from the nanocomposite reached a saturation value of 0.09 mg/ml.

3.6 Antimicrobial activity

The antimicrobial properties of the PVDF-HFP/PVP/molybdenum trioxide nanocomposite were tested against Gram-positive bacteria *S. aureus* and *L. monocytogenes* (Figure 7(a)), Gram-negative

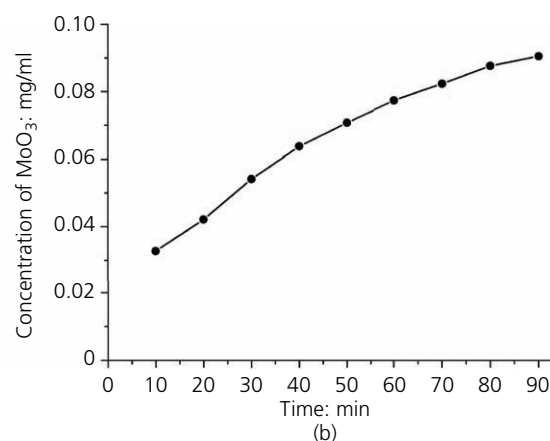


Figure 6. (a) Time evolution of pH values during dissolution in water of the PVDF-HFP/PVP blend (curve A) and PVDF-HFP/PVP/molybdenum trioxide nanocomposite (curve B); (b) concentration of dissolved molybdenum trioxide from the nanocomposite

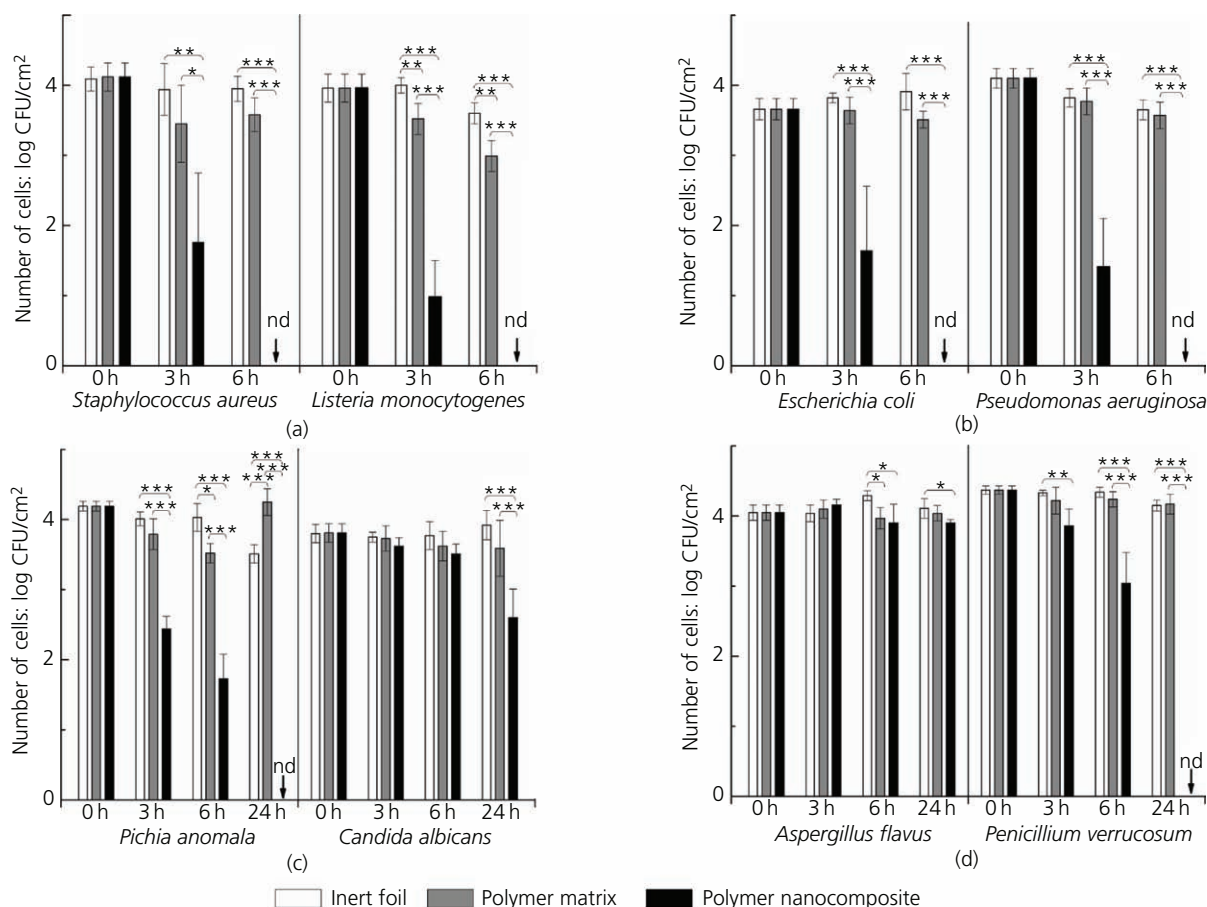


Figure 7. Kinetics of the antimicrobial activity of inert PE foil (empty columns), PVDF-HFP/PVP blend (grey columns) and PVDF-HFP/PVP/molybdenum trioxide nanocomposite (black columns) against (a) Gram-positive bacteria (*S. aureus* and *L. monocytogenes*), (b) Gram-negative bacteria (*E. coli* and *P. aeruginosa*), (c) yeasts (*C. albicans* and *P. anomala*) and (d) moulds (*P. verrucosum* and *A. flavus*). The abbreviation 'nd' means that the presence of microorganism was not detected. Asterisks indicate statistically significant difference (* $p < 0.05$; ** $p < 0.01$; *** $p < 0.001$) between the compared parameters for each microorganism at a given time

bacteria *E. coli* and *P. aeruginosa* (Figure 7(b)), yeasts *C. albicans* and *P. anomala* (Figure 7(c)) and moulds *P. verrucosum* and *A. flavus* (Figure 7(d)). An inert PE foil was used as the negative control. A pure PVDF-HFP/PVP polymer blend was also tested and showed a statistically significant reduction in *L. monocytogenes* after 3 and 6 h. A reduction was also observed in *P. anomala* and *A. flavus* after 6 h, but these differences were no longer present after 24 h.

The antimicrobial activity of the PVDF-HFP/PVP/molybdenum trioxide nanocomposite was more pronounced against bacteria compared with that against fungi. The reduction trend in the number of colonies is evident for all four tested bacteria with a statistically significant reduction of 2–3 log after 3 h of incubation and with a complete bactericidal effect in 6 h (Figures 7(a) and 7(b)). For the yeasts, the antimicrobial effect was stronger against *P. anomala*, with statistically significant reductions of 1.7 log and 2.5 log in 3 and 6 h of incubation, respectively, and a fungicidal effect in 24 h (Figure 7(c)). The number of colonies of *C. albicans* was reduced less, but a

statistically significant reduction of 1.2 log in 24 h was achieved (Figure 7(c)). Species-specific differences in antimicrobial activity were also observed in the moulds, where the nanocomposite reduced the number of *P. verrucosum* already after 3 h with a reduction of 0.5 log in 3 h and by 1.3 log in 6 h in a statistically significant way and showed a fungicidal effect in 24 h. In the case of *A. flavus*, however, this difference was observed after 6 and 24 h (Figure 7(d)).

4. Discussion

The growth of microbes on different surfaces depends on several physical and chemical conditions. The most important physical conditions are the appropriate temperature, pH value, surface topography and the presence of water, while the most important chemical condition is the availability of nutrients. The physical properties of the surface, such as topography, wetting angle and surface zeta potential, influence the adhesion of microbes and their interaction with the surface. The surface roughness (R_a) of the investigated foils determined with AFM was 420 nm for the PVDF-HFP/PVP blend and half (210 nm) for the PVDF-HFP/

PVP/molybdenum trioxide nanocomposite. It is already known that a small increase in the average surface roughness (R_a) value reduces bacterial adhesion.⁴³ The addition of molybdenum trioxide NWs to the PVDF-HFP/PVP blend causes a slightly higher CA of the PVDF-HFP/PVP/molybdenum trioxide nanocomposite. Nevertheless, both foils retain their hydrophilic character, which is unfavourable for the attachment of microorganisms.⁴⁴ The existence of the β -phase of PVDF-HFP both in the pure polymer blend and in the nanocomposite is explained by an interaction between the $>CF_2$ group of PVDF and the carbonyl groups of PVP, as reported for the case of esters.⁴⁵

Both PVP and molybdenum trioxide are water soluble and lower the pH value of the solutions towards the acidic region. The slightly acidic solution of PVP is explained by the carboxyl groups that are located at the beginning of each PVP chain.⁴⁶ The high specific surface area of molybdenum trioxide NWs leads to a very rapid dissolution in water. In the first step, molybdic acid is formed, which then dissociates further to form molybdate and hydroxonium ions.¹³ The acidic environment of the dissolving molybdenum trioxide NWs intensifies the hydrolysis reaction of the PVP polymer. It has been reported that the rate constant of the hydrolysis/hydration reaction of PVP in water increases with acidity.⁴⁶ The dependence of the co-operative solubility is evident from the time dependence of the pH value, which in the case of a polymer blend solution reached the final pH value (5.3) in 1.5 h, while it decreased steadily to 3.8 in 6 h due to the dissolution of the nanocomposite. The solubility also influences the distribution of the surface charge. The zeta potential of the polymer blend is -26.3 mV, indicating the presence of negatively charged ions during the dissolution of PVP. The addition of molybdenum trioxide NWs to the polymer blend causes a change in the zeta potential from negative to positive, probably due to the protonation of the carboxylate anions. The interaction between the molybdenum trioxide NWs and the PVP polymer is also evident in the emergence of two new Raman peaks at 957 and 987 cm^{-1} and in the thermal stabilisation of the PVDF-HFP component of the blend with added molybdenum trioxide, which increased the complex elastic modulus E^* over the entire temperature range.

A consistent and statistically significant antimicrobial activity of the polymer blend was observed only for the Gram-positive bacterium *L. monocytogenes*, but the polymer also reduced *S. aureus* for 0.5 log after 6 h of incubation. This is consistent with a report that the polymers are generally more active against Gram-positive bacteria due to the difference in cell membrane structure.⁴⁷ The PVDF-HFP/PVP/molybdenum trioxide nanocomposite proved to have good bactericidal activity, as it inactivated both Gram-positive and Gram-negative bacteria after 6 h of incubation. However, species-specific differences were observed in fungi, as the nanocomposite was fungicidal against yeast *P. anomala* and mould *P. verrucosum* but only reduced the number of yeast *C. albicans* and mould *A. flavus*. This can be explained by the optimal growth rate of *A. flavus* in the pH range of 3.5–6.0,⁴⁸ while *C. albicans* has the ability to adapt to changes in extracellular pH and colonise tissues with diverse pH in vivo.⁴⁹

5. Conclusion

A novel nanostructured polymer composite was designed from inert biocompatible PVDF-HFP and water-soluble PVP polymers with incorporated molybdenum trioxide NWs. The nanofiller reduces the surface roughness, increases the wetting angle, changes the zeta potential from negative to positive, increases the thermal stability of the blend and preserves the polar β -phase in PVDF-HFP caused by the interaction between the two polymers. The high specific surface area of molybdenum trioxide NWs allows a fast dissolution and a consequent reduction in the pH value. The acidic environment enables hydrolysis of the PVP polymer, which could contribute to the antimicrobial function by forming carboxyl acid and ammonium salt. The synergy in the dissolving processes for PVP and molybdenum trioxide leads to sufficiently low pH values, although a relatively small amount of molybdenum trioxide (0.09 mg/ml in 1.5 h) is released from the nanocomposite. These characteristics indicate that the PVDF-HFP/PVP/molybdenum trioxide nanocomposite is a stable nanostructured coating that has a good antimicrobial potential and is unfavourable for colonisation by microorganisms. The advantage of the reported PVDF-HFP/PVP/molybdenum trioxide nanocomposite is the activation of its antimicrobial effect by water. Instead of using different disinfectants with different degrees of toxicity, which require frequent applications, the PVDF-HFP/PVP/molybdenum trioxide nanocomposite dissolves in water during the cleaning process or in water brought along by adhering microbes or condensed from the air humidity. The potential of its long-term antimicrobial and virucidal activity needs further investigation.

Acknowledgements

This work was financially supported by the Slovenian Research Agency through contracts P0-5544, P1-0099 and P4-0116. The authors thank Dr A. Abram for help with measurements of surface zeta potentials and static CAs and Dr L. Pirker for help in the synthesis of the molybdenum trioxide NWs. The authors thank in particular J. Žigon and Professor Dr M. Petrič for help with measurements of dynamic CAs.

REFERENCES

1. Satpathy S, Sen SK, Pattanaik S and Raut S (2016) Review on bacterial biofilm: an universal cause of contamination. *Biocatalysis and Agricultural Biotechnology* 7: 56–66.
2. Palza H (2015) Antimicrobial polymers with metal nanoparticles. *International Journal of Molecular Sciences* 16: 2099–2116.
3. Glinel K, Thebault P, Humblot V, Pradier CM and Jouenne T (2012) Antibacterial surfaces developed from bio-inspired approaches. *Acta Biomaterialia* 8: 1670–1684.
4. Vasilev K, Cook J and Griesser HJ (2009) Antibacterial surfaces for biomedical devices. *Expert Review of Medical Devices* 6(5): 553–567.
5. Thome J, Holländer A, Jaeger W, Trick I and Oehr C (2003) Ultrathin antibacterial polyammonium coatings on polymer surfaces. *Surface and Coatings Technology* 174–175: 584–587.
6. Greenhalgh R, Dempsey-Hibbert NC and Whitehead KA (2019) Antimicrobial strategies to reduce polymer biomaterial infections and their economic implications and considerations. *International Biodeterioration & Biodegradation* 136: 1–14.

7. Ogunsona EO, Muthuraj R, Ojogbo E, Valerio O and Mekonnen TH (2020) Engineered nanomaterials for antimicrobial applications: a review. *Applied Materials Today* **18**: article 100473.
8. Guo L, Yuan W, Lu Z and Li CM (2013) Polymer/nanosilver composite coatings for antibacterial applications. *Colloids and Surfaces A: Physicochemical and Engineering Aspects* **439**: 69–83.
9. Schwartz VB, Thétiot F, Ritz S et al. (2012) Antibacterial surface coatings from zinc oxide nanoparticles embedded in poly(*N*-isopropylacrylamide) hydrogel surface layers. *Advanced Functional Materials* **22(11)**: 2376–2386.
10. Charpentier PA, Burgess K, Wang L et al. (2012) Nano-TiO₂/polyurethane composites for antibacterial and self-cleaning coatings. *Nanotechnology* **23**: article 425606.
11. Bondarenko O, Juganson K, Ivask A et al. (2013) Toxicity of Ag, CuO and ZnO nanoparticles to selected environmentally relevant test organisms and mammalian cells in vitro: a critical review. *Archives of Toxicology* **87(7)**: 1181–1200.
12. Shafaei S, Lackner M, Meier M et al. (2013) Polymorphs of molybdenum trioxide as innovative antimicrobial materials. *Surface Innovations* **1(4)**: 202–208, <https://doi.org/10.1680/si.13.00021>.
13. Zollfrank C, Gutbrod K, Wechsler P and Guggenbichler JP (2012) Antimicrobial activity of transition metal acid MoO₃ prevents microbial growth on material surfaces. *Materials Science and Engineering: C* **32**: 47–54.
14. Krishnamoorthy K, Veerapandian M, Yun K and Kim SJ (2013) New function of molybdenum trioxide nanoplates: toxicity towards pathogenic bacteria through membrane stress. *Colloids and Surfaces B: Biointerfaces* **112**: 521–524.
15. Kumar A and Pandey G (2017) Synthesis, characterization, effect of temperature on band gap energy of molybdenum oxide nano rods and their antibacterial activity. *American Journal of Applied and Industrial Chemistry* **3(3)**: 38–42.
16. Desai N, Mali S, Kondalkar V, Mane R and Hong C (2015) Chemically grown MoO₃ nanorods for antibacterial activity study. *Journal of Nanomedicine & Nanotechnology* **6**: 338–344.
17. Chaves-Lopez C, Nguyen HN, Oliveira RC et al. (2018) A morphological, enzymatic and metabolic approach to elucidate apoptotic-like cell death in fungi exposed to h- and α-molybdenum trioxide nanoparticles. *Nanoscale* **10(44)**: 20702–20716.
18. Laxmayyaguddi Y, Mydur N, Shankar Pawar A et al. (2018) Modified thermal, dielectric, and electrical conductivity of PVDF-HFP/LiClO₄ polymer electrolyte films by 8 MeV electron beam irradiation. *ACS Omega* **3**: 14188–14200.
19. Sundaram NTK and Subramania A (2007) Microstructure of PVDF-co-HFP based electrolyte prepared by preferential polymer dissolution process. *Journal of Membrane Science* **289(1–2)**: 1–6.
20. Malmonge LF, Malmonge JA and Sakamoto WK (2003) Study of pyroelectric activity of PZT/PVDF-HFP composite. *Materials Research* **6(4)**: 469–473.
21. Cao JH, Zhu BK and Xu YY (2006) Structure and ionic conductivity of porous polymer electrolytes based on PVDF-HFP copolymer membranes. *Journal of Membrane Science* **281**: 446–453.
22. Shawky AI, Noor MJMM, Nasef MM et al. (2016) Enhancing antimicrobial properties of poly(vinylidene fluoride)/hexafluoropropylene copolymer membrane by electron beam induced grafting of *N*-vinyl-2-pyrrolidone and iodine immobilization. *RSC Advances* **6**: 42461–42473.
23. Guo Z, Xu X, Xiang Y, Lu SA and Jiang SP (2015) New anhydrous proton exchange membranes for high-temperature fuel cells based on PVDF-PVP blended polymers. *Journal of Materials Chemistry A* **3(1)**: 148–155.
24. Wang M, Fang D, Wang N et al. (2014) Preparation of PVDF/PVP core-shell nanofibers mats via homogeneous electrospinning. *Polymer* **55**: 2188–2196.
25. Yao C, Li X, Neoh KG, Shi Z and Kang ET (2009) Antibacterial activities of surface modified electrospun poly(vinylidene fluoride-co-hexafluoropropylene) (PVDF-HFP) fibrous membranes. *Applied Surface Science* **255(6)**: 3854–3858.
26. Varlec A, Arčon D, Škapin SD and Remškar M (2016) Oxygen deficiency in MoO₃ polycrystalline nanowires and nanotubes. *Materials Chemistry and Physics* **170**: 154–161.
27. Božinović K, Nestić D, Gradišar Centa U et al. (2020) In-vitro toxicity of molybdenum trioxide nanoparticles on human keratinocytes. *Toxicology* **444**: article 152564.
28. Zhang Y, Yang M, Portney NG et al. (2008) Zeta potential: a surface electrical characteristic to probe the interaction of nanoparticles with normal and cancer human breast epithelial cells. *Biomedical Microdevices* **10**: 321–328.
29. Wilhelmly J (1863) Über die Abhängigkeit der Kapillaritäts-Konstanten des Alkohols von Substanz und Gestalt des Benetzten Festen Körpers. *Annalen der Physik* **119**: 177–217 (in German).
30. Ström G, Fredriksson M and Stenius P (1987) Contact angles, work of adhesion, and interfacial tensions at a dissolving Hydrocarbon surface. *Journal of Colloid and Interface Science* **119(2)**: 352–361.
31. ISO (International Organization for Standardization) (2007) ISO 22196:2007: Plastics – measurement of antibacterial activity on plastics surfaces. ISO, Geneva, Switzerland.
32. Kalampounias AG, Tsilomelekis G, Berg RW and Boghosian S (2012) Molybdenum(VI) oxosulfato complexes in MoO₃-K₂S₂O₇-K₂SO₄ molten mixtures: stoichiometry, vibrational properties, and molecular structures. *Journal of Physical Chemistry A* **116(35)**: 8861–8872.
33. Sharma RK and Reddy GB (2014) Synthesis and characterization of α-MoO₃ microspheres packed with nanoflakes. *Journal of Physics D: Applied Physics* **47(6)**: article 065305.
34. Singh P, Borkar H, Singh BP, Singh VN and Kumar A (2014) Ferroelectric polymer-ceramic composite thick films for energy storage application. *AIP Advances* **4**: article 087117.
35. Beattie IR and Gilson TR (1969) Oxide phonon spectra. *Journal of the Chemical Society A: Inorganic, Physical, Theoretical* **969**: 2322–2327.
36. Dieterle M and Mestl G (2002) Raman spectroscopy of molybdenum oxides. *Physical Chemistry Chemical Physics* **4**: 822–826.
37. Turner DT and Schwartz A (1985) The glass transition temperature of poly(*N*-vinyl pyrrolidone) by differential scanning calorimetry. *Polymer* **26**: 757–762.
38. Remškar M, Iskra I, Jelenc J et al. (2013) A novel structure of polyvinylidene fluoride (PVDF) stabilized by MoS₂ nanotubes. *Soft Matter* **9**: 8647–8653.
39. Strobel M and Lyons CS (2011) An essay on contact angle measurements. *Plasma Processes and Polymers* **8(1)**: 8–13.
40. Manoudis PN and Karapanagiotis I (2013) Modification of the wettability of polymer surfaces using nanoparticles. *Progress in Organic Coatings* **77**: 331–338.
41. Juárez-Moreno JA, Ávila-Ortega A, Oliva AI and Cauch-Rodríguez JV (2015) Effect of wettability and surface roughness on the adhesion properties of collagen on PDMS films treated by capacitively coupled oxygen plasma. *Applied Surface Science* **349**: 763–773.
42. Cai K, Bossert J and Jandt KD (2006) Does the nanometre scale topography of titanium influence protein adsorption and cell proliferation? *Colloids and Surfaces B: Biointerfaces* **49(2)**: 136–144.
43. Taylor RL, Verran J, Lees GC and Ward AJP (1998) The influence of substratum topography on bacterial adhesion to polymethyl methacrylate. *Journal of Materials Science: Materials in Medicine* **9**: 17–22.
44. Oliveira R, Azeredo J, Teixeira P and Fonseca AP (2001) The role of hydrophobicity in bacterial adhesion. In *Biofilm Community Interactions: Chance or Necessity?* (Gilbert P, Allison D, Brading M, Verran J and Walker J (eds)). BioLine, Cardiff, UK, pp. 11–22. See <http://citeseerx.ist.psu.edu/viewdoc/download?doi=10.1.1.625.340&rep=rep1&type=pdf> (accessed 11/12/2020).

-
45. Manna S and Nandi AK (2007) Piezoelectric β polymorph in poly (vinylidene fluoride)-functionalized multiwalled carbon nanotube nanocomposite films. *Journal of Physical Chemistry C* **111**: 14670–14680.
 46. Frank HP (1954) The lactam-amino acid equilibria for ethylpyrrolidone and polyvinylpyrrolidone. *Journal of Polymer Science* **12**: 565–576.
 47. Tashiro T (2001) Antibacterial and bacterium adsorbing macromolecules. *Macromolecular Materials and Engineering* **286**: 63–87.
 48. Kosegarten CE, Ramírez-Corona N, Mani-López E, Palou E and López-Malo A (2017) Description of *Aspergillus flavus* growth under the influence of different factors (water activity, incubation temperature, protein and fat concentration, pH, and cinnamon essential oil concentration) by kinetic, probability of growth, and time-to-detection models. *International Journal of Food Microbiology* **240**: 115–123.
 49. Davis D (2003) Adaptation to environmental pH in *Candida albicans* and its relation to pathogenesis. *Current Genetics* **44**: 1–7.

How can you contribute?

To discuss this paper, please submit up to 500 words to the journal office at journals@ice.org.uk. Your contribution will be forwarded to the author(s) for a reply and, if considered appropriate by the editor-in-chief, it will be published as a discussion in a future issue of the journal.

ICE Science journals rely entirely on contributions from the field of materials science and engineering. Information about how to submit your paper online is available at www.icevirtuallibrary.com/page/authors, where you will also find detailed author guidelines.



Article

Synthesis and Characterization of Tungsten Suboxide W_nO_{3n-1} Nanotiles

Luka Pirker ^{1,†}, Bojana Višić ^{1,2,*,†}, Janez Kovač ¹, Srečo D. Škapin ¹ and Maja Remškar ^{1,3}

¹ Jožef Stefan Institute, Jamova Cesta 39, 1000 Ljubljana, Slovenia; luka.pirker@ijs.si (L.P.); janez.kovac@ijs.si (J.K.); sreco.skapin@ijs.si (S.D.Š.); maja.remskar@ijs.si (M.R.)

² Institute of Physics Belgrade, University of Belgrade, Pregrevica 118, 11080 Belgrade, Serbia

³ Faculty for Mathematics and Physics, University of Ljubljana, Jadranska Ulica 19, 1000 Ljubljana, Slovenia

* Correspondence: bojana.visic@ipb.ac.rs

† These authors contributed equally.

Abstract: W_nO_{3n-1} nanotiles, with multiple stoichiometries within one nanotile, were synthesized via the chemical vapour transport method. They grow along the [010] crystallographic axis, with the thickness ranging from a few tens to a few hundreds of nm, with the lateral size up to several μm . Distinct surface corrugations, up to a few 10 nm deep appear during growth. The $\{102\}_r$ crystallographic shear planes indicate the W_nO_{3n-1} stoichiometries. Within a single nanotile, six stoichiometries were detected, namely $W_{16}O_{47}$ ($WO_{2.938}$), $W_{15}O_{44}$ ($WO_{2.933}$), $W_{14}O_{41}$ ($WO_{2.928}$), $W_{13}O_{38}$ ($WO_{2.923}$), $W_{12}O_{35}$ ($WO_{2.917}$), and $W_{11}O_{32}$ ($WO_{2.909}$), with the last three never being reported before. The existence of oxygen vacancies within the crystallographic shear planes resulted in the observed non-zero density of states at the Fermi energy.

Keywords: tungsten oxides; nanotiles; nanomaterials



Citation: Pirker, L.; Višić, B.; Kovač, J.; Škapin, S.D.; Remškar, M. Synthesis and Characterization of Tungsten Suboxide W_nO_{3n-1} Nanotiles. *Nanomaterials* **2021**, *11*, 1985. <https://doi.org/10.3390/nano11081985>

Academic Editor: Jeremy Sloan

Received: 6 July 2021

Accepted: 30 July 2021

Published: 2 August 2021

Publisher's Note: MDPI stays neutral with regard to jurisdictional claims in published maps and institutional affiliations.



Copyright: © 2021 by the authors. Licensee MDPI, Basel, Switzerland. This article is an open access article distributed under the terms and conditions of the Creative Commons Attribution (CC BY) license (<https://creativecommons.org/licenses/by/4.0/>).

1. Introduction

In the family of transition metal oxide materials, semiconducting WO_3 is among the most studied, due to its promising practical applications. It has already been successfully used as a catalyst for water splitting [1], in gas/temperature sensors [2,3], in optoelectronics [4], or as a component in supercapacitors [5]. The crystal structure of WO_3 is usually described in terms of corner-sharing WO_6 octahedra. The structure can differ from the ideal cubic ReO_3 type structure due to different tilting angles, displacement of the W cation, and rotation of WO_6 octahedra. Its phase transitions have been thoroughly studied [6–9], and various nanometre-sized particles, nanowires and flakes were synthesized [10,11].

The sub-stoichiometric tungsten oxide phases, WO_{3-x} , with $0 < x < 1$, provide the opportunity to synthesize and study nanoparticles with great variety of shapes, sizes and physical properties. According to the literature, for $x \leq 0.2$, the WO_{3-x} crystallize into phases with the chemical formula W_nO_{3n-1} or W_nO_{3n-2} , which are often referred to as Magnéli phases [12,13]. The W_nO_{3n-1} stoichiometry crystallizes in the $P2/a$ symmetry with a monoclinic unit cell containing two W_nO_{3n-1} moieties, while the W_nO_{3n-2} crystallizes in the $P2/m$ symmetry in a monoclinic unit cell with one W_nO_{3n-2} moiety. The oxygen deficiency present in WO_{3-x} is compensated with the formation of crystallographic shear (CS) planes, where some of the corner-sharing WO_6 octahedra become edge-sharing. In W_nO_{3n-1} structures, four WO_6 octahedra are joined by edges, while in W_nO_{3n-2} the number of these octahedra is six. With further reduction ($x > 0.2$), edge and face-sharing WO_6 octahedra emerge, forming pentagonal columns and hexagonal tunnels [14]. The crystal structures of these materials are found to be orthorhombic for $W_{32}O_{84}$ and W_3O_8 , monoclinic for $W_{18}O_{49}$, $W_{17}O_{47}$, $W_{20}O_{58}$, and $W_{25}O_{73}$, and tetragonal for W_5O_{14} [15]. These varieties stem from different oxygen deficiencies within the nanostructures [16,17].

Here, we report on new tungsten suboxide nanostructures crystallized in the form of nanotiles. The nanotiles are composed of different W_nO_{3n-1} stoichiometries, three of which were observed for the first time. High-resolution transmission electron microscopy (HRTEM), scanning electron microscopy (SEM), X-ray diffraction (XRD), Raman spectroscopy, X-ray photoelectron spectroscopy (XPS) and atomic force microscopy (AFM) were used to characterize the nanotiles.

2. Materials and Methods

2.1. Synthesis

The nanotiles were synthesized via the chemical vapour transport reaction (CVT). Iodine was used as the transport agent and nickel as the growth promoter. Quartz ampules were filled with 352.7 mg of WO_3 powder (Sigma-Aldrich, St. Louis, MO, USA, 99.99%), 37.5 mg of nickel (metal foil) and 562 mg of iodine (1–3 mm beads, Sigma-Aldrich, St. Louis, MO, USA, 99.7%). Ampules were evacuated down to 10^{-5} mbar, and the transport reaction was running for 500 h. The material was transported from hot zone of the furnace (1133K) to the growth zone (1009K).

2.2. X-ray Diffraction

X-ray diffraction (XRD) was performed using a D4 Endeavor diffractometer (Bruker AXS GmbH, Karlsruhe, Germany) at room temperature. A quartz monochromator Cu K α 1 radiation source ($\lambda = 0.1541$ nm) and a Sol-X energy dispersive detector were used. The angular range (2θ) was in the range from 10° to 70° , with a step size of 0.02° and collection time of 4 s.

2.3. Raman Spectroscopy

Raman spectra of the nanotiles were recorded by an Alpha300 R (WITec, Ulm, Germany) confocal Raman imaging system. Measurements were performed in backscattered geometry using a frequency doubled Nd:YAG laser (532 nm). The laser power was kept under 5 mW for standard measurements (to prevent oxidation and damage of the material). For laser power dependence studies, the power was varied from 0.06 mW to 24.7 mW. The sample was dispersed in ethanol and drop-casted on a chromium plate as a substrate with a featureless Raman spectrum.

2.4. Scanning Electron Microscopy

Scanning electron microscopy (SEM) images and cross-sections of the samples for TEM analysis were obtained using a Helios NanoLab 650 (Thermo Fisher, Waltham, MA, USA) Focused Ion Beam-scanning electron microscope (FIB). The nanotiles were drop-casted on a silicon wafer for SEM studies.

2.5. High-Resolution Transmission Electron Microscopy and Electron Diffraction

High-resolution transmission electron microscopy (HRTEM) and electron diffraction (ED) images were acquired using a Cs probe-corrected TEM/STEM JEOL ARM 200CF (JEOL, Peabody, MA, USA) microscope equipped with a cold-FEG electron source, operating at 200 kV. Distances between atomic columns and angles between their rows were measured using Digital Micrograph software. An accuracy of 0.04 Å in distance and 0.5° in angle was achieved. All HRTEM images were filtered using the Average Background Subtraction Filter method described in [18].

2.6. Atomic Force Microscopy

Atomic force microscopy (AFM) in contact mode was performed with an Omicron UHV VT-AFM (Scienta Omicron, Taunusstein, Germany) operating at 10^{-9} mbar. Silicon Cantilevers CSG10 (NT-MDT, Moscow, Russia) with a typical force constant of 0.11 N/m were used.

2.7. X-ray Photoelectron Spectroscopy

X-ray photoelectron spectroscopy XPS analysis was carried out on the PHI-TFA XPS spectrometer produced by Physical Electronics, Chanhassen, MN, USA. Samples were mounted on the metallic sample holder and introduced in ultra-high vacuum spectrometer. The vacuum during the XPS analyses was in the range of 10^{-9} mbar. The analysed area was 0.4 mm in diameter and the analysed depth was about 3–5 nm. Sample surfaces were excited by X-ray radiation from monochromatic Al source at photon energy of 1486.6 eV. The high-energy resolution spectra were acquired with energy analyser operating at resolution of about 0.6 eV and pass energy of 29 eV. The accuracy of binding energies was about ± 0.2 eV. Three places on every sample were analysed. High resolution spectra were fitted with Gauss-Lorentz functions and Shirley function was used for background removal. For the XPS measurements, the ethanol suspension of nanotiles was deposited on an oxidized Si wafer, dried at room temperature and inserted into ultra-high vacuum of the spectrometer.

3. Results

3.1. Electron Microscopy

The nanotiles, depicted in Figure 1, grow on the ampule walls in the form of a blue powder. A single nanotile usually grows in a rectangular shape, a few micrometres in width and up to 10 μm in length, as shown in Figure 1. The thickness of the nanotiles varies from a few 10 nm up to a few 100 nm, as seen in Figure S1 and Figure 1. They have distinct corrugations, which can be up to a few 10 nm deep, as seen in Figure 2. To determine the structure of the nanotiles, two cross-section lamellas perpendicular and parallel to the corrugations were prepared for further TEM analysis, as shown in Figure 1a.

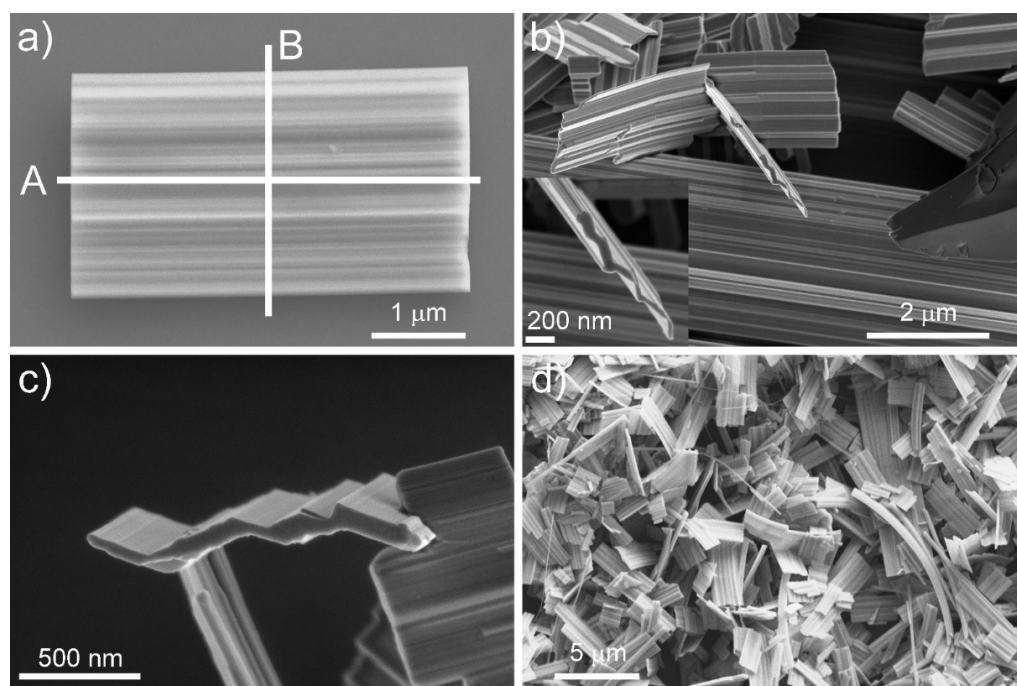


Figure 1. (a) A single nanotile, with lines A and B representing the direction of the cross-sections for the TEM lamellas; (b–d) SEM images of different nanotiles.

An HRTEM image of the cross-section lamella B is shown in Figure 3a and Figure S2. Figure 3a was taken along the [010] direction, and was used to determine the stoichiometry of the nanotiles. The parallel contrast lines are crystallographic shear (CS) planes, which are characteristic for W_nO_{3n-1} and W_nO_{3n-2} phases. Only $\{102\}_r$ CS planes were observed, indicating that only W_nO_{3n-1} structures grow inside the nanotiles [12,19]. Six stoichiometries were determined by measuring the unit cell parameters a , c , and β : $W_{16}O_{47}$ ($WO_{2.938}$),

$W_{15}O_{44}$ ($WO_{2.933}$), $W_{14}O_{41}$ ($WO_{2.928}$), $W_{13}O_{38}$ ($WO_{2.923}$), $W_{12}O_{35}$ ($WO_{2.917}$), and $W_{11}O_{32}$ ($WO_{2.909}$), of which the last three were not experimentally observed to date [20]. The unit cell parameters a , c , and β of the observed phases are presented in Table 1. The a axis is oriented along the CS planes, while the c axis is directed towards the CS plane at the angle β , relative to axis a . An electron diffraction was performed on lamella A, Figure 3b. The reflections (010) , $(40\bar{3})$ and $(41\bar{3})$ correspond to interlayer distances of 3.79 Å, 3.56 Å, and 2.61 Å, respectively. The first estimation of the unit cell parameter b was determined from the (010) reflection with the value of 3.79 Å. The second value for b (3.86 Å) was determined from the average distance between the tungsten atoms that are not part of the CS planes. The mean value of the unit cell parameter b is 3.83 Å. The theoretical tungsten atom positions and unit cell parameters for the newly observed phases were calculated using the model proposed in ref. [12]. The parameters d and e used in the model were determined from the HRTEM and electron diffraction images and are schematically shown in Figure S3: (i) interatomic distance between tungsten atoms that are not part of the CS plane that should equal unit cell parameter b ($d = 3.83$ Å); (ii) interatomic distance between tungsten atoms that are part of the CS plane, where the tungsten octahedra are joined by edges ($e = 2.92$ Å). The experimental unit cell parameters are in good agreement with the calculated ones. The unit cells are schematically drawn on the HRTEM and simulated structure images and are shown in Figure 4.

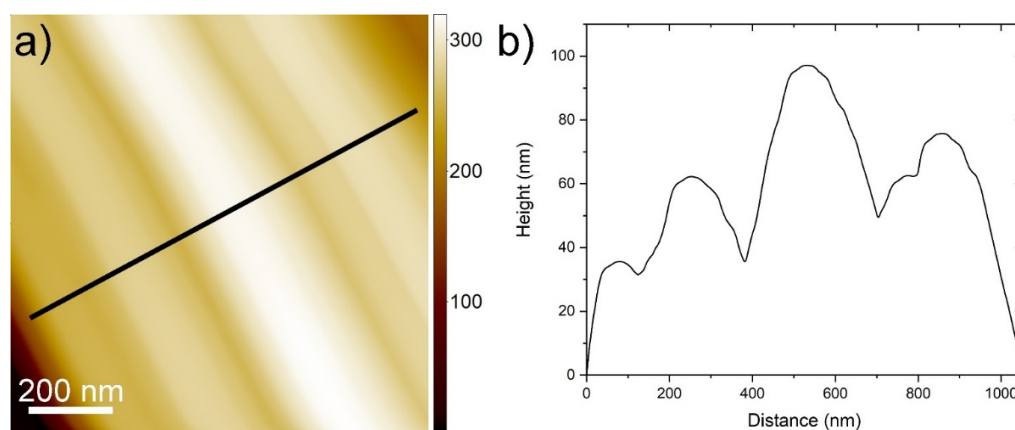


Figure 2. (a) An AFM image of a nanotile with a line profile showing corrugations in (b).

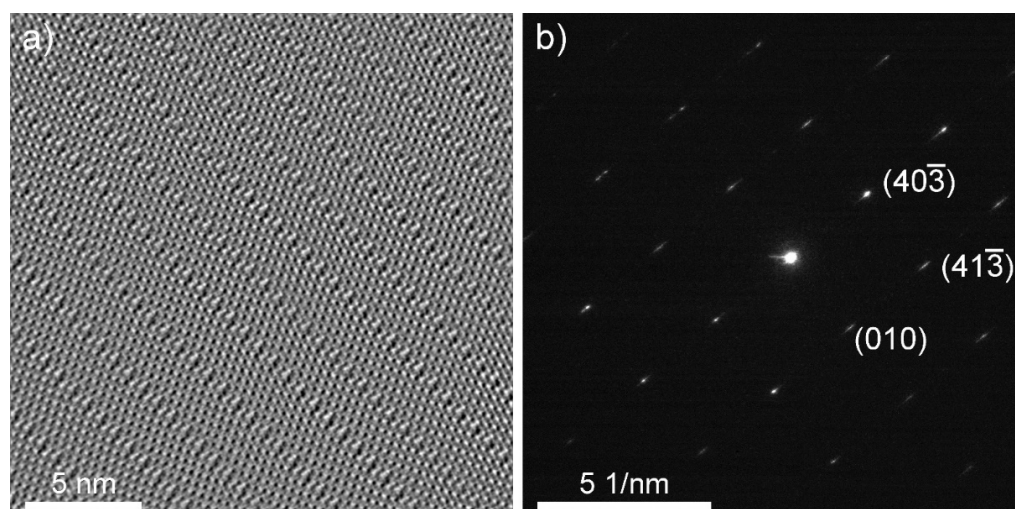
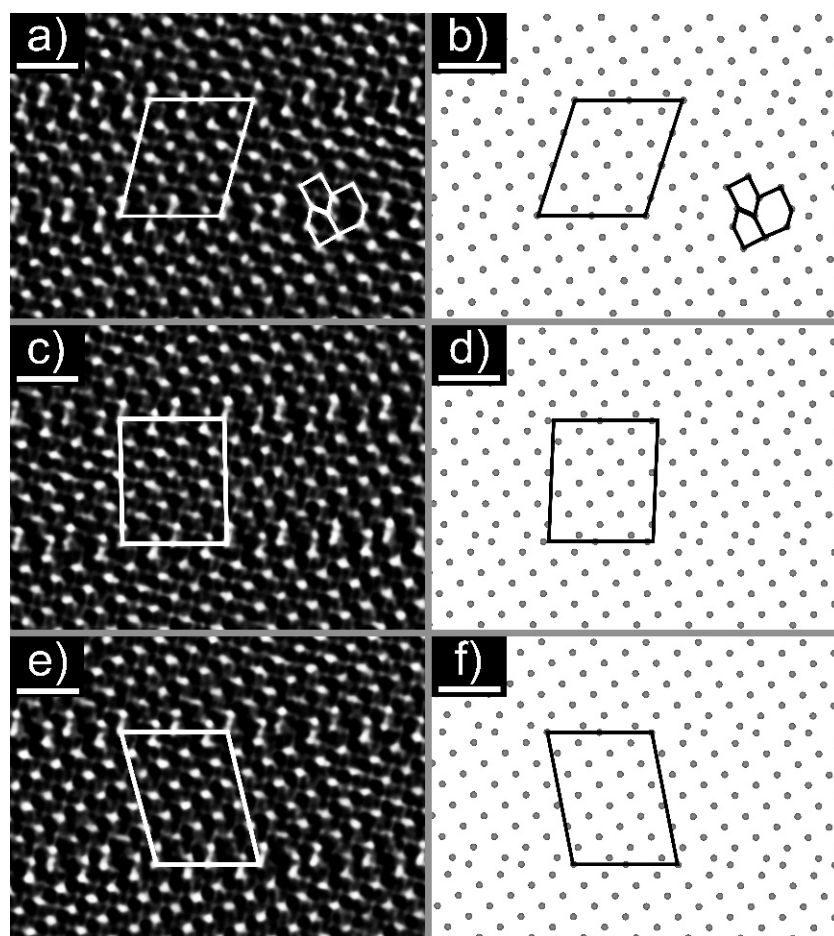


Figure 3. (a) HRTEM image along the $[010]$ direction (lamella B). (b) An electron diffraction of the $[304]$ zone (lamella A).

Table 1. Measured and calculated unit cell parameters for observed phases.

Structure	Measured				Calculated			
	a (Å)	b (Å)	c (Å)	β (°)	a (Å)	b (Å)	c (Å)	β (°)
$W_{11}O_{32}$	17.3	3.83	18.9	79.3	17.1	>3.83	19.2	72.2
$W_{12}O_{35}$	17.3	3.83	20.2	89.6	17.1	>3.83	20.0	87.9
$W_{13}O_{38}$	17.3	3.83	22.5	103.7	17.1	>3.83	22.1	101.5
$W_{14}O_{41}$	17.3	3.83	24.5	74.2	17.1	>3.83	24.6	72.0
$W_{15}O_{43}$	17.3	3.83	25.6	88.0	17.1	>3.83	25.2	84.4
$W_{16}O_{47}$	17.3	3.83	27.5	98.3	17.1	>3.83	26.9	95.7

**Figure 4.** HRTEM images of: (a) $W_{11}O_{32}$, (c) $W_{12}O_{35}$, and (e) $W_{13}O_{38}$ with the proposed unit cell. The scale bar is 1 nm. Simulated structures of: (b) $W_{11}O_{32}$, (d) $W_{12}O_{35}$, and (f) $W_{13}O_{38}$ with the proposed unit cell.

3.2. X-ray Diffraction

The XRD pattern of the nanotiles is shown in Figure 5. Due to their multi-stoichiometric structure, the XRD pattern is composed of diffraction lines corresponding to all tungsten suboxide phases present in the nanotiles. The low-angle diffraction lines were used to determine the most prominent phase, as they are different for each stoichiometry and do not overlap with the $m\text{-WO}_3$ phase. The measured diffractogram had the best match with the $W_{14}O_{41}$ ($WO_{2.928}$) stoichiometry, indicating that this is the phase the majority of the nanotiles crystallize in. The position of the diffraction lines, their relative intensities and the assigned (hkl) indices, are presented in Table 2. Additionally, the (010) line closely matches with the b unit cell parameter obtained from the HRTEM images. In Figure 5, the measured XRD pattern is compared to the $m\text{-WO}_3$ one (PDF2: 01-072-1465).

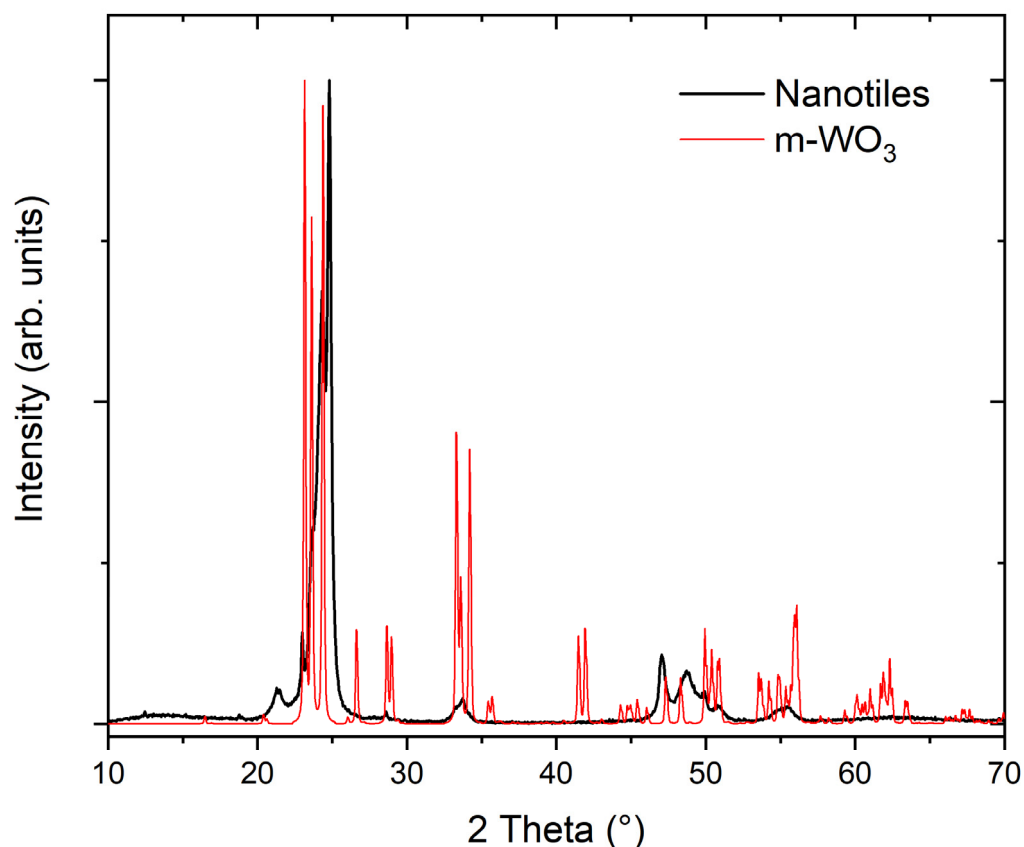


Figure 5. XRD pattern of the WO_{3-x} nanotiles and of $m\text{-WO}_3$ (PDF2: 01-072-1465).

Table 2. Measured XRD diffraction lines (positions in $^\circ$ and \AA) and their relative intensities compared with the calculated d values using parameters obtained from HRTEM images and the assigned (hkl) indices.

2 Theta ($^\circ$)	Measured d (\AA)	Rel. Int.	Theoretical $\text{W}_{14}\text{O}_{41}$ Assigned Index (hkl)	d (\AA)
12.5	7.08	0.02	(20 $\bar{3}$)	7.04
18.8	4.70	0.01	(005)	4.68
21.5	4.13	0.05	(403)	4.17
23.2	3.84	0.14	(010)	3.83
23.9	3.73	0.30	(110)	3.73
24.5	3.63	0.66	(112)	3.63
25.0	3.56	1.00	(402)	3.52
28.9	3.09	0.02	(407)	3.09
34.2	2.62	0.04	(21 $\bar{5}$)	2.62
48.5	1.88	0.10	(71 $\bar{2}$)	1.88
50.3	1.81	0.08	(322)	1.81
52.7	1.74	0.03	(12 $\bar{5}$)	1.74
57.6	1.60	0.02	(522)	1.60

3.3. X-ray Photoelectron Spectroscopy

Figure 6 shows the W 4f and O 2p spectra, the survey spectrum, and the valence band spectrum of the nanotiles. The energy distribution of W 4f core levels is presented in Figure 6a. The spectrum can be deconvoluted into two doublets, with the additional fifth component (around 41.1 eV) corresponding to the W 5p photoelectrons. The main peaks, representing 84% of total W 4f, appear at 35.5 and 37.6 eV, corresponding to 4f_{7/2} and 4f_{5/2}, respectively, of W in 6+ oxidation state [21]. The remaining 16% are attributed to a doublet positioned at 34.3 and 36.4 eV of the 4f_{7/2} and 4f_{5/2} of W in 5+ oxidation

states [22,23]. We can disregard the presence of WO_2 in the nanotiles, as there are no peaks corresponding to 4+ oxidation states (doublets at 33.3 and 35.5 eV) or metallic tungsten (31.2 and 33.4 eV) [24,25].

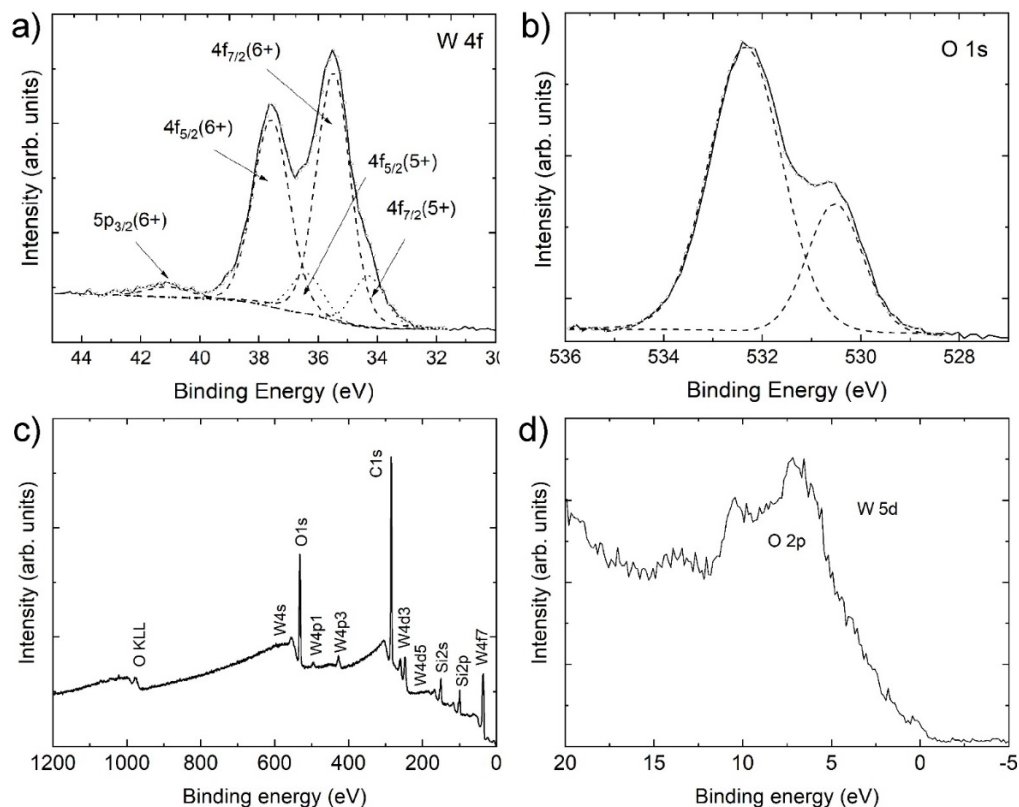


Figure 6. XPS spectra of the nanotiles: (a) the W 4f spectrum; (b) the O 1s spectrum; (c) XPS survey spectrum; and (d) the valence band spectrum.

The oxygen O 1s spectrum can be deconvoluted into two peaks, as shown in Figure 6b. Peak at 530.5 eV, attributing 26% to the O 1s photoelectrons, corresponds to O^{2-} bonded to W^{6+} in WO_3 [26]. Peak at 532.3 eV may correspond to oxygen O^{2-} bonded to SiO_2 (substrate), C-O bonds or lower oxidation states of O in W-O bonds. The survey spectrum presented in Figure 6c shows no impurities other than carbon, while the silicon peaks arise due to the SiO_2 substrate. The valence band spectrum presented in Figure 6d shows a broad O 2p peak with non-negligible density of states at the Fermi energy.

3.4. Raman Spectroscopy

Raman spectra of the nanotiles are shown in Figure 7a. The spectra were taken with the laser polarisation parallel and perpendicular to the corrugations (i.e., b axis). The peak positions and their normalized intensities are presented in Table 3. The Raman spectrum of the nanotiles with the polarisation parallel to the b axis reveals six peaks at 136.5, 322.5, 341.5, 426.5, 722, and 810 cm^{-1} . The peak at 136.5 cm^{-1} is attributed to the relative translational or rotational motions of WO_6 octahedral units in the same unit cell (lattice modes), the 322.5, 341.5, and 426.5 peaks to the W-O-W bending modes, while the 722 and 810 cm^{-1} peaks are attributed to the W-O stretching modes [7,27]. On the other hand, Raman spectrum of the nanotiles with the polarisation perpendicular to the b axis has nine peaks at 136, 180, 232.5, 271.5, 331.5, 367, 428, 702, and 810 cm^{-1} . In both cases the 810 cm^{-1} peak is the most intense one. The dependency of the Raman spectra on orientation is a direct evidence of material anisotropy. Similarly to the previously reported spectra, [20] the spectrum where the polarisation is parallel to the b axis has sharper and more pronounced peaks, pointing to a crystal structure with fewer defects and a higher

number of W-O bonds with well-defined lengths. The Raman spectrum recorded with the polarisation perpendicularly to the b axis has a greater number of peaks in the lattice ($<200\text{ cm}^{-1}$) and bending mode ($200\text{--}400\text{ cm}^{-1}$) region, while the peaks associated with W-O stretching modes ($600\text{--}900\text{ cm}^{-1}$) are broader, indicating that multiple bond lengths are present [27,28]. The spectra of the nanotiles are compared with the precursor WO_3 powder, with the most prominent peaks at 72 , 135 , 273 , 372 , 716 , and 807 cm^{-1} . These peaks match the monoclinic γ -phase with the space group P^2_1/n , and the total of 48 Raman active modes [29]. Compared with the $m\text{-WO}_3$ spectrum, the most intense peak at 810 cm^{-1} is slightly red-shifted towards longer wavelengths with regard to the 807 cm^{-1} in $m\text{-WO}_3$, indicating slightly shorter bonds [7,30]. The peaks at 702 and 428 cm^{-1} are blue-shifted, indicating slightly longer bonds (i.e., shorter wavelengths) compared to the $m\text{-WO}_3$ peaks situated at 715 cm^{-1} and 434 cm^{-1} , respectively.

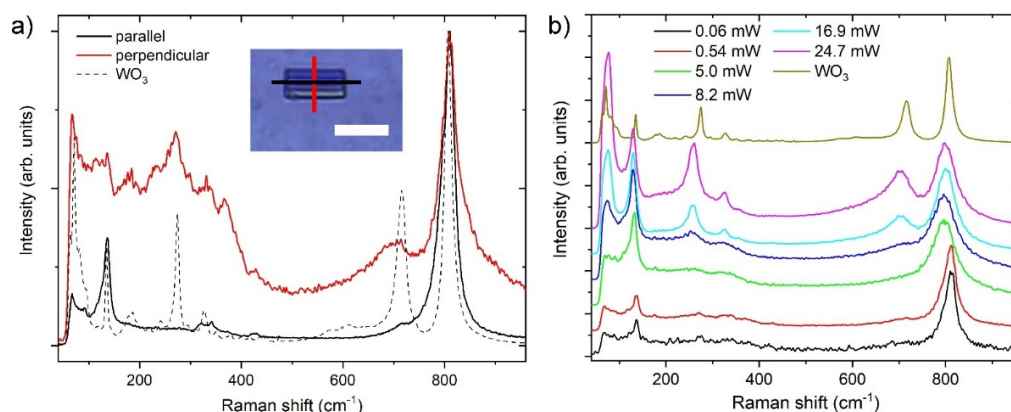


Figure 7. (a) Raman spectra of the WO_{3-x} nanotiles taken parallel and perpendicular to the corrugations, and of $m\text{-WO}_3$ (dashed line). Inset shows an optical image of the nanotile with the red and black line representing the direction of the laser polarisation. (b) Power dependency of the Raman spectra.

Table 3. Raman peak position and normalized intensity of the nanotiles and WO_3 .

Modes	Parallel		Perpendicular		WO_3 Powder	
	Raman Shift	Int	Raman Shift	Int	Raman Shift	Int
Lattice modes	136.5	0.26	71		71	0.65
			135	0.14	135	0.29
			180	0.09	186.5	0.06
			232.5	Sh	241	0.03
W-O bending	322.5	0.02	271.5	0.19	273	0.41
			331.5	0.12	327	0.07
			341.5	0.03	350	0.02
			417	0.01	417	0.01
W-O stretching	426.5	0.01	428	0.02	437	0.01
			722	sh	716	0.49
			810	1.00	807	1.00

As these materials tend to be oxidized or damaged under the laser irradiation in ambient conditions, a stepwise laser power dependency measurement was performed. The powers at which the sample underwent change and damage can be easily inferred from the spectra shown in Figure 7b. The spectra in the power range between 0.06 and 0.54 mW are indistinguishable, while at 5 mW the 810 cm^{-1} peak shifts to 798 cm^{-1} and becomes broader, the 136 cm^{-1} peak becomes more intense and shifts to 130 cm^{-1} , and the shoulders between 200 and 400 cm^{-1} become more prominent. At this point the sample remains visually undamaged, as concluded from its optical image. The power of 8.2 mW marks the start of the sample damage. This is accompanied with the peak at 130 cm^{-1} becoming the

most prominent, the appearance of a new peak at 73 cm^{-1} , and a shoulder appears around 710 cm^{-1} . At 16.9 mW , the spectrum becomes very similar to that of the WO_3 precursor, marking the complete oxidation of the nanotile due to the heating in ambient oxygen. This is evidenced by a clear appearance of the peak at 702 cm^{-1} , albeit blue-shifted and broader (716 cm^{-1} for $m\text{-WO}_3$). The two shoulders between 200 and 400 cm^{-1} transform into peaks at 258 and 325 cm^{-1} (274 and 327 cm^{-1} for $m\text{-WO}_3$). Additionally, the peak at 76 cm^{-1} becomes the most intense one. For higher laser powers, no other new peaks appear.

4. Discussion

The reported nanotiles are composed of multiple $\text{W}_n\text{O}_{3n-1}$ phases, with three of those not observed to date. As previously reported, the multiphase nature of a single nanotile could stabilize the $\text{W}_n\text{O}_{3n-1}$ phases [20]. In our previous report, the similar multi-stoichiometric platelets had a flat, corrugation-free surface, while the nanotiles have distinct corrugations with tens of nm in depth. The change in the morphology could be explained with a slightly different overall stoichiometry. Another reason for this change may be because the nanotiles did not have a template from which to grow, while the platelets grew epitaxially from a nanowire [20]. Similar corrugations are also present in other tungsten suboxides [31–33] and could contribute to the stabilization of different phases. It is presumed that the nanotiles grow faster along the [010] crystallographic axis (along the corrugations), as the length of the nanotiles varies, while the width is remaining quite uniform.

The XRD pattern of the nanotiles differs from a typical XRD pattern of the $m\text{-WO}_3$ especially in the low-angle region. Due to the P2/a symmetry of the $\text{W}_n\text{O}_{3n-1}$ stoichiometries, only $(2n,0,1)$ and $(2n,0,0)$ diffraction lines should be visible [12]. At approximately $2\theta > 30^\circ$, diffraction lines from $\text{W}_n\text{O}_{3n-1}$ and $m\text{-WO}_3$ overlap and thus cannot be used to determine the structure or the stoichiometry.

The valence band spectrum shows some density of states at the Fermi energy. The near-Fermi bands are formed due to 5d- and W 6s-like states taking part in the formation of the shortened W-W bonds [34] or due to trap states created by defects [35]. This could indicate a slightly metallic behaviour at room temperature, instead of a semiconducting one. DFT calculation on similar stoichiometries shows that the 5d-orbitals of tungsten atoms, which are part of the CS planes, are responsible for the conductivity and other effects related to the states near the Fermi surface [17,36].

The Raman spectra of the nanotiles have peaks of similar shape and position to those from the literature [20]. The spectra taken at the polarisation along the b axis have fewer peaks in the lattice and bending mode region than when the polarisation is perpendicular to the b axis. Compared to some other Raman spectra of WO_{3-x} nanomaterials [24,37,38], our spectra show narrower peaks, pointing to a higher degree of crystallinity. When the laser power is increased, the nanotiles oxidize to $m\text{-WO}_3$ [24,37].

Due to the intrinsic oxygen vacancies and formation of CS planes, the electronic and optical properties of tungsten suboxides differ from $m\text{-WO}_3$. Such properties may provide an advantage in applications such as water splitting [39], near-infrared shielding [40], in anode materials for high-performance Li-ion batteries [41], field-effect-transistors [42], photocatalysis [43], and in-domain boundary engineering [44]. As it was shown [35], sub-stoichiometric WO_{3-x} nanosheets can be used as physisorption-based NO_2 sensors. A slight difference in the stoichiometry can change the WO_{3-x} materials from a semiconductor to a metal, which can result in a poorer performance of such sensors. As pristine WO_3 does not have a high photocatalytic activity, introducing oxygen vacancies and/or using lower dimensional WO_{3-x} can improve its performance. In several studies [45,46], the WO_{3-x} materials outperformed pristine WO_3 in the degradation of dyes such as methylene blue, congo red, and rhodamine B. The oxygen vacancies act as electron donors, increasing the charge transport and thus enhancing the photocatalytic activity. Sub-stoichiometric materials also outperform $m\text{-WO}_3$ when it comes to water splitting [47]. By annealing the samples under different atmospheres, the number and nature of oxygen vacancies were

altered. It was concluded that the moderate concentration of oxygen vacancies results in appearance of W^{5+} shallow donor states that increase photoactivity, while the deep trap W^{4+} states have a detrimental effect on photocurrent. Being able to determine the stoichiometry and with it the electrical and optical properties of WO_{3-x} nanomaterials offers new opportunities for a wide range of applications.

5. Conclusions

Multi-stoichiometric nanotiles were synthesized using the CVT method. The thickness of the nanotiles ranged from a few 10 to a few 100 nm, and they grew up to a few μm in the lateral size. The formation of $\{102\}_r$ CS planes indicates, that only W_nO_{3n-1} phases grow inside the nanotiles. Three new stoichiometries were identified from HRTEM images: $W_{13}O_{38}$ ($WO_{2.923}$), $W_{12}O_{35}$ ($WO_{2.917}$), and $W_{11}O_{32}$ ($WO_{2.909}$). Measured unit cell parameters agreed well with the calculated ones. The valence band spectrum showed some density of states at the Fermi energy, making the material slightly metallic. Obtained Raman spectra showed multiple peaks and are direct evidence of the material anisotropy. Increasing the laser power during Raman spectroscopy promoted the oxidation of the platelets into m- WO_3 .

Supplementary Materials: The following are available online at <https://www.mdpi.com/article/10.3390/nano11081985/s1>, Figure S1: (a) An AFM image of a nanotile with a line profile showing its height; (b) Figure S2: TEM image along the [010] direction. The white arrows point along the CS planes. Figure S3: interatomic distance between tungsten atoms that are not part of the CS plane (red) and interatomic distance between tungsten atoms that are part of the CS plane, where the tungsten octahedra are joined by edges (green).

Author Contributions: Conceptualization, L.P. and B.V.; methodology, L.P. and B.V.; validation, L.P., B.V., J.K., S.D.Š. and M.R.; formal analysis, L.P. and B.V.; investigation, L.P., B.V., J.K. and S.D.Š.; resources, M.R.; data curation, L.P. and B.V.; writing—original draft preparation, L.P. and B.V.; writing—review and editing, J.K., S.D.Š. and M.R.; visualization, L.P. and B.V.; supervision, M.R.; project administration, M.R.; funding acquisition, M.R. All authors have read and agreed to the published version of the manuscript.

Funding: This work was supported by grants from the Slovene Research Agency P1-0099 and P2-0082.

Data Availability Statement: The data presented in this study are available on request from the corresponding author.

Acknowledgments: The authors would like to thank Janez Jelenc for all the help regarding the AFM images.

Conflicts of Interest: The authors declare that they have no conflict of interest.

References

1. Sayama, K.; Kazuaki, M.; Ryu, A.; Yoshimoto, A.; Hironori, A. Stoichiometric water splitting into H_2 and O_2 using a mixture of two different photocatalysts and an IO_3^-/I^- shuttle redox mediator under visible light irradiation. *Chem. Comm.* **2001**, *23*, 2416–2417. [[CrossRef](#)]
2. Ho, J. Novel nitrogen monoxides (NO) gas sensors integrated with tungsten trioxide (WO_3)/pin structure for room temperature operation. *Solid-State Electron.* **2003**, *47*, 827–830. [[CrossRef](#)]
3. Reyes, L.F.; Hoel, A.; Saukko, S.; Heszler, P.; Lantto, V.; Granqvist, C.G. Gas sensor response of pure and activated WO_3 nanoparticle films made by advanced reactive gas deposition. *Sens. Actuators B Chem.* **2006**, *117*, 128–134. [[CrossRef](#)]
4. Hai, Z.; Wei, Z.; Xue, C.; Xu, H.; Verpoort, F. Nanostructured tungsten oxide thin film devices: From optoelectronics and ionics to iontronics. *J. Mater. Chem.* **2019**, *7*, 12968–12990. [[CrossRef](#)]
5. Thind, S.S.; Chang, X.; Wentzell, J.S.; Chen, A. High-performance based supercapacitor on tantalum iridium oxides supported on tungsten oxide nanoplatelets. *Electrochem. Commun.* **2016**, *67*, 1–5. [[CrossRef](#)]
6. Cazzanelli, E.; Vinegoni, C.; Mariotto, G.; Kuzmin, A.; Purans, J. Low-Temperature Polymorphism in Tungsten Trioxide Powders and Its Dependence on Mechanical Treatments. *J. Solid State Chem.* **1999**, *143*, 24–32. [[CrossRef](#)]
7. Daniel, M.F.; Desbat, B.; Lassegues, J.C.; Gerand, B.; Figlarz, M. Infrared and raman study of WO_3 tungsten trioxides and $WO_3 \cdot xH_2O$ tungsten trioxide hydrates. *J. Solid State Chem.* **1987**, *67*, 235–247. [[CrossRef](#)]
8. Filipescu, M.; Ion, V.; Colceag, D.; Ossi, P.M.; Dinescu, M. Growth and characterizations of nanostructured tungsten oxides. *Rom. Rep. Phys.* **2012**, *64*, 1213–1225.

9. Salje, E. Lattice Dynamics of WO_3 . *Acta Crystallogr. Sect. A Cryst. Phys. Diffr. Theor. Gen. Crystallogr.* **1975**, *31*, 360–363. [[CrossRef](#)]
10. Li, X.L.; Liu, J.F.; Li, Y.D. Large-scale synthesis of tungsten oxide nanowires with high aspect ratio. *Inorg. Chem.* **2003**, *42*, 921–924. [[CrossRef](#)]
11. Hariharan, V.; Gnanavel, B.; Sathiyapriya, R.; Aroulmoji, V. A review on tungsten oxide (WO_3) and their derivatives for sensor applications. *Int. J. Adv. Sci. Eng* **2019**, *5*, 1163–1168. [[CrossRef](#)]
12. Magnéli, A. Structures of the ReO_3 -type with recurrent dislocations of atoms: homologous series' of molybdenum and tungsten oxides. *Acta Crystallogr.* **1953**, *6*, 495–500. [[CrossRef](#)]
13. Pickering, R.; Tilley, R.J.D. An electron microscope study of tungsten oxides in the composition range $\text{WO}_{2.90}$ – $\text{WO}_{2.72}$. *J. Solid State Chem.* **1976**, *16*, 247–255. [[CrossRef](#)]
14. Lundberg, M.; Sundberg, M.; Magnéli, A. The “Pentagonal Column” as a building unit in crystal and defect structures of some groups of transition metal compounds. *J. Solid State Chem.* **1982**, *44*, 32–40. [[CrossRef](#)]
15. Migas, D.B.; Shaposhnikov, V.L.; Rodin, V.N.; Borisenko, V.E. Tungsten oxides. I. Effects of oxygen vacancies and doping on electronic and optical properties of different phases of WO_3 . *J. Appl. Phys.* **2010**, *108*, 093713. [[CrossRef](#)]
16. Frey, G.L.; Rothschild, A.; Sloan, J.; Rosentsveig, R.; Popovitz-Biro, R.; Tenne, R. Investigations of nonstoichiometric tungsten oxide nanoparticles. *J. Solid State Chem.* **2001**, *162*, 300–314. [[CrossRef](#)]
17. Migas, D.B.; Shaposhnikov, V.L.; Borisenko, V.E. Tungsten oxides. II The metallic nature of Magnéli phases. *J. Appl. Phys.* **2010**, *108*, 093714. [[CrossRef](#)]
18. Kilaas, R. Optimal and near-optimal filters in high-resolution electron microscopy. *J. Microsc.* **1998**, *190*, 45–51. [[CrossRef](#)]
19. Bursill, L.A.; Hyde, B.G. CS Families derived from the ReO_3 structure type: An electron microscope study of reduced WO_3 and related pseudobinary systems. *J. Solid State Chem.* **1972**, *14*, 430–446. [[CrossRef](#)]
20. Pirker, L.; Višić, B.; Škapin, S.D.; Dražić, G.; Kovač, J.; Remškar, M. Multi-stoichiometric quasi-two-dimensional $\text{W}_n\text{O}_{3n-1}$ tungsten oxides. *Nanoscale* **2020**, *212*, 15102–15114. [[CrossRef](#)]
21. Leftheriotis, G.; Papaefthimiou, S.; Yianoulis, P.; Siokou, A.; Kefalas, D. Structural and electrochemical properties of opaque sol–gel deposited WO_3 layers. *Appl. Surf. Sci.* **2003**, *218*, 276–281. [[CrossRef](#)]
22. Katoh, M.; Takeda, Y. Chemical state analysis of tungsten and tungsten oxides using an electron probe microanalyzer. *Jpn. J. Appl. Phys.* **2004**, *43*, 7292. [[CrossRef](#)]
23. Zhang, C.; Boudiba, A.; Navio, C.; Bittencourt, C.; Olivier, M.G.; Snyders, R.; Debliquy, M. Highly sensitive hydrogen sensors based on co-sputtered platinum-activated tungsten oxide films. *Int. J. Hydrogen Energy* **2011**, *36*, 1107–1114. [[CrossRef](#)]
24. Lu, D.Y.; Chen, J.; Zhou, J.; Deng, S.Z.; Xu, N.S.; Xu, J.B. Raman spectroscopic study of oxidation and phase transition in $\text{W}_{18}\text{O}_{49}$ Nanowires. *J. Raman Spectrosc.* **2007**, *38*, 176–180. [[CrossRef](#)]
25. Remškar, M.; Kovac, J.; Viršek, M.; Mrak, M.; Jesih, A.; Seabaugh, A. W_5O_{14} nanowires. *Adv. Funct. Mater.* **2007**, *17*, 1974–1978. [[CrossRef](#)]
26. Trapatseli, M.; Vernardou, D.; Tzanetakis, P.; Spanakis, E. Field emission properties of low-temperature, hydrothermally grown tungsten oxide. *ACS Appl. Mater. Interfaces* **2011**, *3*, 2726–2731. [[CrossRef](#)] [[PubMed](#)]
27. Hardcastle, F.D.; Wachs, I.E. Determination of the molecular structures of tungstates by raman spectroscopy. *J. Raman Spectrosc.* **1995**, *26*, 397–405. [[CrossRef](#)]
28. Gonzalez-Calbet, J.M.; Rosique-Perez, C.; Vallet-Regi, M.; Alario-Franco, M.A.; Rodríguez-Carvajal, J. Lithium insertion in reduced tungsten oxides. *Solid State Ionics* **1989**, *32*, 162–166. [[CrossRef](#)]
29. Woodward, P.M.; Sleight, A.W.; Vogt, T. Structure refinement of triclinic tungsten trioxide. *J. Phys. Chem. Solids* **1995**, *56*, 1305–1315. [[CrossRef](#)]
30. Thummavichai, K.; Wang, N.; Xu, F.; Rance, G.; Xia, Y.; Zhu, Y. In situ investigations of the phase change behaviour of tungsten oxide nanostructures. *R. Soc. Open Sci.* **2018**, *5*, 171932. [[CrossRef](#)]
31. Saqib, M.; Jelenc, J.; Pirker, L.; Škapin, S.D.; De Pietro, L.; Ramsperger, U.; Knápek, A.; Müllerová, I.; Remškar, M. Field emission properties of single crystalline W_5O_{14} and $\text{W}_{18}\text{O}_{49}$ nanowires. *J. Electron. Spectros. Relat. Phenom.* **2020**, *241*, 146837. [[CrossRef](#)]
32. Zhang, Z.; Sheng, L.; Chen, L.; Zhang, Z.; Wang, Y. Atomic-scale observation of pressure-dependent reduction dynamics of $\text{W}_{18}\text{O}_{49}$ nanowires in an environmental TEM. *Phys. Chem. Chem. Phys.* **2017**, *19*, 16307. [[CrossRef](#)] [[PubMed](#)]
33. Merchan-Merchan, W.; Farahani, M.F.; Moorhead-Rosenberg, Z. Electron beam induced formation of tungsten sub-oxide nanorods from flame-formed fragments. *Micron* **2014**, *57*, 23–30. [[CrossRef](#)]
34. Khyzhun, O.Y. XPS, XES and XAS studies of the electronic structure of tungsten oxides. *J. Alloys Compd.* **2000**, *305*, 1–6. [[CrossRef](#)]
35. Khan, H.; Zavabeti, A.; Wang, Y.; Harrison, C.J.; Carey, B.J.; Mohiuddin, M.; Chrimes, A.F.; De Castro, I.A.; Zhang, B.Y.; Sabri, Y.M.; et al. Quasi-physisorptive two dimensional tungsten oxide nanosheets with extraordinary sensitivity and selectivity to NO_2 . *Nanoscale* **2017**, *9*, 19162–19175. [[CrossRef](#)]
36. Korshunov, M.M.; Nekrasov, I.A.; Pavlov, N.S.; Slobodchikov, A.A. Band structure of tungsten oxide $\text{W}_{20}\text{O}_{58}$ with ideal octahedra. *JETP Lett.* **2021**, *113*, 57–60. [[CrossRef](#)]
37. Chen, J.; Lu, D.; Zhang, W.; Xie, F.; Zhou, J.; Gong, L.; Liu, X.; Deng, S.; Xu, N. Synthesis and raman spectroscopic study of $\text{W}_{20}\text{O}_{58}$ nanowires. *J. Phys. D* **2008**, *41*, 115305. [[CrossRef](#)]
38. Huang, P.; Kalyar, M.M.A.; Webster, R.F.; Cherns, D.; Ashfold, M.N.R. Tungsten oxide nanorod growth by pulsed laser deposition: Influence of substrate and process conditions. *Nanoscale* **2014**, *6*, 13586–13597. [[CrossRef](#)] [[PubMed](#)]

39. Lee, Y.-J.; Lee, T.; Soon, A. Phase stability diagrams of group 6 Magnéli oxides and their implications for photon-assisted applications. *Chem. Mater.* **2019**, *31*, 4282–4290. [[CrossRef](#)]
40. Zhao, Z.; Bai, Y.; Ning, W.; Fan, J.; Gu, Z.; Chang, H.; Yin, S. Effect of surfactants on the performance of 3D morphology $W_{18}O_{49}$ by solvothermal synthesis. *Appl. Surf. Sci.* **2019**, *471*, 537–544. [[CrossRef](#)]
41. Li, Y.; Chang, K.; Tang, H.; Li, B.; Qin, Y.; Hou, Y.; Chang, Z. Preparation of oxygen-deficient WO_{3-x} nanosheets and their characterization as anode materials for high-performance Li-ion batteries. *Electrochim. Acta* **2019**, *298*, 640–649. [[CrossRef](#)]
42. Zhuiykov, S. Material characterisation and transistor function of quasi two dimensional sub-stoichiometric WO_{3-x} nanoflakes. *Mater. Lett.* **2016**, *165*, 173–177. [[CrossRef](#)]
43. Pan, K.; Shan, K.; Wei, S.; Li, K.; Zhu, J.; Siyal, S.H.; Wu, H.-H. Enhanced photocatalytic performance of WO_{3-x} with oxygen vacancies via heterostructuring. *Compos. Commun.* **2019**, *16*, 106–110. [[CrossRef](#)]
44. Salje, E.K.H. Polaronic states and superconductivity in WO_{3-x} . *Condens. Matter* **2020**, *5*, 32. [[CrossRef](#)]
45. Chen, S.; Xiao, Y.; Xie, W.; Wang, Y.; Hu, Z.; Zhang, W.; Zhao, H. Facile strategy for synthesizing non-stoichiometric monoclinic structured tungsten trioxide (WO_{3-x}) with plasma resonance absorption and enhanced photocatalytic activity. *Nanomaterials* **2018**, *8*, 553. [[CrossRef](#)] [[PubMed](#)]
46. Parthibavarman, M.; Karthik, M.; Prabhakaran, S. Facile and one step synthesis of WO_3 nanorods and nanosheets as an efficient photocatalyst and humidity sensing material. *Vacuum* **2018**, *155*, 224–232. [[CrossRef](#)]
47. Mohamed, A.M.; Amer, A.W.; AlQaradawi, S.Y.; Allam, N.K. On the nature of defect states in tungstate nanoflake arrays as promising photoanodes in solar fuel cells. *Phys. Chem. Chem. Phys.* **2016**, *18*, 22217–22223. [[CrossRef](#)] [[PubMed](#)]

PAPER • OPEN ACCESS

Influence of crystal structure and oxygen vacancies on optical properties of nanostructured multi-stoichiometric tungsten suboxides

To cite this article: Bojana Višić *et al* 2022 *Nanotechnology* **33** 275705

View the [article online](#) for updates and enhancements.

You may also like

- [A Solar Coronal Hole and Fast Solar Wind Turbulence Model and First-orbit Parker Solar Probe \(PSP\) Observations](#)
L. Adhikari, G. P. Zank and L.-L. Zhao
- [Oxide-Thickness-Dependent Suboxide Width and Its Effect on Inversion Tunneling Current](#)
Yen-Po Lin and Jenn-Gwo Hwu
- [Low-dimensional phases engineering for improving the emission efficiency and stability of quasi-2D perovskite films](#)
Yue Wang, , Zhuang-Zhuang Ma *et al.*







EDINBURGH INSTRUMENTS

WORLD LEADING MOLECULAR SPECTROSCOPY SOLUTIONS

edinst.com

The advertisement features a red background with the Edinburgh Instruments logo on the left, which consists of a stylized sunburst pattern. In the center, several pieces of laboratory equipment are displayed, including a large white and black instrument labeled 'FLS 1000' and a smaller white instrument labeled 'F55'. The text 'WORLD LEADING MOLECULAR SPECTROSCOPY SOLUTIONS' is written in white, bold, uppercase letters. The website 'edinst.com' is shown in a white box in the bottom right corner.

Influence of crystal structure and oxygen vacancies on optical properties of nanostructured multi-stoichiometric tungsten suboxides

Bojana Višić^{1,2,5} , Luka Pirker^{1,5} , Marko Opačić², Ana Milosavljević², Nenad Lazarević², Boris Majaron^{3,4}  and Maja Remškar¹ 

¹ Department of Condensed Matter Physics, Jozef Stefan Institute, Jamova Cesta 39, 1000 Ljubljana, Slovenia

² Institute of Physics Belgrade, University of Belgrade, Pregrevica 118, 11080 Belgrade, Serbia

³ Department of Complex Matter, Jozef Stefan Institute, Jamova 39, 1000 Ljubljana, Slovenia

⁴ Faculty of Physics and Mathematics, University of Ljubljana, Jadranska 19, Slovenia

E-mail: bojana.visic@ipb.ac.rs

Received 8 March 2022, revised 28 March 2022

Accepted for publication 31 March 2022

Published 20 April 2022



CrossMark

Abstract

Four distinct tungsten suboxide (WO_{3-x}) nanomaterials were synthesized via chemical vapour transport reaction and the role of their crystal structures on the optical properties was studied. These materials grow either as thin, quasi-2D crystals with the $\text{W}_n\text{O}_{3n-1}$ formula (in shape of platelets or nanotiles), or as nanowires (W_5O_{14} , $\text{W}_{18}\text{O}_{49}$). For the quasi-2D materials, the appearance of defect states gives rise to two indirect absorption edges. One is assigned to the regular bandgap occurring between the valence and the conduction band, while the second is a defect-induced band. While the bandgap values of platelets and nanotiles are in the upper range of the reported values for the suboxides, the nanowires' bandgaps are lower due to the higher number of free charge carriers. Both types of nanowires sustain localized surface plasmon resonances, as evidenced from the extinction measurements, whereas the quasi-2D materials exhibit excitonic transitions. All four materials have photoluminescence emission peaks in the UV region. The interplay of the crystal structure, oxygen vacancies and shape can result in changes in optical behaviour, and the understanding of these effects could enable intentional tuning of selected properties.

Supplementary material for this article is available [online](#)

Keywords: tungsten oxides, Magnèli phases, nanowires, quasi-2D materials

(Some figures may appear in colour only in the online journal)

⁵ These authors contributed equally.



Original content from this work may be used under the terms of the [Creative Commons Attribution 4.0 licence](#). Any further distribution of this work must maintain attribution to the author(s) and the title of the work, journal citation and DOI.

1. Introduction

The family of tungsten oxides, including stoichiometric WO_3 and WO_2 and substoichiometric Magnèli phases (WO_{3-x} , $0 < x < 1$), is widely studied due to numerous intriguing properties [1–5]. These tungsten (sub)oxides have been used as photodetectors [6, 7] and gas sensors [8–10], in photocatalysis and photoelectrochemical water splitting [3, 11, 12],

in smart windows [13] and optoelectronics [14]. In bulk form, WO_3 is a large indirect bandgap n-type semiconductor, with bandgap values reported in the 2.6–3.0 eV range [15–17]. In nanosized WO_3 , quantum size effects appear, resulting in a blueshift of the bandgap up to 3.25 eV, with the bandwidth modulation correlated to the size of the nanoparticles [18]. This is a direct consequence of the quantum confinement effect.

Due to the crystal shear mechanism, various sub-stoichiometric Magnèli phases with different combinations of edge- or corner-sharing WO_6 octahedra can be formed [19]. This may lead to appearance of crystal shear (CS) planes and pentagonal columns (PC), which form to accommodate oxygen vacancies [20, 21]. For less reduced suboxides (i.e. $x < 0.2$), CS planes occur; while PCs are formed for x greater than 0.2. In the former, CS planes' corner-sharing WO_6 octahedra become edge-sharing [22], while in the latter WO_7 bipyramids are formed and share their equatorial edges with the WO_6 octahedra [23]. The degree of reduction and appearance of oxygen vacancies can be crucial for understanding the change of the optical response with respect to the fully oxidized WO_3 [8]. Furthermore, it was reported that the oxygen vacancy defect states induced by annealing can significantly improve electrical conductivity [24]. Substoichiometric WO_{3-x} are mostly found to be blue or light green, which is a structure-sensitive phenomenon and is mainly a consequence of the stoichiometry or oxygen vacancies [25, 26]. First-principles pseudopotential and total-energy projector-augmented wave method calculations showed that single oxygen vacancies and substoichiometric crystal structures modify the optical properties and generate different types of defect states in the bulk [27, 28].

For nanostructured WO_{3-x} , various phenomena may lead to different size- and shape- dependent behaviour within the same stoichiometry. This can lead to seemingly contradictory results, if only the effect of the degree of reduction is considered. It was reported that the metallic $\text{WO}_{2.83}$ nanorods ($\text{W}_{24}\text{O}_{68}$) can sustain strong localized surface plasmon resonances (LSPR), centred around 1.4 eV (corresponding to $\lambda = 900$ nm) [26]. Electrical transport measurements of $\text{WO}_{2.8}$ (W_5O_{14}) show that they exhibit metallic behaviour [29]. On the other hand, based on electrical transport measurements and photoluminescence spectra, $\text{WO}_{2.72}$ ($\text{W}_{18}\text{O}_{49}$) nanowires (NWs) show a semiconducting behaviour [30, 31].

A close relationship between the creation of oxygen vacancies and stoichiometry (i.e. degree of reduction) and morphology has been reported [32–34]. Both the stoichiometry and the amount of oxygen vacancies heavily depend on the synthesis conditions, and in turn determine the optical and electrical properties, such as photoluminescence and electrical conductivity. Therefore, a careful structural study of these materials is significant for interpreting optical spectra. In this paper, we report on optical properties of various nanostructured suboxides; namely, multistoichiometric $\text{W}_n\text{O}_{3n-1}$ in two distinct morphologies (platelets and nanotiles), and W_5O_{14} ($\text{WO}_{2.8}$) and $\text{W}_{18}\text{O}_{49}$ ($\text{WO}_{2.72}$) nanowires.

2. Methods

2.1. Synthesis

All the materials were synthesized via chemical vapour transport reaction in a two-zone furnace, using iodine as the transport agent. The synthesis protocols are described in detail in [29, 35–37].

2.2. Electron microscopy

Scanning electron microscopy (SEM) was performed on Supra 35 VP (Carl Zeiss, Germany). High-resolution transmission electron microscopy (HRTEM) and electron diffraction (ED) images were obtained by a Cs probe-corrected TEM/STEM JEOL ARM 200CF microscope equipped with a cold-FEG electron source, operating at 200 kV. Cross-sections of the samples for TEM analysis were obtained using a Helios NanoLab 650 Focused Ion Beam-scanning electron microscope (FIB).

2.3. Photoluminescence

The solutions for the optical measurements were prepared using purified water (extinction) or ethanol (photoluminescence and Raman spectroscopy).

Photoluminescence spectra were measured using an optical spectrometer (PTI QuantaMaster 8000 by Horiba) with a continuous Xe lamp and a photomultiplier sensitive in visible and near-infrared part of the spectrum (Hamamatsu R2658). Holographic reflection gratings blazed at 300 nm were used in the dual-stage excitation monochromator, and ruled gratings (500 nm blaze) in the single-stage emission monochromator. The spectra were measured in the wavelength range of 290–450 nm (corresponding to 3.1–4.3 eV) at nominal resolution of 3 nm, with the excitation spectral band centered at 275 nm (4.51 eV). All presented spectra were corrected for spectral dependence of the instrument's excitation and emission channels.

2.4. Extinction measurements

Extinction measurements were performed with an UV–vis spectrometer (Perkin-Elmer lambda 950). The spectra were recorded with a 1 nm resolution. The solution was hand-shaken and the suspensions were measured using quartz cuvettes.

2.5. Raman scattering

The Raman scattering measurements were performed using a Tri Vista 557 Raman system in backscattering micro-Raman configuration. The 532 nm line of VerdiG solid-state (for platelets) and the 514.5 nm line of Ar^+/Kr^+ ion gas laser (for nanotiles and nanowires) were used as an excitation source. A microscope objective with $\times 100$ magnification was used for focusing the laser beam and collecting scattered light. Laser power was kept below 0.5 mW at the sample surface, in order to minimize local heating. Spectra were recorded in parallel and crossed polarisation configuration. All measurements were performed in air, at room temperature. Spectra were corrected for the Bose factor.

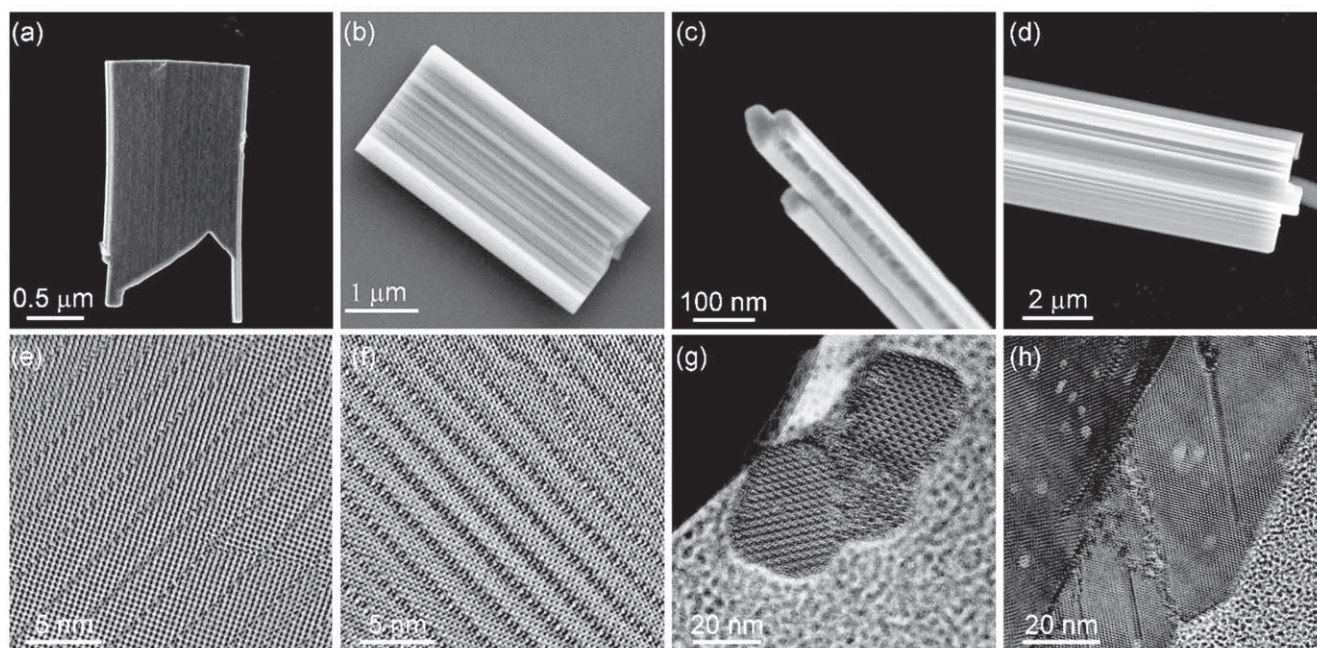


Figure 1. Electron microscopy images of (a), (e) platelets, (b), (f) nanotiles, (c), (g) W_5O_{14} NW and (d), (h) $W_{18}O_{49}$ NW. Top panel corresponds to SEM, while the bottom panel corresponds to TEM images.

Table 1. Stoichiometry of tungsten suboxide nanomaterials, their shape, thickness and lateral size (for 2D W_nO_{3n-1}) or *-diameter and length (for nanowires), and the assessed work function.

Stoichiometry	Shape	Thickness/diameter*	Lateral size/length*	Work function (eV)
W_nO_{3n-1}	Platelets	100 nm	Up to 4 μm	4.18–4.31
W_nO_{3n-1}	Nanotiles	100 nm	Up to several μm	4.94–5.30
W_5O_{14} ($WO_{2.8}$)	Nanowires	100–200 nm	Several tens μm	4.20–4.34
$W_{18}O_{49}$ ($WO_{2.72}$)	Nanowires	Up to 3 μm	Several tens μm	4.55–4.57

2.6. Kelvin probe force microscopy

The work function (WF) was measured with the Kelvin probe force microscopy (KPFM) method using a non-contact frequency-modulated atomic force microscope (NC-AFM, Omicron VT-AFM, Taunusstein, Germany) operating in ultra-high vacuum (10^{-9} mbar). The samples were dispersed in isopropanol and drop casted on a freshly cleaved highly oriented pyrolytic graphite (HOPG) substrate. The AFM and the KPFM images were taken simultaneously on the same area. KPFM was used to determine the WF of the samples by measuring the contact potential difference (CPD) between the substrate (HOPG) and the samples. As HOPG has a fairly stable WF value of 4.60 eV [38], it is commonly used as a reference material in KPFM measurements.

3. Results and discussion

3.1. Composition and morphology

The studied WO_{3-x} phases grow as thin plate-like crystals (platelets, nanotiles) or as nanowires (W_5O_{14} , $W_{18}O_{49}$). Figure 1 shows SEM and TEM images of the W_nO_{3n-1}

platelets (a), (e) and nanotiles (b), (f); W_5O_{14} nanowires (c), (g), and $W_{18}O_{49}$ nanowires (d), (h). The stoichiometry and size of all four studied WO_{3-x} phases is summarized in table 1.

The W_nO_{3n-1} platelets grow epitaxially from $W_{19}O_{55}$ nanowires. These nanowires can either get detached from the platelets by mild sonication, or remain at the long edge of the platelet, as seen in figure 1(a). The platelets grow in a rectangular geometry and are approximately 100 nm thick with the lateral size of up to 4 μm . Several W_nO_{3n-1} Magnèli phases, such as $W_{18}O_{53}$ ($WO_{2.944}$), $W_{17}O_{50}$ ($WO_{2.941}$), $W_{16}O_{47}$ ($WO_{2.938}$), $W_{15}O_{44}$ ($WO_{2.933}$), $W_{14}O_{41}$ ($WO_{2.929}$), W_9O_{26} ($WO_{2.889}$) and $W_{10}O_{29}$ ($WO_{2.9}$), were found within a single platelet [36].

The nanotiles with the length and width up to a few μm are approximately 100 nm thick. They have characteristic surface corrugations that can be several tens of nm deep. They are multi-stoichiometric, with six distinct stoichiometries within a single nanotile: $W_{16}O_{47}$ ($WO_{2.938}$), $W_{15}O_{44}$ ($WO_{2.933}$), $W_{14}O_{41}$ ($WO_{2.928}$), $W_{13}O_{38}$ ($WO_{2.923}$), $W_{12}O_{35}$ ($WO_{2.917}$), and $W_{11}O_{32}$ ($WO_{2.909}$), all having the same W_nO_{3n-1} formula [37]. In both plate-like morphologies (i.e. nanotiles and platelets), CS planes are observed, as shown in

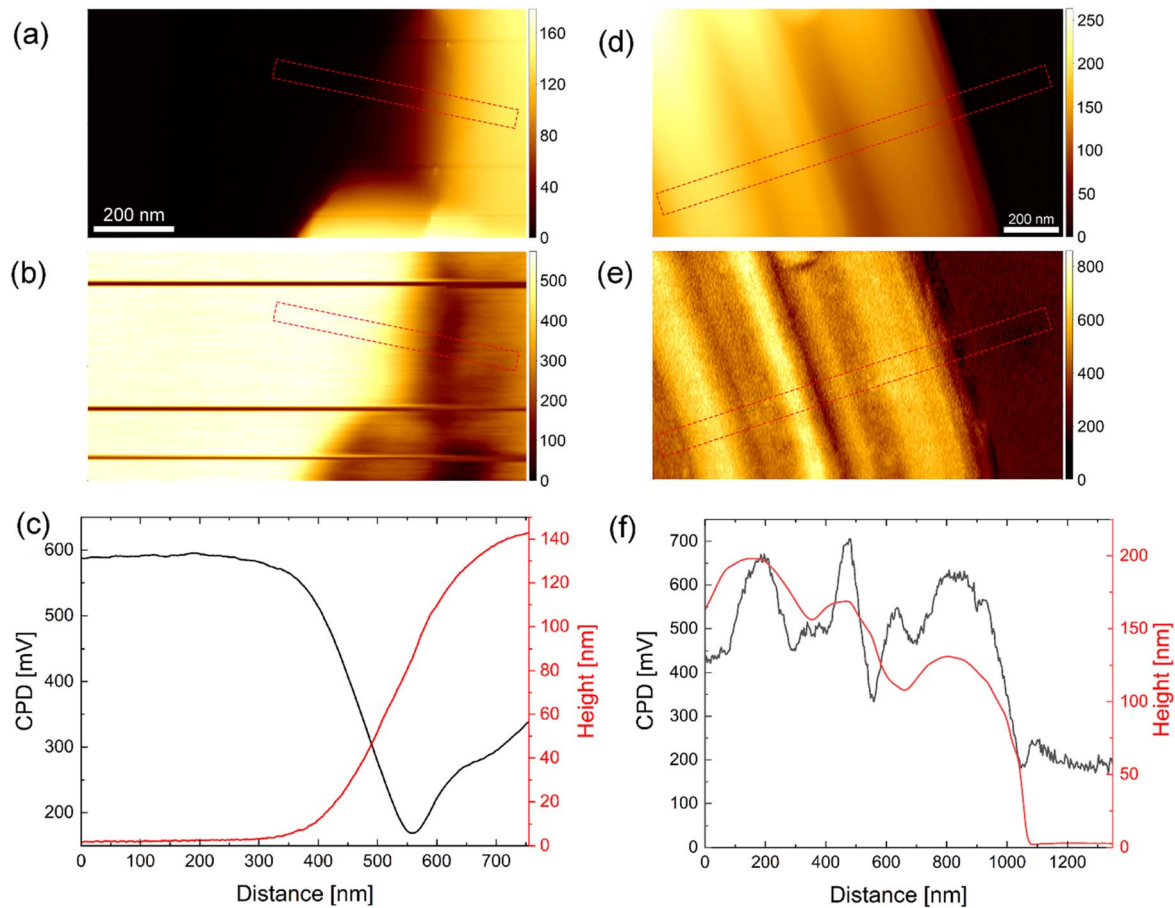


Figure 2. AFM (a), (d) and KPFM images (b), (e) of platelets and nanotiles, respectively. The CPD profiles and the matching thickness (c), (f) correspond to the areas marked with dashed rectangles.

figures 1(e), (f). The distance between the CS planes reflects the stoichiometry of a particular block.

Both W_5O_{14} and $W_{18}O_{49}$ nanowires have constant diameters along the lengths of several tens of μm . The W_5O_{14} NWs are thinner, with the mean diameter of 100–200 nm, while $W_{18}O_{49}$ NWs have significantly larger diameters of up to 3 μm , with rarely observed thin ones [35]. The cross-sectional views of such nanowires (figures 1(g), (h)) reveal that they are composed of several single-crystalline units.

3.2. Work function

The WF was measured on an individual WO_{3-x} nanotile or platelet. The results are compared with the previously published data obtained on the W_5O_{14} and $W_{18}O_{49}$ nanowires [35]. The topography and Kelvin images are shown in figure 2.

The platelet shown in figure 2(a) is around 140 nm thick. The CPD measured on the platelets was between 290 and 420 mV lower than on HOPG, corresponding to a WF of 4.18–4.31 eV. Very similar WF values were reported earlier for W_5O_{14} nanowires (4.20–4.34 eV) [35]. On the other hand, the CPD obtained on the nanotiles was between 340 and 700 mV higher than on HOPG, indicating a WF of 4.94–5.30 eV. The WF of the nanotiles is thus substantially

higher compared to both W_5O_{14} and $W_{18}O_{49}$ nanowires (4.55–4.57 eV) [35].

The KPFM and AFM images also reveal that the WF is morphology dependent. In the case of platelets, the WF is slightly lower at the edge (figure 2(c)), similar to measurements performed on the edges of W_5O_{14} nanowires [35]. This might be due to the growth mechanism, as the platelets grow from nanowires [36], or due to band bending [39]. The WF of nanotiles also varies with location and was found to be lower inside the corrugations (figure 2(f)). The difference between the CPD at top and the bottom of the corrugation can be up to 350 meV. The summarized positions of WF values are presented in table 2.

3.3. Optical properties

3.3.1. Raman spectroscopy. Raman spectra of WO_{3-x} nanomaterials can be tentatively divided into three regions, characterized by the peaks originating from different types of vibrations. Lattice modes generally appear below 200 cm^{-1} , W–O–W bending modes between approximately 200 and 400 cm^{-1} , whereas between 600 and 900 cm^{-1} one can observe W–O stretching modes [40, 41]. Figure 3 represents room temperature Raman spectra of WO_{3-x} nanostructures measured in three polarization

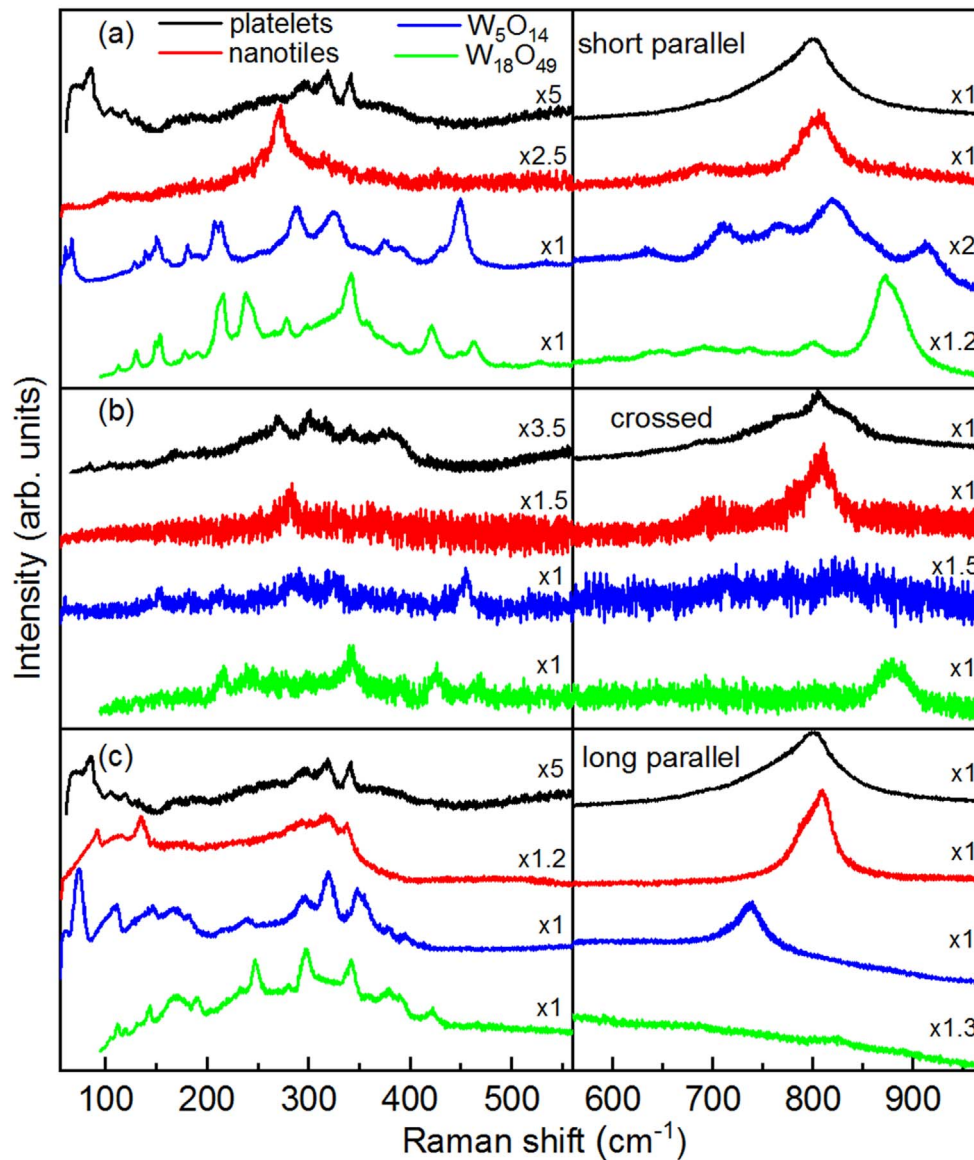


Figure 3. Raman scattering spectra of WO_{3-x} nanostructures measured at room temperature in three polarization configurations: (a) parallel, with incident and scattered light polarized along the short axis of the samples (short parallel configuration), (b) crossed, and (c) parallel, with incident and scattered light polarized along the long axis of the samples (long parallel configuration). For clarity, lower and higher-energy ranges are displayed with different scale factors.

Table 2. Summary of the assessed absorption and PL transitions, bandgap and work function values in tungsten suboxide nanomaterials.

	$\text{W}_n\text{O}_{3n-1}$ platelets	$\text{W}_n\text{O}_{3n-1}$ nanotiles	W_5O_{14} ($\text{WO}_{2.8}$)	$\text{W}_{18}\text{O}_{49}$ ($\text{WO}_{2.72}$)
UV-vis (nm)	207, 222, 241, 281, 323	205, 216, 240, 281, 324, 416	200, 223, 258, 326, 760	198, 208, 296, 776
PL (nm)	299, 323	302, 316	298, 324	299, 319
Bandgap (direct) (eV (nm))	4.11 (301)	4.05 (306)		
Bandgap (indirect) (eV (nm))	3.76 (330), 3.17 (391)	3.48 (356), 2.78 (446)	2.16 (574)	2.62 (473)
WF (eV)	4.18–4.31	4.94–5.30	4.20–4.34	4.55–4.57
Average WF (eV)	4.25	5.12	4.27	4.56

configurations: short and long parallel, with incident and scattered light polarized along short and long axis of the sample respectively; and crossed, with polarisations parallel

to the short and long axis of the sample but mutually orthogonal. In the case of the platelets, short and long parallel configurations are equivalent due to their symmetry.

Therefore, only two spectra were sufficient to observe all prominent modes noted in [36].

In platelets' crossed polarization configuration spectrum, there are four weak peaks, at 85, 105, 130 and 165 cm^{-1} related to lattice vibration, six peaks centred at 235, 271, 300, 319, 340 and 380 cm^{-1} , originating from W–O–W bending vibrations and one weak (690 cm^{-1}) and two strong (778 and 808 cm^{-1}) W–O stretching vibrations. In parallel configuration, one can observe few relatively weak peaks, at 85, 105, 120, 130, 297, 319 and 340 cm^{-1} , and two sharp overlapped peaks at 778 and 802 cm^{-1} . These results are in very good agreement with those from [36].

In the case of the nanotiles' short parallel polarization spectrum, only one weak peak (105 cm^{-1}) originating from lattice vibration, one strong peak at 271 cm^{-1} , a few weak peaks (at 231, 317, 331, 365 and 428 cm^{-1}) in the W–O–W bending region, and two prominent W–O stretching vibrations centred at 697 and 807 cm^{-1} are observed. In the crossed scattering configuration one can recognize the three highest intensity modes from that were also observed in the short parallel polarization (at 271, 697 and 807 cm^{-1}), whereas spectrum in long parallel polarization contains sharper and more pronounced low energy peaks, indicating good crystallinity and well-defined W–O bond length. Closer inspection revealed eight peaks, at 92, 113, 135, 175, 294, 319, 338 and 807 cm^{-1} , with the two prominent ones at 135 and 807 cm^{-1} , coinciding with the results given in [37].

Raman spectra of nanowires are qualitatively different from those of quasi-2D materials. Namely, for W_5O_{14} NW, in short parallel polarization seven lattice (at 67, 129, 139, 151, 181, 208 and 214 cm^{-1}), six W–O–W bending (at 288, 325, 376, 391, 430 and 448 cm^{-1}) and five W–O stretching vibrations, centred around 635, 712, 767, 819 and 912 cm^{-1} , were observed. Crossed polarization revealed Raman peaks at 151, 181, 208, 288, 325, 448 and 712 cm^{-1} , whereas in long parallel polarization one can observe peaks at 73, 108, 147, 167, 181, 237, 297, 319, 350, 376, 394 and 737 cm^{-1} .

In the short parallel polarization, the $\text{W}_{18}\text{O}_{49}$ NW spectrum hosts a large number of peaks, at 113, 129, 149, 153, 178, 190, 211, 215, 238, 245, 278, 341, 358, 390, 422, 449, 463, 527, 644, 689, 737, 801, 871 and 882 cm^{-1} , some of which are overlapping. In crossed polarization configuration there are only a few peaks, centred at 211, 215, 238, 245, 341, 422, 463, 871 and 882 cm^{-1} , whereas the spectrum in the long parallel polarization contains modes at 113, 119, 131, 142, 168, 190, 232, 247, 280, 297, 341, 378, 390, 422 and 821 cm^{-1} . The peak positions of all four materials are summarized in tables S1–4 (available online at stacks.iop.org/NANO/33/275705/mmedia).

Unlike the spectra of the nanotiles and platelets, where the W–O stretching modes centred around 800 cm^{-1} are absolutely dominant, Raman spectra of the nanowires contain a large number of sharp peaks in the first two frequency regions, which are comparable or even more dominant than the ones from the stretching vibrations region. This indicates that 2D materials contain a higher number of W–O bonds with well-defined lengths, whereas W_5O_{14} and $\text{W}_{18}\text{O}_{49}$ nanowires have better crystallinity and higher number of

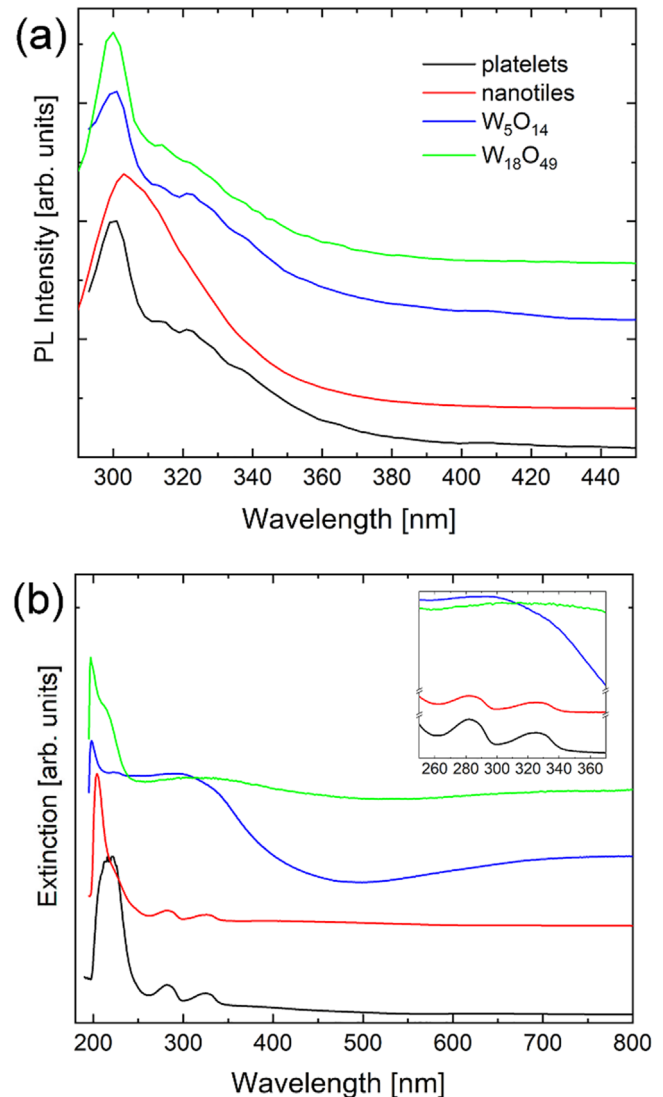


Figure 4. (a) Room temperature PL spectra and (b) UV-vis extinction spectra of platelets, nanotiles, W_5O_{14} and $\text{W}_{18}\text{O}_{49}$ nanowires.

W–O–W bonds with well-defined bond angles. The fact that spectra of all the analysed materials strongly depend on the sample orientation and light polarization unequivocally confirms their anisotropic structure.

3.3.2. Photoluminescence. In figure 4(a), the PL spectra of all four materials are presented, measured with the excitation centred at 275 nm (4.51 eV). The PL spectra were deconvoluted, confirming that they contain two distinct emission lines in the UV region (figure S1). All of these suboxides have a dominant, high-energy peak situated around 300 nm (4.1 eV). An additional, red-shifted component appears in the 320 nm region (~ 3.9 eV), but its contribution varies. The positions of the PL peaks are summarized in table 2.

Because bulk WO_3 is an indirect band-gap semiconductor, its photoluminescence (PL) spectrum does not have any prominent features. In contrast, the appearance of new states in WO_{3-x} materials allows distinct optical transitions, often

associated with PL emission lines. Many studies were reported on PL activity of the substoichiometric oxides [42–49], and, in general, correlated the electronic transitions to the defect states within the band gap, arising from oxygen vacancies. The two processes guiding these transitions were assigned either to the occurrence of localized states in the bandgap, stemming from oxygen vacancies or other defects; or to a band-to-band transition, arising from the electron–hole recombination induced by quantum confinement. However, there is no general consensus on interpretation of the observed emissions, as the experimental reports differ and do not unambiguously assign the observed emissions to the proposed mechanisms.

Theoretical models show that an oxygen vacancy can be in three new states, namely in a neutral (V_O^0), single- (V_O^+), or double-charged (V_O^{2+}) [25, 27, 34]. Within these models, the removal of an O atom from WO_3 structure (ReO_3 -type, $W^{6+}-O^{2-}-W^{6+}$) results in creation of a V_O^0 state. This corresponds to creation of either a $W^{6+} + W^{4+}$ or $2W^{5+}$ defect states with levels inside or near the valence band ($W^{4+}-V_O^0-W^{6+}$ or $W^{5+}-V_O^0-W^{5+}$) [25]. Removal of one additional electron, (i.e. conversion to V_O^+ (W^{5+})), leads to Coulombic repulsion between the positive vacancy and the nearest W-ion, displacing the ion and shifting the defect level into the bandgap ($W^{5+}-V_O^+-W^{6+}$). Removal of another electron creates a new state within the CB ($W^{6+}-V_O^{2+}-W^{6+}$). Therefore, the neutral state lies inside the valence band (VB), single-charged in the band gap, and the double-charged state inside the conduction band (CB). In other words, the W^{5+} states are shallow and can act as donor states, while electrons trapped in deeper states (W^{4+}) would need more energy to get excited into the CB. It is also important to note that the bandgap is closely related to the W–O bond length. When an O vacancy is introduced, structural relaxation of the lattice leads to an increase of the W–W distance. As the W ion gets displaced from the center of the WO_6 octahedron, the VB lowers and the CB rises, thus increasing the bandgap [50].

For PL spectra reported for $W_{18}O_{49}$ nanowires and nanorods, peaks appear in UV and blue spectral regions [31, 43, 45, 51]. For the nanorods, the peak located in the UV region blueshifts from 350 to 320 nm as the nanorod diameter decreases. This effect is assigned to quantum confinement, since the stoichiometry remains the same. The blue peak is situated around the absorption edge at 430 nm and does not show any size dependence, therefore it was assigned to the defect states within the bandgap [31].

Previously reported XPS measurements on these materials can provide more insight into origin of the transitions [29, 36, 37]. The valence band spectrum of the platelets indicates a semiconducting behaviour with a negligible density of states at the Fermi energy. On the other hand, the valence band spectrum of the nanotiles revealed a slightly metallic behaviour at room temperature due to a partial overlapping of a broad O 2p peak with W 5d orbitals [36, 37]. The W spectra confirm the presence of 5+ and 6+ oxidation states in both nanotiles and platelets. For the nanotiles, 6+ states represent 84% of the total W 4f, with the remaining 16% assigned to 5+, giving the average oxidation number of

5.84 and 3 – x value of 2.92. Similarly, the platelets spectrum is comprised of 81% of 6+ and 19% of 5+, with the oxidation number of 5.81 and 3 – x value of 2.91. These values are in great agreement with the stoichiometry deduced from the composition [36, 37]. Since the XPS measurements mainly correspond to the surface layers, these results confirm that the samples have no surface contaminations and that the additional defects do not accumulate at the surface layers. Similarly, 5+ and 6+ states have been observed for W_5O_{14} NW [29], while for the $W_{18}O_{49}$ NW, an additional 4+ state can appear [52, 53].

Focusing on the O 1s spectrum of nanotiles, platelets and W_5O_{14} NW, it can be observed that the peak at 533.5 eV is the most prominent for the platelets, the intensity decreases for NW while it is completely absent for the nanotiles. The WF values were increasing in the same order. This peak, together with the one at 532.0 eV, is attributed to O binding with W in lower oxidation states. HRTEM images shown in figure S3 reveal that the CS planes in the platelets appear parallel to the basal plane, which is still within the depth sensitivity of the XPS. On the other hand, the CS planes in the nanotiles are not close to the surface and are terminated in an unordered fashion, with the regular WO_3 dominating the surface. The effect of the oxidation state of the surface W can be of a great influence on the optical properties of these materials. Therefore, we can attribute the two observed emission bands in the UV to two electron–hole recombination processes, whereby the hole comes from the VB, while the electrons come from two resonant states within the CB, i.e. from two V_O^{2+} states [25, 48].

3.3.3. Extinction. As previously mentioned, both theoretical and experimental studies correlated oxygen vacancies and/or substoichiometric crystal structure to the appearance of defect states [27, 54, 55]. It was reported that up to $x = 0.1$, the optical and electrical properties of bulk WO_{3-x} are governed primarily by localized electrons involved in polarons [26]. The insulator-metal transition begins at $x = 0.1$, as the polaron wave functions start to overlap and form delocalized states [56]. As the x increases, free electrons start to dominate optical processes. In general, the indirect bandgap corresponds to the electronic transition from the filled O 2p orbitals at the top of the valence band to the empty W 5d orbitals in the conduction band [57]. Therefore, the absorption spectrum of WO_3 is essentially featureless until the photon energy reaches the bandgap value. Near the UV region, interband transitions start to take place and govern the optical properties [57].

Extinction (UV–vis) measurements, which include contributions of both absorbance and scattering processes, were performed on all four materials and the spectra are presented in figure 4(b). Although the samples were diluted in order to avoid the multi-scattering regime, the scattering effects in the near UV region cannot be completely excluded. The deconvolution of all the spectra has been performed and the positions of the individual peak contributions extracted, as shown in figure S2.

The most prominent transitions appear in the UVC range, with two contributions centred at 207 and 222 nm for the platelets and at 205 and 216 nm for the nanotiles, with another peak situated at 240 nm for both. Additionally, there are two prominent and closely positioned peaks, situated at 281 and 324 nm. These peaks may originate from excitonic transitions, as described later. A wide and less intense peak is also observed at 359 nm and 416 nm for the platelets and nanotiles, respectively. For both materials, the scattering is accounted for with a model function, as described in the SI.

On the other hand, the spectra of nanowires are significantly different compared to the quasi-2D materials. Both types of NWs have a high-energy peak around 200 nm. For $W_{18}O_{49}$ NWs, this peak can be deconvoluted into two peaks positioned at 198 and 208 nm. $W_{18}O_{49}$ NWs spectrum has a higher-energy peak centred at 296 nm, ending with a broad transition at 776 nm. In addition to the peak at 200 nm, W_5O_{14} NWs have a very weak peak at 223 nm and an additional broad peak at approximately 300 nm, which can be deconvoluted into two peaks situated at 258 and 326 nm. An even broader peak appears at 760 nm in the near-IR part of the spectrum. The emergence of the near-IR peaks can be associated with LSPR due to free charge carriers. LSPR were observed previously in $W_{24}O_{68}$ ($WO_{2.83}$) and $W_{19}O_{55}$ ($WO_{2.89}$) nanorods, positioned at 900 nm and 600 nm, respectively [26, 55]. Assigning the near-IR tails to LSPR is also in agreement with earlier measurements on these NWs, which suggested metallic behaviour [29, 35].

Extinction spectra of these suboxides vary substantially in the literature, even within the same stoichiometry or morphology. For example, ultrathin (sub-nanometre) $W_{18}O_{49}$ ($WO_{2.72}$) nanowires show a large absorption tail in the visible part of the spectrum, which saturates upon oxidation [32, 51]. This effect points to the presence of a large number of oxygen vacancies or substoichiometric crystal structures. For the nanowires with larger diameter, the absorption in the visible and near-IR range drops. Nanorod bundles of the same stoichiometry have rather featureless spectra, with a steady decrease with increasing wavelength [31]. In the case of $W_{19}O_{55}$ ($WO_{2.89}$) nanorods, the extinction spectrum in UV-vis consists of one broad peak situated at 600 nm (2.07 eV) and a strong absorption band at 200–400 nm, similar to that seen in bulk WO_3 [55]. On the other hand, $W_{24}O_{68}$ ($WO_{2.83}$) nanorods support strong LSPRs, as evidenced by a broad peak centred around 900 nm [26]. WO_{3-x} reduced cubic nanosheets have a narrow peak around 220 nm, with a broader one centred around 300 nm [58]. The strong absorption in the long wavelength region is attributed to the new, oxygen vacancies-induced levels below the conduction band.

Qualitatively, the line shapes of the nanotiles and platelets spectra are similar to those of $WO_{2.9}$ ($W_{20}O_{58}$) nanoparticles [54] and WO_{3-x} quantum dots [59]. For the $WO_{2.9}$ NPs, the UV-vis spectrum consists of two shoulders at 220 and 265 nm, and a band at 320 nm with the bandgap estimated at 3.1 eV (400 nm). These NPs are also stoichiometrically the closest to platelets and nanotiles. Quantum dots have a high-intensity high-energy peak followed by broader

bands around 230 and 285 nm. Therefore, the two peaks found in the nanotiles and platelets and positioned at 281 and 323 nm are most likely a consequence of the crystal structure, i.e. the CS planes.

From the measured extinction spectra, direct and indirect optical bandgaps can be calculated using the equation [60]:

$$\alpha = \frac{A(h\nu - E_g)^n}{h\nu},$$

Here, α is the absorption coefficient, A is a constant, and E_g is the indirect bandgap for $n = 1/2$ and direct bandgap in the case of $n = 2$. The corresponding Tauc plots are presented in figure S4.

The optical bandgaps are highly sensitive to morphology and stoichiometry. In the literature, the measured optical bandgaps of bulk WO_3 , bulk $WO_{2.9}$ and $WO_{2.9}$ nanowires were reported at 2.67 eV, 3.05 eV and 3.17 eV, respectively [3, 32]. For $W_{18}O_{49}$ nanorod bundles, the absorption edge is situated at 2.95 eV [31]. The decrease of the bandgap value of these nanorods by approximately 0.5 eV compared to that of the WO_3 nanoparticles of similar size (3.44 eV) [61] is assigned to the presence of new states correlated to the oxygen vacancies. The appearance of these new states can lead to the rise of two indirect absorption edges, as reported for the suboxide nanosheets (at 2.6 eV and 1.11 eV) [58]. In general, the optical bandgap of these nanostructured suboxides is governed by several different processes. The quantum confinement results in the increase of the bandgap, i.e. the smaller the particle, the larger the bandgap. A similar effect can be assigned also to the Burstein–Moss shift [62]. Namely, in the case of n-type metal oxide semiconductors, an increase of dopants (i.e. oxygen vacancies and W^{5+} atoms) shifts the absorption edge to higher energies due to filling states. Consequently, the measured bandgap, as determined from the onset of interband absorption, moves to higher energies (i.e. undergoes a blue shift). On the other hand, in heavily doped semiconductors, bandgap renormalization takes place. As the electrons start interacting with defects and impurities, their energy shifts due to a variety of effects, such as exchange interaction or Coulombic repulsion [63]. Consequently, the bandgap shrinks with increasing doping level, explaining the decrease of the band-gap with the increase of x [64]. The complex interplay of all these effects makes the value of the bandgap difficult to predict.

For both the nanotiles and platelets, an increase of the indirect bandgap is observed. However, there is an opening of another, lower energy bandgap. This bandgap appears as a consequence of the altered electronic structure due to bond length changes caused by oxygen vacancies and formation of CS planes with W atoms in lower oxidation states. The appearance of two indirect absorption edges was previously reported in suboxide nanosheets [58]. The two indirect bandgaps appear at 3.76 and 3.17 eV for the platelets and at 3.48 and 2.78 eV for the nanotiles. The former value can be assigned to the regular bandgap (between the VB and the CB), while the latter appears

between a new, defect-induced band and CB. The regular gap coincides with the transitions observed in the extinction spectra. These values lie in the upper range of the bandgaps reported in the literature, which is attributed to the distortions in the WO_6 octahedra in such sub-stoichiometric materials [12, 24].

Nanowires show the indirect bandgap values of 2.16 and 2.62 eV for W_5O_{14} and $\text{W}_{18}\text{O}_{49}$, respectively. As these materials show LSPR fingerprints and therefore free charge carriers, their bandgap decreased with respect to WO_3 .

The calculated direct optical bandgap is 4.11 eV (302 nm) for the platelets and 4.05 eV (306 nm) for the nanotiles. These values are in good agreement with the dominant PL peaks that are situated at 4.15 eV and 4.11 eV for the platelets and nanotiles, respectively. As discussed previously, both recorded PL bands are in the UV region, in the 3.9–4.2 eV range and can be assigned to two resonant states introduced by oxygen vacancies [27, 47]. Namely, an electron–hole pair forms an exciton near the oxygen vacancy. When an electron is excited to a state at or above the resonance, it can be trapped. The emission bands in the UV are thus attributed to electron–hole recombination, where the electron comes from one of the two resonant levels in the CB, while the hole occupies the VB. Therefore, the direct bandgap stems from optical transitions related to the defect states. These transitions and the corresponding bandgaps are at the same positions for nanotiles and platelets, confirming their similar stoichiometry. The band gap values and extinction peak positions are presented in table 2.

4. Conclusions

Structural and optical properties of four different WO_{3-x} nanostructures with different morphologies and/or stoichiometries are presented. While the two quasi-2D materials show polycrystallinity, nanowires are of uniform W_5O_{14} and $\text{W}_{18}\text{O}_{49}$ composition. Raman spectra reveal that less oxidized $\text{W}_x\text{O}_{3x-1}$ stoichiometries have higher number of W–O bonds with well-defined lengths, whereas more reduced tungsten suboxides have a higher number of W–O–W bonds with well-defined bond angles. The extinction spectra reveal the appearance of excitonic states for the less oxidized $\text{W}_x\text{O}_{3x-1}$ stoichiometries and two indirect bandgaps deduced from the Tauc plots. Both values appear in the upper range reported for suboxide materials, which can be explained by the formation of oxygen vacancies. The extinction spectra of the more reduced tungsten suboxides show the presence of LSPR in the near-IR region. Their bandgaps are lower, as they have a higher number of free charge carriers, confirmed by the LSPR-like peaks. PL spectra reveal two distinct emission peaks in the UV range, present in all four nanomaterials. They are attributed to electron–hole recombination, with the hole stemming from the VB and electron from one of the resonant states within the CB. Furthermore, the effects of stoichiometry and CS planes are discussed in relation to the understanding of the optical properties.



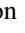
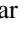
Acknowledgments

This work was financially supported by the Slovenian Research Agency through contracts P1-0099 and P1-0192. BV, MO, AM and NL acknowledge funding provided by the Institute of Physics Belgrade, through the grant by the Ministry of Education, Science, and Technological Development of the Republic of Serbia and Center for Solid State Physics and New Materials. Authors are grateful to Janez Jelenc (Jozef Stefan Institute) for KPFM measurements, and Lina Senica for technical assistance with the photoluminescence measurements.

Data availability statement

All data that support the findings of this study are included within the article (and any supplementary files).

ORCID iDs

Bojana Višić  <https://orcid.org/0000-0002-2065-0727>
 Luka Pirker  <https://orcid.org/0000-0003-0741-0048>
 Boris Majaron  <https://orcid.org/0000-0003-2841-8276>
 Maja Remškar  <https://orcid.org/0000-0002-8919-1768>

References

- [1] Mahjabin S *et al* 2021 Effects of oxygen concentration variation on the structural and optical properties of reactive sputtered WO_x thin film *Sol. Energy* **222** 202–11
- [2] Thummavichai K, Xia Y and Zhu Y 2017 Recent progress in chromogenic research of tungsten oxides towards energy-related applications *Prog. Mater. Sci.* **88** 281–324
- [3] Huang Z F, Song J, Pan L, Zhang X, Wang L and Zou J J 2015 Tungsten oxides for photocatalysis, electrochemistry, and phototherapy *Adv. Mater.* **27** 5309–27
- [4] Pirker L and Višić B 2021 Recent progress in the synthesis and potential applications of two-dimensional tungsten (Sub) oxides *Isr. J. Chem.* (<https://doi.org/10.1002/ijch.202100074>)
- [5] Zhang X, Wei Y and Yu R 2022 Multi-dimensional tungsten oxides for efficient solar energy conversion *Small Structures* **3** 2100130
- [6] Liu J, Zhong M, Li J, Pan A and Zhu X 2015 Few-layer WO_3 nanosheets for high-performance UV-photodetectors *Mater. Lett.* **148** 184–7
- [7] He Z, Liu Q, Hou H, Gao F, Tang B and Yang W 2015 Tailored electrospinning of WO_3 nanobelts as efficient ultraviolet photodetectors with photo-dark current ratios up to 1000 *ACS Appl. Mater. Interfaces* **7** 10878–85
- [8] Aguir K, Lemire C and Lollman D 2002 Electrical properties of reactively sputtered WO_3 thin films as ozone gas sensor *Sensors Actuators B* **84** 1–5
- [9] Zhang C *et al* 2011 Highly sensitive hydrogen sensors based on co-sputtered platinum-activated tungsten oxide films *Int. J. Hydrogen Energy* **36** 1107–14
- [10] Hariharan V, Gnanavel B, Sathiyapriya R and Aroulmoji V 2019 A review on tungsten oxide (WO_3) and their derivatives for sensor applications *Int. J. Adv. Sci. Eng.* **5** 1163–8

- [11] Sayama K, Mukasa K, Abe R, Abe Y and Arakawa H 2001 Stoichiometric water splitting into H₂ and O₂ using a mixture of two different photocatalysts and an IO₃⁻/I⁻ shuttle redox mediator under visible light irradiation *Chem. Commun.* **23** 2416–7
- [12] Wang G, Ling Y and Li Y 2012 Oxygen-deficient metal oxide nanostructures for photoelectrochemical water oxidation and other applications *Nanoscale*. **4** 6682–91
- [13] Miyazaki H, Ishigaki T and Ota T 2017 Photochromic smart windows employing WO₃-based composite films *J. Mater. Sci. Res.* **6** 62–6
- [14] Hai Z, Wei Z, Xue C, Xu H and Verpoort F 2019 Nanostructured tungsten oxide thin film devices: from optoelectronics and ionics to iontronics *J. Mater. Chem. C* **7** 12968–90
- [15] Granqvist C G 2000 Electrochromic tungsten oxide films: review of progress 1993–1998 *Sol. Energy Mater. Sol. Cells* **60** 201–62
- [16] González-Borrero P et al 2010 Optical band-gap determination of nanostructured WO₃ film *Appl. Phys. Lett.* **96** 061909
- [17] He T and Yao J 2007 Photochromic materials based on tungsten oxide *J. Mater. Chem.* **17** 4547–57
- [18] Zheng H, Ou J Z, Strano M S, Kaner R B, Mitchell A and Kalantar-zadeh K 2011 Nanostructured tungsten oxide—properties, synthesis, and applications *Adv. Funct. Mater.* **21** 2175–96
- [19] Polaczek A, Pekala M and Obuszko Z 1994 Magnetic susceptibility and thermoelectric power of tungsten intermediary oxides *J. Phys.:Condens. Matter* **6** 7909
- [20] Tilley R 1970 The formation of shear structures in sub-stoichiometric tungsten trioxide *Mater. Res. Bull.* **5** 813–23
- [21] Pickering R and Tilley R 1976 An electron microscope study of tungsten oxides in the composition range WO₂. 90 · WO₂. 72 *J. Solid State Chem.* **16** 247–55
- [22] Magnéli A 1953 Structures of the ReO₃-type with recurrent dislocations of atoms: homologous series' of molybdenum and tungsten oxides *Acta Crystallogr.* **6** 495–500
- [23] Lundberg M, Sundberg M and Magnéli A 1982 The 'pentagonal column' as a building unit in crystal and defect structures of some groups of transition metal compounds *J. Solid State Chem.* **44** 32–40
- [24] Mohamed A M, Amer A W, AlQaradawi S Y and Allam N K 2016 On the nature of defect states in tungstate nanoflake arrays as promising photoanodes in solar fuel cells *Phys. Chem. Chem. Phys.* **18** 22217–23
- [25] Deb S K 2008 Opportunities and challenges in science and technology of WO₃ for electrochromic and related applications *Sol. Energy Mater. Sol. Cells* **92** 245–58
- [26] Manthiram K and Alivisatos A P 2012 Tunable localized surface plasmon resonances in tungsten oxide nanocrystals *JACS* **134** 3995–8
- [27] Karazhanov S Z, Zhang Y, Mascarenhas A, Deb S and Wang L-W 2003 Oxygen vacancy in cubic WO₃ studied by first-principles pseudopotential calculation *Solid State Ionics* **165** 43–9
- [28] Migas D, Shaposhnikov V and Borisenko V 2010 Tungsten oxides. II. The metallic nature of Magnéli phases *J. Appl. Phys.* **108** 093714
- [29] Remškar M, Kovac J, Viršek M, Mrak M, Jesih A and Seabaugh A 2007 W₅O₁₄ nanowires *Adv. Funct. Mater.* **17** 1974–8
- [30] Shi S, Xue X, Feng P, Liu Y, Zhao H and Wang T 2008 Low-temperature synthesis and electrical transport properties of W₁₈O₄₉ nanowires *J. Cryst. Growth* **310** 462–6
- [31] Su C-Y and Lin H-C 2009 Direct route to tungsten oxide nanorod bundles: microstructures and electro-optical properties *J. Phys. Chem. C* **113** 4042–6
- [32] Paik T et al 2018 Photocatalytic hydrogen evolution from substoichiometric colloidal WO_{3-x} nanowires *ACS Energy Lett.* **3** 1904–10
- [33] Song K, Liu X, Tian C, Deng H, Wang J and Su X 2019 Oxygen defect-rich WO_{3-x} nanostructures with high photocatalytic activity for dehydration of isopropyl alcohol to propylene *Surf. Interfaces* **14** 245–50
- [34] Wang F, Di Valentin C and Pacchioni G 2011 Semiconductor-to-metal transition in WO_{3-x}: nature of the oxygen vacancy *Phys. Rev. B* **84** 073103
- [35] Saqib M et al 2020 Field emission properties of single crystalline W₅O₁₄ and W₁₈O₄₉ nanowires *J. Electron. Spectrosc. Relat. Phenom.* **241** 146837
- [36] Pirker L, Višić B, Škapin S D, Dražić G, Kovač J and Remškar M 2020 Multi-stoichiometric quasi-two-dimensional W_n O 3n– 1 tungsten oxides *Nanoscale*. **12** 15102–14
- [37] Pirker L, Višić B, Kovač J, Škapin S D and Remškar M 2021 Synthesis and characterization of tungsten suboxide W_nO_{3n– 1} nanotiles *Nanomaterials*. **11** 1985
- [38] Maeda F, Takahashi T, Ohsawa H, Suzuki S and Suematsu H 1988 Unoccupied-electronic-band structure of graphite studied by angle-resolved secondary-electron emission and inverse photoemission *Phys. Rev. B* **37** 4482
- [39] Lanzoni E M et al 2021 The impact of Kelvin probe force microscopy operation modes and environment on grain boundary band bending in perovskite and Cu (In, Ga) Se₂ solar cells *Nano Energy* **88** 106270
- [40] Daniel M, Desbat B, Lassegues J, Gerand B and Figlarz M 1987 Infrared and Raman study of WO₃ tungsten trioxides and WO₃ · xH₂O tungsten trioxide hydrates *J. Solid State Chem.* **67** 235–47
- [41] Hardcastle F D and Wachs I E 1995 Determination of the molecular structures of tungstates by Raman spectroscopy *J. Raman Spectrosc.* **26** 397–405
- [42] Johansson M B, Zietz B, Niklasson G A and Österlund L 2014 Optical properties of nanocrystalline WO₃ and WO_{3-x} thin films prepared by DC magnetron sputtering *J. Appl. Phys.* **115** 213510
- [43] Lee K, Seo W S and Park J T 2003 Synthesis and optical properties of colloidal tungsten oxide nanorods *JACS* **125** 3408–9
- [44] Feng M et al 2005 Strong photoluminescence of nanostructured crystalline tungsten oxide thin films *Appl. Phys. Lett.* **86** 141901
- [45] Hong K, Xie M, Hu R and Wu H 2007 Synthesizing tungsten oxide nanowires by a thermal evaporation method *Appl. Phys. Lett.* **90** 173121
- [46] Wang J, Lee P S and Ma J 2009 Synthesis, growth mechanism and room-temperature blue luminescence emission of uniform WO₃ nanosheets with W as starting material *J. Cryst. Growth* **311** 316–9
- [47] Luo J Y, Xu N S, Zhao F L, Deng S Z and Tao Y T 2011 Ultraviolet superfluorescence from oxygen vacancies in WO_{3-x} nanowires at room temperature *J. Appl. Phys.* **109** 024312
- [48] Wang B, Zhong X, He C, Zhang B, Cvelbar U and Ostrikov K 2021 Nanostructure conversion and enhanced photoluminescence of vacancy engineered substoichiometric tungsten oxide nanomaterials *Mater. Chem. Phys.* **262** 124311
- [49] Wang D et al 2013 High-performance gas sensing achieved by mesoporous tungsten oxide mesocrystals with increased oxygen vacancies *J. Mater. Chem. A* **1** 8653–7
- [50] Walkingshaw A D, Spaldin N A and Artacho E 2004 Density-functional study of charge doping in WO₃ *Phys. Rev. B* **70** 165110
- [51] Xi G et al 2012 Ultrathin W₁₈O₄₉ nanowires with diameters below 1 nm: synthesis, near-infrared absorption,

- photoluminescence, and photochemical reduction of carbon dioxide *Angew. Chem. Int. Ed.* **51** 2395–9
- [52] Guo C, Yin S, Dong Q and Sato T 2012 The near infrared absorption properties of $W_{18}O_{49}$ *RSC Adv.* **2** 5041–3
- [53] Guo C, Yin S, Yan M, Kobayashi M, Kakihana M and Sato T 2012 Morphology-controlled synthesis of $W_{18}O_{49}$ nanostructures and their near-infrared absorption properties *Inorg. Chem.* **51** 4763–71
- [54] Barreca F, Acacia N, Spadaro S, Curro G and Neri F 2011 Tungsten trioxide (WO_{3-x}) nanoparticles prepared by pulsed laser ablation in water *Mater. Chem. Phys.* **127** 197–202
- [55] Qian J, Zhao Z, Shen Z, Zhang G, Peng Z and Fu X 2016 Oxide vacancies enhanced visible active photocatalytic $W_{19}O_{55}$ NMRs via strong adsorption *RSC Adv.* **6** 8061–9
- [56] Salje E and Güttler B 1984 Anderson transition and intermediate polaron formation in WO_{3-x} Transport properties and optical absorption *Philos. Mag. B* **50** 607–20
- [57] Hjelm A, Granqvist C G and Wills J M 1996 Electronic structure and optical properties of WO_3 , $LiWO_3$, $NaWO_3$, and HWO_3 *Phys. Rev. B* **54** 2436
- [58] Fang Z et al 2017 Synthesis of reduced cubic phase WO_{3-x} nanosheet by direct reduction of $H_2WO_4 \cdot H_2O$ *Mater. Today Energy* **6** 146–53
- [59] Wang Y et al 2017 Simultaneous synthesis of WO_{3-x} quantum dots and bundle-like nanowires using a one-pot template-free solvothermal strategy and their versatile applications *Small* **13** 1603689
- [60] Pankove J I 1971 *Optical Processes in Semi-Conductors* (Mineola, NY: Dover Publications, Inc)
- [61] He T et al 2002 Photochromism of WO_3 colloids combined with TiO_2 nanoparticles *J. Phys. Chem. B* **106** 12670–6
- [62] Sarkar A, Ghosh S, Chaudhuri S and Pal A 1991 Studies on electron transport properties and the Burstein-Moss shift in indium-doped ZnO films *Thin Solid Films* **204** 255–64
- [63] Walsh A, Da Silva J L and Wei S-H 2008 Origins of band-gap renormalization in degenerately doped semiconductors *Phys. Rev. B* **78** 075211
- [64] Smith W, Zhang Z-Y and Zhao Y-P 2007 Structural and optical characterization of WO_3 nanorods/films prepared by oblique angle deposition *J. Vac. Sci. Technol. B* **25** 1875–81

Recent Progress in the Synthesis and Potential Applications of Two-Dimensional Tungsten (Sub)oxides

Luka Pirker^[a] and Bojana Višić^{*[a, b]}

Abstract: While WO_3 is one of the most studied metal-oxides in bulk, it is increasingly gaining interest as a two-dimensional (2D) material as it exhibits different behaviour compared to bulk. In addition, many substoichiometric WO_{3-x} ($0 \leq x \leq 1$) phases exist both in bulk and 2D form. These Magneli phases have different physical and chemical properties than their WO_3 counterparts. By introducing oxygen vacancies, the physical and chemical properties of 2D

tungsten (sub)oxide nanomaterials can be further altered. This review focuses on synthesis pathways of 2D tungsten (sub)oxides reported so far, and their subsequent use for various applications. The different stoichiometries and additional oxygen vacancies that appear in these materials, combined with their low thickness and high surface area, make them interesting candidates for gas sensing, catalytic application or in electronic devices.

Keywords: two-dimensional materials · metal oxides · tungsten suboxides · synthesis · applications

1. Introduction

Tungsten (VI) oxide (WO_3) is one of the most investigated transition metal oxides due to various potential applications, such as in photochromic smart windows,^[1] in optoelectronics,^[2] gas sensing and photocatalysis,^[3] as supercapacitors,^[4] as nanostructured thermoelectrics,^[5] etc. The WO_3 forms a rich variety of crystal structures composed of corner-sharing WO_6 octahedra, which differ in tilting angles, displacements of the W cation from the centre of the octahedron, and rotation of WO_6 octahedra with respect to ideal cubic (ReO_3 type) structure.^[5] In bulk, partially reversible inter-phase transformations occur upon heating in addition to the formation of a metastable phase.^[6] At nanoscale, phase transitions occur at temperatures lower than in bulk and depend mostly on the size of WO_3 nanoparticles.^[7]

Recently, two-dimensional (2D) nanostructures, including 2D- WO_3 , have attracted a lot of attention among researchers due to their novel physical and chemical properties, which differ from their bulk counterparts.^[8] High surface area, appearance of crystalline planes/surfaces that are not available in bulk materials, and stability of crystal phases declared as metastable in bulk systems are just some of the examples. Due to their low-dimensional nature, quantum confinement effects come into play, changing their electronic properties. This is providing a great opportunity for their use as components in novel sensors, energy conversion devices, transistors, to name a few. Different particular particle shapes, such as pseudo-spherical nanometre-sized particles, nanowires, nano-discs and flakes, were already synthesized with various growth techniques.^[9]

Besides the stoichiometric WO_3 , many substoichiometric WO_{3-x} phases exist, where $0 \leq x \leq 1$. The electrical, optical, and structural properties of tungsten suboxides depend strongly on the degree of reduction (i. e. x) and consequently

differ from stoichiometric WO_3 .^[10] Moreover, for additional tuning of their properties, oxygen vacancies can be induced in WO_3 or WO_{3-x} . The abundance of tungsten ore in combination with the low-dimensional nature, a wide range of substoichiometric phases that can be further altered by inducing oxygen vacancies, 2D tungsten (sub)oxides offer a platform with diverse and tuneable properties for a great variety of applications.

This review focuses on current synthesis approaches to obtaining 2D tungsten (sub)oxide materials. In addition, the progress in their utilization in various applications, such as gas sensing, catalysis and photodetection, is discussed in terms of current state of the art and future outlook.

2. Synthesis, Morphology and Structure

One of the first 2D- WO_3 crystals was prepared more than 15 years ago, when monoclinic WO_3 nanosheets were synthesized by a solvothermal reaction.^[11] The square nanosheets were 150 nm in size and thin enough for a direct HRTEM

[a] Dr. L. Pirker, B. Višić
Solid State Physics, Jozef Stefan Institute
Jamova cesta 39, 1000 Ljubljana, Slovenia

[b] B. Višić
Institute of Physics Belgrade, University of Belgrade
Pregrevica 118, 11080 Belgrade, Serbia
Phone: +381113713000
Fax: +381113162190
E-mail: bojana.visic@ipb.ac.rs

© 2021 The Authors. *Israel Journal of Chemistry* published by Wiley-VCH GmbH. This is an open access article under the terms of the Creative Commons Attribution License, which permits use, distribution and reproduction in any medium, provided the original work is properly cited.

analysis. In the following years, different methods of synthesis were reported. The 2D-WO₃ nanoparticles were crystallized in the monoclinic WO₃ phase via wet chemical synthesis,^[12] topochemical conversion,^[13] hydrothermal,^[8] solvothermal,^[14] exfoliation and oxidation of WS₂,^[15] and microwave irradiation,^[16] to name a few. The morphologies of synthesized nanoparticles range from rectangular nanoplates,^[13] irregularly shaped nanodisks,^[13] leaf-like nanoplatelets,^[17] and nanoflakes,^[18] with the sizes ranging from 20 nm to 500 nm in lateral dimensions and from 5 nm to 60 nm in thickness. An example of a nanoplate is shown in Figure 1 a, b).

Although at room temperature only the monoclinic WO₃ phase is stable in bulk, other crystal structures were stabilized in form of 2D-WO₃ crystals. Hexagonal WO₃ nanosheets were synthesized from the colloidal suspension of BaWO₄-PAA^[19] orthorhombic WO₃ nanoplates were synthesized using sodium tungsten Na₂WO₄·2H₂O as precursor by a simple free template precipitation method,^[20] triclinic WO₃ nanoparticles were synthesized through a hydrothermal route,^[21] and cubic WO₃ nanosheets were synthesized by direct reduction.^[22] Novel octahedral molecular sieves (h'-WO₃) with the diameter between 20 and 80 nm and thickness of 3–10 nm were also synthesized and are shown in Figure 1 c).^[23]

With various synthesis methods, different crystal facets could be exposed, which are not available in bulk materials. It was reported that (100), (010), and (001) facets could be exposed with the use of different surfactants,^[12,24] solvents,^[21] specific precursors,^[13,25] or the synthesis method. Their atomic structure and electronic properties differ due to the nature of the crystal structure, and thus play an important part in the physical and chemical properties of the material.^[26] For example, it was reported that (100) facets show higher evolution rate of O₂ in water splitting than WO₃ without a preferred crystal face.^[26b]

As stated in the Introduction, the stoichiometric WO₃ can also be reduced into substoichiometric WO_{3-x} using different techniques such as chemical vapor transport (CVT),^[27] heating under controlled atmosphere,^[28] and electron beam irradiation in a TEM microscope.^[28b,29] The substoichiometric WO_{3-x} can

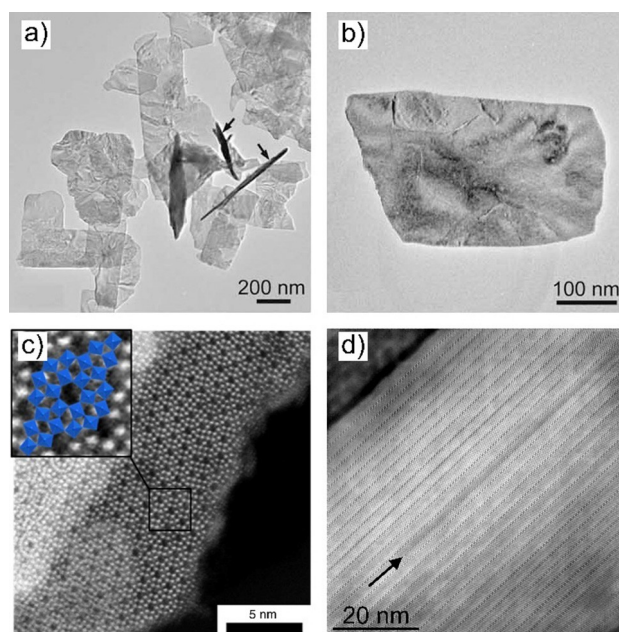
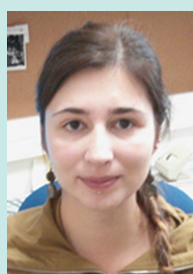


Figure 1. a) Low-magnification and b) high magnification TEM images of WO₃ nanoplates (Reprinted from reference [13] with permission from John Wiley and Sons); c) HAADF-STEM micrograph of a h'-WO₃ framework. The inset shows the arrangement of tungsten octahedra (Reprinted from reference [23] with permission from Springer Nature); d) HRTEM image of a cross-section lamella showing semi-regularly distributed CS planes in a W_nO_{3n-1} tungsten suboxide. The arrow points to a defect (Reprinted from reference [10] with permission from the Royal Society of Chemistry.)

be synthesized with a wide variety of hydrothermal and solvothermal methods,^[30] layer deposition methods, such as atomic layer deposition (ALD) and chemical vapour deposition (CVD).^[31] These suboxides grow in different structures such as films,^[32] needles,^[33] nanowires,^[27] nanorods^[34] and nanodots^[35] and can crystallize in similar structures as tungsten bronzes with a general formula A_xWO₃, where A is an electropositive element.^[36] While in the tungsten bronzes W⁵⁺



Dr. Luka Pirker obtained his BS and MSc in physics at the Faculty of Mathematics and Physics, University of Ljubljana in Slovenia. He finished his PhD in physics at the Faculty of Mathematics and Physics, University of Ljubljana in Slovenia in 2020 under the supervision of prof. Maja Remškar. He is currently working at Jozef Stefan Institute, Slovenia. During his PhD he investigated the structural, optical, and electrical properties of low-dimensional tungsten suboxides. He is also interested in low-dimensional transition metal dichalcogenides and their structural, optical, and electrical properties.



Assoc. Res. Prof. Bojana Višić completed her BS and MSc at the Faculty of Physics, Belgrade, Serbia in 2007 and 2008, respectively. She received her PhD at Faculty of Mathematics and Physics, Ljubljana, Slovenia in 2013, under the guidance of Prof. Maja Remškar. Afterwards she joined the groups of prof. Reshef Tenne (Weizmann Institute of Science, Israel) and prof. Maja Remškar (Jozef Stefan Institute, Slovenia) as a postdoctoral fellow in 2013–2017 and 2017–2018. In December 2018, she joined the Center for Solid State Physics and New Materials at the Institute of Physics, Belgrade, Serbia. Her main research interests focus on low-dimensional materials, namely inorganic nanotubes, their characterization and optical properties.

state appears due to the presence of the electropositive element, in WO_{3-x} it occurs through the intrinsic oxygen vacancies. It has been shown that even when x in WO_{3-x} is less than 0.0001, the oxygen atoms are not removed randomly but form ordered structures.^[28a] Within the material, crystallographic shear (CS) planes, pentagonal columns (PC), and oxygen vacancy walls (OVW) are formed to accommodate the oxygen vacancies, as shown in Figure 2.

The term crystallographic shear comes from the shearing of two adjacent blocks of WO_3 . In a CS plane, corner sharing WO_6 octahedra that are a part of the CS plane become edge sharing WO_6 octahedra.^[38] While a single CS plane is considered a defect, an array of equally spaced CS planes forms a WO_{3-x} crystal with a defined stoichiometry. The CS planes can be described in terms of $\{hkl\}_r$ planes of WO_3 , which crystallize in the ReO_3 type structure.^[39] For $x < 0.007$, the $\{102\}_r$ CS planes are randomly distributed.^[28a] The increase of the degree of reduction (i. e. increasing x) increases the density of CS planes, resulting in a formation of their ordered arrays, which form the $\text{W}_n\text{O}_{3n-1}$ tungsten suboxides. When x approaches 0.1, the formation of $\{103\}_r$ CS planes become favourable over the formation of $\{102\}_r$ CS planes, forming the $\text{W}_n\text{O}_{3n-2}$ tungsten suboxides. While CS planes are observed in less reduced WO_{3-x} ($x \leq 0.2$), PC structures form only in more reduced WO_{3-x} ($x \geq 0.2$). The PC are periodic structures of WO_7 bipyramids that share their equatorial edges with WO_6 octahedra.^[40] Within structures with PC, three-, four-, five- and six-sided tunnels can also form as in the case of $\text{W}_{18}\text{O}_{49}$ or W_5O_{14} .^[27,41] Although OVW were proposed as the precursors of CS planes, there are very few articles where these were experimentally observed.^[42] The abundance of CS planes and PCs largely depends on the degree of reduction.

With sufficiently low reduction, single oxygen vacancies can be produced.^[43] In this case, oxygen atoms are removed from the surface, forming oxygen vacancies. To minimize the surface energy, single PCs appear on the surface, stabilizing the structure. Although technically oxygen vacancies reduce WO_3 into WO_{3-x} , in the majority of the materials reported in the literature, it is not clear what kind of structure formed within the material. Thus, the term substoichiometric tungsten oxides (WO_{3-x}) is used interchangeably in literature for

materials with ordered CS and PC structures, as well as for materials with induced oxygen vacancies.

For 2D- WO_{3-x} materials, different stoichiometries were identified, such as $\text{W}_{18}\text{O}_{49}$ ^[44] and $\text{W}_{10}\text{O}_{29}$ nanosheets,^[45] as well as materials with mixed stoichiometry,^[30b] multi-stoichiometric nanoplates,^[10,46] and nanomaterials with unknown stoichiometries.^[47] Similarly to 2D nanoparticles, 2D- WO_3 and 2D- WO_{3-x} thin films can be made using atomic layer deposition,^[31a] molecular beam epitaxy,^[48] and vapor-phase deposition.^[31b] Different stoichiometries can be prepared, from monoclinic WO_3 ,^[31a] to $\text{W}_{18}\text{O}_{49}$,^[49] and WO_2+O bilayer structure,^[31b] with the thickness ranging from a monolayer up to several tens of nm. Owing to the large area of deposited films, they can be used in many applications such as electrochromic displays, solar cells, and supercapacitors.^[50] Due to the formation of CS planes, as shown in Figure 1d), the electronic and optical properties differ from monoclinic WO_3 and they may have an advantage in applications such as water splitting,^[37,51] near-infrared shielding,^[44] as anode materials for high-performance Li-ion batteries,^[52] photocatalysis,^[53] and in domain boundary engineering.^[54]

Although the majority of the reported stoichiometries were determined from XRD measurements, it is not the most suitable and precise method to use in the case of tungsten suboxides, as the differences between phases are too small to be detected.^[39] Only for highly crystalline samples, where the diffraction peaks from the low index (hkl) planes are observed, can the stoichiometry be determined by using XRD as the main tool. HRTEM images and electron diffraction patterns can be used to further elucidate the true crystal structure of tungsten (sub)oxides.

A short summary of the synthesis methods, particle sizes, crystal structures, exposed faces, and applications of 2D- WO_3 and 2D- WO_{3-x} is presented in Table 1.

3. 2D- WO_{3-x} for Applications

Among the biggest advantages of the 2D morphology are the large specific surface area, increased number of active sites and confined thickness, which make these nanostructures promising candidates for gas sensing, catalytic applications and electronic or photonic devices. Additionally, the 2D- WO_3 and 2D- WO_{3-x} are interesting from the aspect of defect engineering, where finding the optimal concentration of oxygen vacancies could lead to fine bandgap tuning, increased amount of charge carriers and photocurrents, whilst maintaining the crystallinity. Nevertheless, ultrathin WO_{3-x} nanosheets have not been sufficiently studied in terms of applications, despite their substantial amount of reactive (002) crystal facets and a high specific surface area.

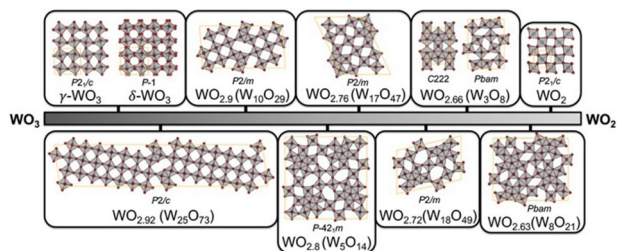


Figure 2. Crystal structures of some stoichiometric and sub-stoichiometric tungsten oxides. Reprinted with permission from reference [37]. Copyright 2021 American Chemical Society.

Table 1. A short summary of the synthesis methods, particle sizes, crystal structures, exposed faces, and applications of 2D-WO_{3-x} nanomaterials.

Synthesis method	Lateral size (nm)	Thickness (nm)	Crystal structure	Exposed faces	Application	Morphology
Wet chemical ^[12]	200–1000	7–18	Monoclinic WO ₃	(010)	Water splitting	nanodisks
topochemical conversion ^[13]	200–500	10–30	Monoclinic WO ₃	(001)	Water splitting	nanoplates
hydrothermal ^[55]	A few 100	~10	Monoclinic WO ₃	(200)	NO ₂ gas detection	nanosheets
Laser ablation ^[17]	600–1800 μm	30	Monoclinic WO ₃	(001)	/	leaf-like nanoplatelets
Aqueous Synthesis ^[19]	Several 100	5–60	Hexagonal WO ₃	(001)	/	nanosheets
wet chemical ^[20]	Up to 175	~40	Orthorhombic WO ₃	(010)	CO oxidation	nanoplatelets
hydrothermal ^[21]	< 200 nm	30–175	Triclinic WO ₃	(100), (010), (001)	Gas sensing	nanosheets
thermal decomposition ^[56]	Up to a few 10	/	W ₁₈ O ₄₉	(020)	Photocatalytic decomposition	nanosheets
CVT ^[10]	Up to 4000	10–100	W _n O _{3n-1}	(001)	/	nanoplates
direct current sputtering ^[49]	/	> 52	W ₁₈ O ₄₉	/	water splitting	film
ALD ^[31a]	/	~42	Monoclinic WO ₃	(002)	Gas sensor	film
Vapor-phase deposition ^[31b]	9–4	monolayer	WO ₂ + O bilayer	/	/	clusters

3.1 Gas Sensing

Materials preferred in gas sensing applications tend to have a good adsorption-desorption mechanism and a pore-rich morphology. This makes 2D-WO₃ and 2D-WO_{3-x} promising candidates, since the oxygen vacancies play an important role in adsorption-desorption phenomena. In order to obtain the enhanced gas-sensing performances, morphology and surface design are required. Other important parameters for optimization of sensor performance are sensitivity, stability, selectivity, adsorption and desorption ability, crystal structure, electronic and chemical properties etc. In addition, since these reactions rely closely on the interaction of the surface of the material and the target molecules, the performance depends strongly on the exposed facets and surface area. Different facets of the same structure can have different dangling bonds and electronic structure, exhibiting different physical and chemical properties. As seen in Section 2, tuning the synthesis can expose selected facets^[26b], with which the gas sensing ability can be optimized. When it comes to gas sensing capabilities of metal oxides, they are mostly based on the oxidation-reduction reaction of the detected gases.^[57] As the oxidation-reduction reaction takes place on the surface, the physical and chemical properties of the facets play an important role. If the planes are terminated with positive ions, they are able to adsorb the oxygen species and target molecules due to unsaturated oxygen coordination, improving gas sensing capabilities. It was shown that for the monoclinic WO₃, (002) crystal facets exhibit enhanced photocatalytic CO₂ reduction and photoelectrochemical (PEC) water splitting capabilities compared to (200) and (020) facets, due to improved photoinduced charge carrier separation efficiency.^[26a] Another important factor for gas sensing is selectivity. The sensor has to be able to discriminate the selected gas in a mixture of gases, and this is

determined by the adsorption and subsequent chemical oxidation on the surface of the potential sensor material. The sensitivity is largely affected by geometrical and chemical heterogeneities of the reacting surface. Materials with higher amount of surface defects, where adsorption and catalytic reaction may take place, are preferred.

Reducing NO₂ emissions is an important task, as very low concentrations (1 ppm) can induce respiratory issues.^[58] Since NO₂ sensors should operate in the ambient oxygen environment, materials under consideration need to have good air durability, as well as high selectivity and sensitivity, fast response and recovery time. 150 nm thick WO₃ films were shown to be good candidates for NO₂ sensing.^[59] Here, Cantalini *et al.* showed that the sensor sensitivity increases with the increase in surface defects concentration, while the long-term stability depends on the optimization of the annealing process of the films. In this case, the films were more stable when annealed for longer times, which stabilizes the surface defects.^[55] In a different study, 10 nm thick WO_{3-x} nanosheets showed high sensitivity and selectivity to NO₂. The best performance was obtained at 50 ppb NO₂ at 140 °C with response and recovery times of 140 s and 75 s, respectively. With a further reduced thickness, Khan *et al.* made physisorption-based NO₂ sensors from 4 nm thick substoichiometric WO_{3-x} nanosheets.^[60] The optimal operating temperature for samples annealed at different temperatures was 150 °C. This temperature is significantly lower than for the conventional chemisorptive metal oxide gas sensors, which operate above 200 °C. As the operating temperature increased, the response decreased. In this regime, the rate of adsorption is lower than the rate of desorption. The best responsivity (here, the input/output ratio of the electrical resistance) to 40 ppb was reported to be 30, which is more than an order of magnitude higher than for the nanocrystals.^[60] This work furthermore empha-

Review

sizes the influence of the stoichiometry on performance and properties. These materials were tested in the NO₂ concentration range of 20 to 2000 ppb, but the sample annealed at 225 °C was overly sensitive, reaching saturation beyond 120 ppb. The saturation occurs because as the concentration of the NO₂ increases, these surface-adsorbed molecules act as acceptors available to take electrons from the suboxide and at a certain concentration, there are no electrons left. The sample annealed at 225 °C has the WO_{2.96} stoichiometry, which is known to be semiconducting, while the unannealed and annealed at 450 °C have the WO_{2.92} stoichiometry that is more metallic and requires more electron transfer for full off/on switching. Therefore, the changes in crystal structure and stoichiometry can result in different performance of sensors. The same samples were studied for NH₃, H₂S, CO₂, H₂ and humidity sensing, but showed far less promise. This is explained with greater molecule-surface binding energies for NO₂ and WO₃.

In another study, WO₃ nanosheets prepared by microwave irradiation method showed promise as humidity sensors.^[61] With the relative humidity working range of 10–90%, the maximum sensitivity was estimated to be 98%, with the response and recovery time of 25 and 15 s, respectively. They showed high stability, with only a 3% drop in performance after three months, making them suitable candidates for high performance sensing.

Ultrathin (5 nm) WO₃ sheets were successfully used as gas sensing material for the detection of xylene, a volatile organic compound that has adverse effects on human health.^[3] The sensing mechanism can be explained as follows: oxygen molecules from air get adsorbed on the surface of WO₃ and get chemisorbed into O²⁻, O⁻ or O₂⁻ by capturing electrons from the material's conduction band. Upon xylene introduction, it reacts with these species, releasing the trapped electrons. In the case of thin sheets, these charge layers may cover the entire surface, increasing the material's sensitivity.^[3] This sensing mechanism is depicted in Figure 3 a).

2D-WO₃ nanoplatelets with 10–50 nm thickness were used as hydrogen sensors.^[62] The most efficient interaction of WO₃ with the molecules that contain hydrogen atoms is through intercalation. The intercalated H⁺ ions embed themselves into WO₃ lattice, and the electrons released from the lattice are transferred to the lowest unoccupied energy levels. This in turn changes the band structure of the metal oxide and increases the conductivity, which can be used for sensing applications. The mechanism of H₂ sensing is based on the changes in electrical conductance, which strongly depends on the content of oxygen vacancies and H⁺ ions. The oxygen adsorbing capabilities in turn depend on the surface area of the material, morphology and the operating temperature. As the oxygen species adsorbed on the surface capture electrons from the material, the hole concentration increases, forming an electron-depleted layer at the surface of the platelets.^[62]

Triclinic WO₃ nanosheets with 35 nm thickness were synthesized in a process that enables the control of the exposed facets.^[21] These nanosheets were used as l-butylamine sensors,

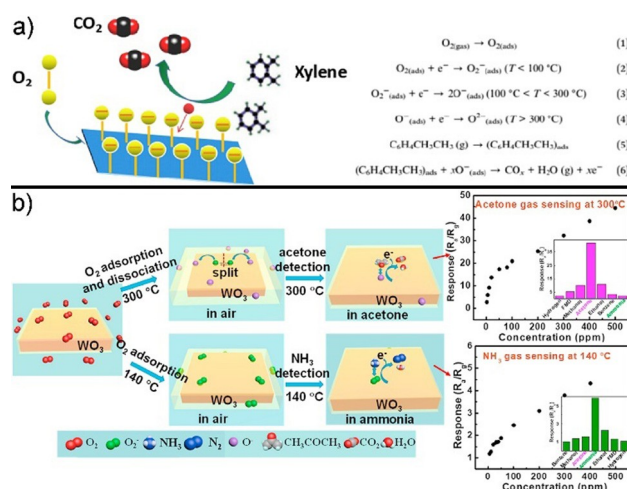


Figure 3. Schematic illustrations of the sensing mechanism of 2D-WO₃ towards a) xylene (Reprinted from reference [3], with permission from Elsevier) and b) acetone and ammonia (Reprinted from reference [24], with permission from Elsevier).

and the sheets with the exposed (010) facets demonstrated the best performance. It was shown that (001) and (100) facets have more O-terminated planes, while (010) have more W atoms exposed at the surface. Therefore, as it has more positive ions than other facets, it has better gas sensing capabilities.

As n-type semiconductors, WO_{3-x} materials are good candidates for ethanol sensing.^[63] When the platelets are exposed to air, the oxygen molecules from the atmosphere can get adsorbed on the surface. They can subsequently capture electrons from the conduction band of WO_{3-x}, forming adsorbed oxygen ions (O²⁻, O⁻, O₂⁻), producing an electron-depletion layer on the surface. When the sensor gets exposed to ethanol, the ethanol molecules get chemisorbed on the surface and oxidized by the adsorbed oxygen ions.^[63] The oxidation promotes the return of the depleted electrons back to the conduction band, resulting in the decrease of the thickness of the electron-depletion layer. As a result, upon ethanol exposure, electrical current increases. The sensors of WO₃ nanoplates annealed at different temperatures were tested at the operating temperature of 300 °C for various ethanol concentrations.^[64] It was shown that the sensitivity improved as the gas concentration increased. The gas sensor made of nanoplates with 500–1000 nm in lateral size and 50 nm thickness annealed at 450 °C had the best alcohol sensing performance, due to the high crystallinity of the nanoplates. The sensor maintained the initial response upon seven successive tests to 100 ppm of ethanol, showing good stability and reproducibility. The plate-like morphology and high crystallinity enable effective adsorption and rapid diffusion of the ethanol molecules. WO₃ platelets, produced by laser-assisted synthesis and with 70 nm thickness, were tested as ethanol sensors both in their pristine form and decorated with 8 nm Au nanoparticles.^[65] The pure platelet sensor reached the

Review

maximum response (current ratios through the sensor with and without the target gas) of 28 at 390 °C for 100 ppm of ethanol. With the added Au particles, the optimal temperature was lowered to 300 °C, with the 3.5-fold increase of the response value. The difference is attributed to the increased thickness of the electron-depletion layer, whereby Au nanoparticles accelerate the reaction between the ethanol molecules and adsorb oxygen ions.

Nanoplatelets of monoclinic WO₃ with 70–100 nm in lateral size and 30 nm of thickness were investigated as acetone and ammonia sensors due to their high crystallinity and smooth 2D surface.^[24] These nanoplatelets do not have oxygen vacancies, but an abundance of surface chemisorbed oxygen. Those properties make them excellent gas sensors towards acetone at 300 °C, with response and recovery times of 3 s and 7 s, respectively, at 10 ppm of acetone. Additionally, this sensor showed a wide response range (1–500 ppm), detection concentration as low as 1 ppm and good selectivity and stability. It was shown that active O⁻ plays a leading sensing role for acetone. In the case of ammonia sensing, the optimal operating temperature was found to be 140 °C, with the response and recovery times of 39 s and 10 s, respectively; response region of 5–500 ppm and high selectivity. The sensing mechanism and the sensor response are shown in Figure 3 b).

3.2 Electrical Properties: Conductivity and 2D Photodetectors

The presence of the free electrons in the conduction band is the dominant factor in the electrical conductivity of these materials. These free electrons mainly come from CS planes, PC structures, oxygen vacancies, and other defects.^[66] Even in the case of a single crystal, the electrical conductivity can span five orders of magnitude (10⁻⁴–10 Scm⁻¹), depending on the stoichiometry,^[67] with the charge carrier concentrations spanning the similar range (10¹⁷–10²² cm⁻³).^[68] The amount of oxygen vacancies and the stoichiometry strongly depend on synthesis conditions and structural factors, which heavily influence the conductivity. This makes tungsten (sub)oxides interesting in terms of tailoring the material properties for specific electrical applications.

Bulk monoclinic WO₃ is a wide bandgap n-type semiconductor.^[1a,69] The n-type semiconductor properties stem from oxygen vacancy-type defects. Bandgap corresponds to the difference between the top of the valence band (filled O 2p orbitals) and the bottom of the conduction band (empty W 5d orbitals), and is typically reported as 2.62 eV.^[70] Bulk, stoichiometric WO₃ is therefore transparent in the visible wavelength range. Another thing to consider when designing optical devices based on WO₃, is its large refractive index of up to 2.5.^[71] On the other hand, oxygen vacancies due to true, point-like defects in WO₃, are major contributors in the improved photocurrent density.^[72] In n-type metal oxides, these oxygen vacancies act as shallow donors. These electrons may fill the acceptor states below the conduction band minimum,

making inter-bandgap states. If these shallow defect states remain unfilled, they can act as electron traps, resulting in the increased photoelectron lifetimes.^[73] Due to the quantum confinement effects, 2D-WO₃ have a larger bandgap and more positive conduction and valence band edges.^[25,74] For nanostructured semiconductors, the bandgap generally increases with the decrease in size,^[75] resulting in the blueshift of the optical absorption band edge. It should be pointed out that the quantum confinement effect can occur in two different regimes.^[76] In the strong regime, the size of the material has to be much smaller than its Bohr radius, which is estimated as 3 nm for WO₃.^[77] The bandgap is significantly altered because the electron wavefunctions are perturbed directly. In the weak regime, when the crystallite size is larger than the Bohr radius, the bandgap energy changes are subtler, as the wavefunctions are indirectly perturbed. Therefore, the crystallite size plays an important role in bandgap engineering.

In bulk and in form of nanowires, WO₃ photodetectors showed a relatively slow response time and low on/off ratios.^[78] It is to be expected that 2D nanosheets have an improved performance.

50 nm layers thick WO₃ layers were deposited on a graphene back electrode (on a PET substrate), in order to engineer a transparent, flexible UV detector, as shown in Figure 4 a).^[74] These photodetectors were subsequently tested under 325 nm UV light or an alternating on and off UV source in 10 s intervals. The detector had a typical p-type Schottky contact barrier *I*-*V* response. The time responses are highly stable and reproducible, with no degradation after tens of on-

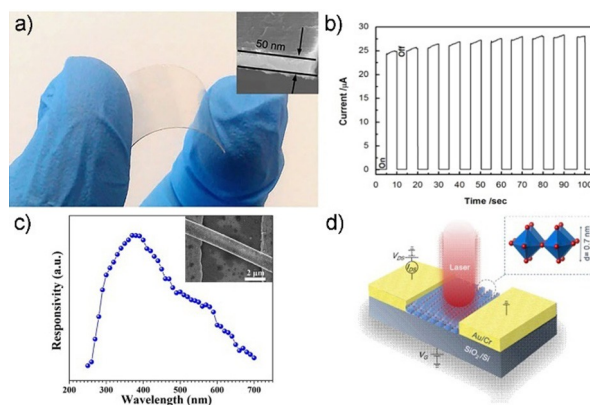


Figure 4. a) The fabricated flexible photodetector made of a WO₃ nanosheet on PET substrate (Reprinted from reference [74], with permission from Springer); b) The time-resolved photocurrent of the photodetector in response to light on/off at an irradiance of 131 mWcm⁻² with 365 nm light (Reprinted from reference [79], with permission from Elsevier); c) Spectroscopic photoresponse of the WO₃ nanobelt photodetector (shown in inset) measured at various wavelengths ranging from 250 to 700 nm at a bias of 1 mV. (Reprinted with permission from reference [80]. Copyright {2015} American Chemical Society); d) Three-dimensional schematic view of the monolayer WO₃ photodetector and the focused laser beam used to probe the device. (Reprinted from reference [82], with permission from Elsevier).

Review

off switching cycles. Interestingly, there was an increase in photocurrent with prolonged irradiation time, possibly due to its photochromic effect under UV radiation.^[74]

A 12 nm (approximately 16 molecular sheets) thick WO_3 nanosheets photodetector, with two Cr/Au electrodes, was irradiated with a 365 nm monochromatic light.^[79] This source was chosen as it is approximately at the position of the bandgap. The device exhibited a reversible on/off ratio of 2000, making it a high-quality photosensitive switch. The rise and the decay time were estimated to be 40 ms and 80 ms, respectively, which is much faster than that of the nanowires (20 s). The decay time was longer than the rise time, due to the presence of several recombination processes, such as surface and Auger recombination. Spectral responsivity, defined as the photocurrent generated per unit power of incident light on the effective area of a photodevice, was estimated as 293 AW^{-1} . The time-resolved photocurrent in response to on/off light is shown in Figure 4b).

Additionally, polycrystalline WO_3 200–300 nm thick nanobelts were successfully used as a building block of a UV photodetector.^[80] One individual belt consisted of dense nanoparticles of 20 nm in size. Using gold electrodes, this photodetector was assembled on a SiO_2/Si substrate and the photoresponse was recorded for the light excitation between 250 and 700 nm, as shown in Figure 4c), with the maximum sensitivity observed at 400 nm. The photoresponse has a slight drop for the wavelengths shorter than 400 nm, as explained by the enhanced absorption of the high-energy photons near the surface, while the increase in the longer wavelengths was attributed to the transition of the carriers from defect states to the conduction band.^[81] I - V curves recorded in dark and under illumination are nonlinear, indicating Schottky contact between the sample and the electrodes. The photoexcited currents were much greater than dark currents, with a photo-dark current ratio of 1000. The superior performance compared to monocrystalline WO_3 was attributed to the abundance of grains and boundaries that suppress the dark currents, and the increased photocurrent due to band-gap modulation.

Finally, a monolayer WO_3 , produced by atomic layer deposition on a SiO_2/Si wafer, as shown in in Figure 4d), was used for UV-A (315–400 nm) spectrum detection, which represents 95% of the UV radiation that reaches the Earth's surface.^[82] This detector was shown to have an extremely fast response time ($\leq 40 \mu\text{s}$, 400 times faster than in the case of WO_3 nanosheets^[79]), stability of more than 200 cycles and photoresponsivity of 0.33 AW^{-1} . This value is more than two orders of magnitude greater than for the previously reported WO_3 photodetectors, with the reduced thickness as the most important factor for such an improvement in performance. Additionally, the photodetector was tested under 320 nm light for different bias and back-gate voltages. In the dark, with no bias, a depletion sub-layer near the surface of the monolayer is formed, as the surrounding O_2 adsorbs on the material. With the applied bias, the current through the monolayer is low as the conductivity is low because of the depletion layer. When the device was put under the UV radiation, the photogenerated

holes moved to the surface and desorbed the oxygen, in turn decreasing the width of the depletion sublayer and increasing the number of free charge carriers. This whole process is sped up due to the small thickness.

Ultrathin (less than 10 nm) WO_{3-x} nanoflakes were intercalated with H^+ and tested as field-effect-transistor (FET) based devices.^[83] Zhuiykov *et al.* reported that devices prepared this way reach charge-carrier mobility of $319 \text{ cm}^2 \text{ V}^{-1} \text{ s}^{-2}$, comparable to those of MoS_2 and WS_2 , while for the nanoflakes before intercalation the mobility was $275 \text{ cm}^2 \text{ V}^{-1} \text{ s}^{-2}$. Both results are great improvements compared to the bulk WO_3 , that had the reported charge-carrier mobility of $12 \text{ cm}^2 \text{ V}^{-1} \text{ s}^{-2}$.^[83] By changing the thickness of the material (from 50 nm to 2.5 nm), the bandgap was modulated from 2.60 to 2.40 eV. It is believed that the intercalated H^+ ions interact with the corner-sharing oxygen atoms in the first monolayer, while the remaining ions get transferred deeper into the structure and repeat the same interaction. This fuels the formation of H_2O molecules that get released, leaving lone oxygen vacancies. The additional electron gets delocalized within the layers, giving rise to a mid-gap state. Furthermore, it was shown that H^+ intercalation reduces the bandgap from 2.6 to 2.5 eV.

3.3 Photocatalysis and Photoelectrochemical (PEC) Water Splitting

Pristine WO_3 does not have the photocatalytic activity high enough for practical use. Therefore, many approaches have been undertaken to improve the photocatalytic performance, with the most efficient ones being the introduction of the oxygen vacancies and/or using lower dimensional WO_{3-x} .

The photocatalytic reduction of CO_2 is an important route for its transformation to organic compounds as well as CO. Semiconductors have been used for photocatalysis with the absorption of a photon with the energy greater than its bandgap. This process induces an interband transition, whereby conduction band electrons and valence band holes are formed. The electrons and holes diffuse to the surface of the material, but only a fraction reaches it due to the recombination. In addition, the free charge carriers that reach the surface may be trapped before the interfacial charge transfer. Lastly, the photogenerated electrons reduce the CO_2 adsorbed on the catalyst surface into CO, HCOOH etc, while the holes oxidize H_2O to O_2 . One of the most important steps is the facilitation of the electron-hole separation, since the charge recombination happens on a much faster timescale (10^{-9} s) than the reaction process (10^{-3} – 10^{-8} s).^[84] Using the lower-dimensional WO_{3-x} can potentially improve the catalytic behaviour. Namely, in the case of bulk WO_3 , the photogenerated electrons in the conduction band have a lower, more positive, band-edge position.^[25] Therefore, in bulk, this material cannot be used for the reduction of CO_2 or H_2O . On the other hand, 5 nm thick WO_3 nanosheets could catalyse the photoreduction of CO_2 with H_2O into CH_4 . For such ultrathin material, the bandgap

Review

increased from 2.63 eV to 2.79 eV, while the conduction band edge moved from 0.05 eV to -0.42 eV (versus normal hydrogen electrode, NHE), becoming more negative than the CO_2/CH_4 redox potential at -0.24 eV.^[25–26] This demonstrates how a specific morphology can change the position of the conduction and/or the valence band, making the material a more suitable candidate for CO_2 reduction.

Liang *et al.* studied 5 nm thick WO_3 sheets' photocatalytic activity by degradation of methyl orange (MO) under simulated sunlight.^[3] They showed that the nanosheets have superior photocatalytic activity compared to nanoparticles or bulk material, due to their high specific surface area. Ultrathin (5 nm) WO_{3-x} nanosheets with abundant surface oxygen vacancies were also tested as PEC devices, by degradation of MO under visible light.^[14] After 90 min of irradiation, 70% of the solution was degraded, making them good candidates for this type of catalysis.

WO_{3-x} nanosheets with up to 300 nm lateral size and 15 nm thickness were tested as photocatalysts by using methylene blue (MB) and congo-red (CR) dyes under visible light irradiation.^[61] In 100 min, 99.5% of MB and 92% of CR was photodegraded by the nanosheets, a significant improvement compared with the nanorods (76% and 70%). The superior photocatalytic performance of the nanosheets is explained by the increase in the active surface, the smaller bandgap and oxygen deficiencies.

Both pristine WO_3 and 20–30 nm thick WO_3 nanosheets with oxygen vacancies were tested for their photocatalytic activity for the degradation of rhodamine B (RhB) under visible light irradiation.^[47a] While the pristine oxide decomposed only 9% of RhB after 320 min, WO_3 nanosheets with oxygen vacancies had increased photocatalytic efficiency of 77%. The latter sample had enhanced visible light absorption, and the plasmonic resonance with the peak at 800 nm. The oxygen vacancies act as electron donors and contribute to the enhanced donor density, increasing the charge transport and enhancing the photocatalytic activity.^[47a] Hydrothermally prepared WO_3 platelets with 50 nm thickness and up to 170 nm in lateral size were tested for the similar activity.^[85] It was shown that after 70 min of irradiation, the characteristic absorption peak of RhB almost disappeared, suggesting good photocatalytic activity.

Photoelectrochemical (PEC) water splitting is an increasingly popular technique for the efficient hydrogen generation. While the hydrogen is produced at the photocathode part of the PEC cell, photoanode material is responsible for the oxygen evolution reaction. Suitable photoanode candidates need to have appropriate band alignments (valence band more positive than water oxidation and conduction band more negative than hydrogen reduction) and to be absorbent in the visible light. WO_3 has a bandgap that can capture approximately 12% of the solar spectrum and absorb light up to 500 nm in the visible spectrum,^[86] while being chemically stable and environmentally friendly. In the case of the suboxides, the W^{5+} present in CS and PC structures as well as oxygen vacancy-induced electron traps can extend the photo-

electron lifetimes, improving their performance as photocathodes for water splitting.^[87] As a result, the photogenerated holes in the valence band have more time to move to the electrode and participate in the reaction. The W^{5+} and oxygen vacancies are not just active centres which capture charges to block recombination, they may also reduce the activation energy. On the other hand, samples with high number of defects may have decreased crystallinity. This can result in an overall decrease of photocurrents due to increase in scattering effects. Since the hole diffusion length in WO_3 is 150 nm,^[88] if the thickness of the samples is of an approximately similar size, it can play a significant role in decreasing charge carrier recombination. If this is fulfilled, the photogenerated holes can reach the surface more easily and participate in water splitting before recombining.

The free-standing pore-rich sub-4 nm thick WO_3 nanosheets were obtained by using a chemical topology transformation strategy.^[86] It was demonstrated that they have more photogenerated holes, shorter migration path and stronger oxidation ability than thicker samples. The measured photocurrent density of this sample is 2.14 mA cm^{-2} .

Mohamed *et al.* investigated both the stoichiometric and nonstoichiometric WO_3 , using an electrochemical method to study the nature of the defect states.^[72] Annealing the samples under different atmospheres resulted not only in different number, but in different nature of vacancies, making this a suitable approach to defect engineering. The highest photocurrent density was obtained on the nanoflakes annealed in air (1.3 mA cm^{-2}), with the optical band gap of 2.88 eV. It was demonstrated that the nonstoichiometric samples had higher photocurrents, indicating the presence of the shallow surface states, that feed the conduction band with electrons and form interband states. When the deep defect states become more dominant, they push the Fermi level away from the conduction band minimum, having damaging effect on the photocurrent. It can be concluded that the moderate concentration of oxygen vacancies results in appearance of W^{5+} shallow donor states that increase the photoactivity, while the deep trap W^{4+} states arise with the increase in oxygen vacancies, with the detrimental effect on photocurrent. This subtle interplay explains the contradictory results for the same material prepared under different conditions.

Soltani *et al.* designed 50 nm thick highly porous WO_{3-x} nanoplates with dual oxygen and tungsten vacancies for PEC water splitting.^[87] The number of oxygen vacancies and the film design were optimised to provide a large surface area for efficient charge collecting, which led to a photocurrent density of 4.12 mA cm^{-2} at 1.6 V vs Ag/AgCl. The stability time was reported as 1 h.

4. Summary and Outlook

In this review, an overview of the recent progress in the preparation of quasi-two-dimensional tungsten (sub)oxides was discussed. In recent years, a wide range of techniques

were developed to synthesize such materials. To a certain degree, the crystal phase, morphology and stoichiometry can be controlled but there is still room for improvement. For example, as discussed above, different facets have unique physical and chemical properties, which can be exploited in a wide range of chemical reactions and sensing devices. As of now, only a few 2D-WO₃ nanomaterials were synthesized with the certain facets exposed intentionally. Although the majority of the tungsten oxide nanomaterials appears in one form of the WO₃ crystal structure, substoichiometric tungsten oxides (WO_{3-x}) show a great variety of structures. Furthermore, they hold great promise due to their W⁵⁺ states that act as electron donors. By varying the stoichiometry of WO_{3-x} or the number of oxygen vacancies on the surface of tungsten (sub)oxides, their electrical and optical properties can be tuned for specific devices and chemical reactions.

It has to be pointed out that in the majority of publications, the material's reported stoichiometry was determined exclusively from XRD measurements, which is not a suitable method as the differences between the WO_{3-x} phases are too small to be unambiguously detected. Furthermore, it should be emphasized that the WO_{3-x} materials containing CS and PC structures should not be interchanged with materials with surface oxygen vacancies. Although individual oxygen vacancies can be produced, in order to minimize the surface energy, PC structures are formed while single CS planes appear when the material is further reduced. It would be beneficial if the reports on tungsten suboxide materials contained a thorough examination with HRTEM and electron diffraction techniques in order to determine the true nature and structure of oxygen vacancies. Only when this is achieved, further spectroscopic methods, such as Raman spectroscopy and optical measurements, can be utilized properly.

When it comes to potential applications, three of the most important factors that are responsible for the performance are the sample thickness, stoichiometry, and the oxygen vacancies. While the nanostructured suboxides in the shape of nanorods, nanowires and various other types of nanoparticles have been under numerous application-based studies, the similar research for their 2D counterparts is still in its infancy. For example, their charge-carrier densities are comparable to those of transition metal dichalcogenides, but the amount of reports of FETs based on these suboxides has been incomparably small. The control of the thickness, stoichiometry, and the introduction of the oxygen vacancies can be used as general strategies for increasing the electrical conductivity and photocatalytic activity. One of the major challenges could be the quantification and the effect on the crystal structure of the oxygen vacancies, and the deep understanding of their effect on optical and electronic properties, and the resulting performance in various applications.

Acknowledgements

This work was financially supported by the Slovenian Research Agency grant P1-0099. B. V. acknowledges funding provided by the Institute of Physics Belgrade through the grant by the Ministry of Education, Science, and Technological Development of the Republic of Serbia and Center for Solid State Physics and New Materials.

References

- [1] a) C. G. Granqvist, *Sol. Energy Mater. Sol. Cells* **2000**, *60*, 201–262; b) H. Miyazaki, T. Ishigaki, T. Ota, *J. Mater. Sci. Res.* **2017**, *6*, 62–66.
- [2] Z. Hai, Z. Wei, C. Xue, H. Xu, F. Verpoort, *J. Mater. Chem. C* **2019**, *7*, 12968–12990.
- [3] Y. Liang, Y. Yang, C. Zou, K. Xu, X. Luo, T. Luo, J. Li, Q. Yang, P. Shi, C. Yuan, *J. Alloys Compd.* **2019**, *783*, 848–854.
- [4] S. S. Thind, X. Chang, J. S. Wentzell, A. Chen, *Electrochem. Commun.* **2016**, *67*, 1–5.
- [5] H. Zheng, J. Z. Ou, M. S. Strano, R. B. Kaner, A. Mitchell, K. Kalantar-zadeh, *Adv. Funct. Mater.* **2011**, *21*, 2175–2196.
- [6] a) T. Vogt, P. M. Woodward, B. A. Hunter, *J. Solid State Chem.* **1999**, *144*, 209–215; b) B. Gerand, G. Nowogrocki, J. Guenot, M. Figlarz, *J. Solid State Chem.* **1979**, *29*, 429–434.
- [7] M. Boulova, G. Lucazeau, *J. Solid State Chem.* **2002**, *167*, 425–434.
- [8] Z. Zhang, X. Hao, S. Hao, X. Yu, Y. Wang, J. Li, *Molecular Catalysis* **2021**, *503*, 111427.
- [9] V. Hariharan, B. Gnanavel, R. Sathiyapriya, V. Aroulmoji, *Int J Adv Sci Eng Inf Technol.* **2019**, *5*, 1163–1168.
- [10] L. Pirker, B. Višić, S. D. Škapin, G. Dražić, J. Kovač, M. Remškar, *Nanoscale* **2020**, *12*, 15102–15114.
- [11] H. G. Choi, Y. H. Jung, D. K. Kim, *J. Am. Ceram. Soc.* **2005**, *88*, 1684–1686.
- [12] A. Wolcott, T. R. Kuykendall, W. Chen, S. Chen, J. Z. Zhang, *J. Phys. Chem. B* **2006**, *110*, 25288–25296.
- [13] D. Chen, L. Gao, A. Yasumori, K. Kuroda, Y. Sugahara, *Small* **2008**, *4*, 1813–1822.
- [14] X. Zhou, X. Zheng, B. Yan, T. Xu, Q. Xu, *Appl. Surf. Sci.* **2017**, *400*, 57–63.
- [15] A. Azam, J. Kim, J. Park, T. G. Novak, A. P. Tiwari, S. H. Song, B. Kim, S. Jeon, *Nano Lett.* **2018**, *18*, 5646–5651.
- [16] K. D. McDonald, B. M. Bartlett, *RSC Adv.* **2019**, *9*, 28688–28694.
- [17] H. Zhang, G. Duan, Y. Li, X. Xu, Z. Dai, W. Cai, *Cryst. Growth Des.* **2012**, *12*, 2646–2652.
- [18] W. Li, P. Da, Y. Zhang, Y. Wang, X. Lin, X. Gong, G. Zheng, *ACS Nano* **2014**, *8*, 11770–11777.
- [19] Y. Oaki, H. Imai, *Adv. Mater.* **2006**, *18*, 1807–1811.
- [20] N. Dirany, M. Arab, V. Madigou, C. Leroux, J. Gavarrri, *RSC Adv.* **2016**, *6*, 69615–69626.
- [21] X. Han, X. Han, L. Li, C. Wang, *New J. Chem.* **2012**, *36*, 2205–2208.
- [22] Z. Fang, S. Jiao, B. Wang, W. Yin, S. Liu, R. Gao, Z. Liu, G. Pang, S. Feng, *Mater. Today* **2017**, *6*, 146–153.
- [23] J. Besnardiere, B. Ma, A. Torres-Pardo, G. Wallez, H. Kabbour, J. M. González-Calbet, H. J. Von Bardeleben, B. Fleury, V. Buissette, C. Sanchez, *Nat. Commun.* **2019**, *10*, 1–9.

- [24] G. Liu, L. Zhu, Y. Yu, M. Qiu, H. Gao, D. Chen, *J. Alloys Compd.* **2021**, 858, 157638.
- [25] X. Chen, Y. Zhou, Q. Liu, Z. Li, J. Liu, Z. Zou, *ACS Appl. Mater. Interfaces* **2012**, 4, 3372–3377.
- [26] a) Y. P. Xie, G. Liu, L. Yin, H.-M. Cheng, *J. Mater. Chem.* **2012**, 22, 6746–6751; b) N. Zhang, C. Chen, Z. Mei, X. Liu, X. Qu, Y. Li, S. Li, W. Qi, Y. Zhang, J. Ye, *ACS Appl. Mater. Interfaces* **2016**, 8, 10367–10374.
- [27] M. Remškar, J. Kovac, M. Viršek, M. Mrak, A. Jesih, A. Seabaugh, *Adv. Funct. Mater.* **2007**, 17, 1974–1978.
- [28] a) J. Allpress, R. Tilley, M. Sienko, *J. Solid State Chem.* **1971**, 3, 440–451; b) S. Iijima, *J. Solid State Chem.* **1975**, 14, 52–65.
- [29] W. Merchan-Merchan, M. F. Farahani, Z. Moorhead-Rosenberg, *Micron* **2014**, 57, 23–30.
- [30] a) S. Lee, Y.-W. Lee, D.-H. Kwak, M.-C. Kim, J.-Y. Lee, D.-M. Kim, K.-W. Park, *Ceram. Int.* **2015**, 41, 4989–4995; b) B. Wang, X. Zhong, C. He, B. Zhang, U. Cvelbar, K. Ostrikov, *J. Alloys Compd.* **2021**, 854, 157249; c) B. Wang, X. Zhong, C. He, B. Zhang, U. Cvelbar, K. Ostrikov, *Mater. Chem. Phys.* **2021**, 262, 124311.
- [31] a) M. Mattinen, J.-L. Wree, N. Stegmann, E. Ciftiyurek, M. E. Achhab, P. J. King, K. Mizohata, J. Räisänen, K. D. Schierbaum, A. Devi, *Chem. Mater.* **2018**, 30, 8690–8701; b) N. Doudin, D. Kuhness, M. Blatnik, G. Barcaro, F. Negreiros, L. Sementa, A. Fortunelli, S. Surnev, F. Netzer, *J. Phys. Chem. C* **2016**, 120, 28682–28693.
- [32] M. B. Johansson, B. Zietz, G. A. Niklasson, L. Österlund, *J. Appl. Phys.* **2014**, 115, 213510.
- [33] M. Dobson, R. Tilley, *Acta Crystallogr. Sect. B* **1988**, 44, 474–480.
- [34] S. Heo, J. Kim, G. K. Ong, D. J. Milliron, *Nano Lett.* **2017**, 17, 5756–5761.
- [35] L. Wen, L. Chen, S. Zheng, J. Zeng, G. Duan, Y. Wang, G. Wang, Z. Chai, Z. Li, M. Gao, *Adv. Mater.* **2016**, 28, 5072–5079.
- [36] a) P. Labbe, in *Key Engineering Materials, Vol. 68*, Trans Tech Publ, **1992**, p. 293; b) R. Tilley, *J. Solid State Chem.* **1976**, 19, 53–62.
- [37] Y.-J. Lee, T. Lee, A. Soon, *Chem. Mater.* **2019**, 31, 4282–4290.
- [38] A. Magnéli, *Acta Crystallogr.* **1953**, 6, 495–500.
- [39] L. Bursill, B. Hyde, *J. Solid State Chem.* **1972**, 4, 430–446.
- [40] M. Lundberg, M. Sundberg, A. Magnéli, *J. Solid State Chem.* **1982**, 44, 32–40.
- [41] a) A. Magneli, *Arkiv Kemi* **1949**, 1, 223–230; b) R. Pickering, R. Tilley, *J. Solid State Chem.* **1976**, 16, 247–255.
- [42] T. Miyano, M. Iwanishi, C. Kaito, M. Shiojiri, *Japanese J. Appl. Phys.* **1983**, 22, 863.
- [43] J. Meng, Z. Lan, I. E. Castelli, K. Zheng, *J. Phys. Chem. C* **2021**, 125, 8456–8460.
- [44] Z. Zhao, Y. Bai, W. Ning, J. Fan, Z. Gu, H. Chang, S. Yin, *Appl. Surf. Sci.* **2019**, 471, 537–544.
- [45] W. Zhang, P. Xu, Y. Shen, J. Feng, Z. Liu, G. Cai, X. Yang, R. Guan, L. Su, L. Yue, *J. Environ. Chem. Eng.* **2021**, 9 (6), 106493.
- [46] L. Pirker, B. Višić, J. Kovač, S. D. Škapin, M. Remškar, *Nanomaterials* **2021**, 11, 1985.
- [47] a) S. Chen, Y. Xiao, W. Xie, Y. Wang, Z. Hu, W. Zhang, H. Zhao, *Nanomaterials* **2018**, 8, 553; b) X. Ming, A. Guo, G. Wang, X. Wang, *Sol. Energy Mater. Sol. Cells* **2018**, 185, 333–341.
- [48] F. Negreiros, T. Obermüller, M. Blatnik, M. Mohammadi, A. Fortunelli, F. Netzer, S. Surnev, *J. Phys. Chem. C* **2019**, 123, 27584–27593.
- [49] A. Mohamedkhair, Q. Drmosh, M. Qamar, Z. Yamani, *Catalysts* **2020**, 10, 526.
- [50] a) Z. Hai, M. K. Akbari, Z. Wei, C. Xue, H. Xu, J. Hu, S. Zhuiykov, *Electrochim. Acta* **2017**, 246, 625–633; b) S. Balasubramanyam, A. Sharma, V. Vandalon, H. C. Knoops, W. M. Kessels, A. A. Bol, *J. Vac. Sci. Technol.* **2018**, 36, 01B103.
- [51] S. Yu, Y. Ling, J. Zhang, F. Qin, Z. Zhang, *Int. J. Hydrogen Energy* **2017**, 42, 20879–20887.
- [52] Y. Li, K. Chang, H. Tang, B. Li, Y. Qin, Y. Hou, Z. Chang, *Electrochim. Acta* **2019**, 298, 640–649.
- [53] K. Pan, K. Shan, S. Wei, K. Li, J. Zhu, S. H. Siyal, H.-H. Wu, *Compos. Commun.* **2019**, 16, 106–110.
- [54] E. K. Salje, *Condens. Matter* **2020**, 5, 32.
- [55] Z. Wang, D. Wang, J. Sun, *Sens. Actuators B* **2017**, 245, 828–834.
- [56] W. Zhu, F. Huang, E. Chen, Q. Wu, J. Xu, C. Lu, Y. Wang, *Che. Asian J.* **2017**, 12, 524–529.
- [57] A. Dey, *Mater. Sci. Eng. B* **2018**, 229, 206–217.
- [58] M. Guarnieri, J. R. Balmes, *The Lancet* **2014**, 383, 1581–1592.
- [59] C. Cantalini, L. Lozzi, M. Passacantando, S. Santucci, *IEEE Sens. J.* **2003**, 3, 171–179.
- [60] H. Khan, A. Zavabeti, Y. Wang, C. J. Harrison, B. J. Carey, M. Mohiuddin, A. F. Chrimes, I. A. De Castro, B. Y. Zhang, Y. M. Sabri, *Nanoscale* **2017**, 9, 19162–19175.
- [61] M. Parthibavarman, M. Karthik, S. Prabhakaran, *Vacuum* **2018**, 155, 224–232.
- [62] M. B. Rahmani, M. H. Yaacob, Y. M. Sabri, *Sens. Actuators B* **2017**, 251, 57–64.
- [63] M. Horprathum, T. Srichaiyaperk, B. Samransuksamer, A. Wisitsoraat, P. Eiamchai, S. Limwichean, C. Chananonawathorn, K. Aiempnanakit, N. Nuntawong, V. Patthanasettakul, *ACS Appl. Mater. Interfaces* **2014**, 6, 22051–22060.
- [64] J. Ma, J. Zhang, S. Wang, T. Wang, J. Lian, X. Duan, W. Zheng, *J. Phys. Chem. C* **2011**, 115, 18157–18163.
- [65] E. Dai, S. Wu, Y. Ye, Y. Cai, J. Liu, C. Liang, *J. Colloid Interface Sci.* **2018**, 514, 165–171.
- [66] K. Aguir, C. Lemire, D. Lollman, *Sens. Actuators B* **2002**, 84, 1–5.
- [67] V. Makarov, M. Trontelj, *J. Eur. Ceram. Soc.* **1996**, 16, 791–794.
- [68] a) X. Liu, Y. He, S. Wang, Q. Zhang, M. Song, *Int. J. Refract. Met. Hard M.* **2012**, 34, 47–52; b) K. Patel, C. Panchal, V. Kheraj, M. Desai, *Mater. Chem. Phys.* **2009**, 114, 475–478; c) M. Regragui, V. Jousseau, M. Addou, A. Outzourhit, J. Bernede, B. E. Idrissi, *Thin Solid Films* **2001**, 397, 238–243.
- [69] P. González-Borrero, F. Sato, A. Medina, M. L. Baesso, A. C. Bento, G. Baldissera, C. Persson, G. A. Niklasson, C. G. Granqvist, A. Ferreira da Silva, *Appl. Phys. Lett.* **2010**, 96, 061909.
- [70] M. Gillet, K. Aguir, C. Lemire, E. Gillet, K. Schierbaum, *Thin Solid Films* **2004**, 467, 239–246.
- [71] D. Davazoglou, A. Donnadieu, *Thin Solid Films* **1987**, 147, 131–142.
- [72] A. M. Mohamed, A. W. Amer, S. Y. AlQaradawi, N. K. Allam, *Phys. Chem. Chem. Phys.* **2016**, 18, 22217–22223.
- [73] L. J. Antila, M. J. Heikkilä, V. Mäkinen, N. Humalämäki, M. Laitinen, V. Linko, P. Jalkanen, J. Toppari, V. Aumanen, M. Kemell, *J. Phys. Chem. C* **2011**, 115, 16720–16729.
- [74] Z. Sun, T. Liao, Y. Dou, S. M. Hwang, M.-S. Park, L. Jiang, J. H. Kim, S. X. Dou, *Nat. Commun.* **2014**, 5, 1–9.
- [75] S. Gullapalli, R. Vemuri, C. Ramana, *Appl. Phys. Lett.* **2010**, 96, 171903.
- [76] A. D. Yoffe, *Adv. Phys.* **1993**, 42, 173–266.
- [77] R. A. May, L. Kondrachova, B. P. Hahn, K. J. Stevenson, *J. Phys. Chem. C* **2007**, 111, 18251–18257.
- [78] L. Li, Y. Zhang, X. Fang, T. Zhai, M. Liao, X. Sun, Y. Koide, Y. Bando, D. Golberg, *J. Mater. Chem.* **2011**, 21, 6525–6530.
- [79] J. Liu, M. Zhong, J. Li, A. Pan, X. Zhu, *Mater. Lett.* **2015**, 148, 184–187.

- [80] Z. He, Q. Liu, H. Hou, F. Gao, B. Tang, W. Yang, *ACS Appl. Mater. Interfaces* **2015**, *7*, 10878–10885.
- [81] J. Jie, W. Zhang, Y. Jiang, X. Meng, Y. Li, S. Lee, *Nano Lett.* **2006**, *6*, 1887–1892.
- [82] Z. Hai, M. K. Akbari, C. Xue, H. Xu, L. Hyde, S. Zhuiykov, *Appl. Surf. Sci.* **2017**, *405*, 169–177.
- [83] S. Zhuiykov, E. Kats, B. Carey, S. Balendhran, *Nanoscale* **2014**, *6*, 15029–15036.
- [84] M. R. Hoffmann, S. T. Martin, W. Choi, D. W. Bahnemann, *Chem. Rev.* **1995**, *95*, 69–96.
- [85] H. Zhang, J. Yang, D. Li, W. Guo, Q. Qin, L. Zhu, W. Zheng, *Appl. Surf. Sci.* **2014**, *305*, 274–280.
- [86] Y. Liu, L. Liang, C. Xiao, X. Hua, Z. Li, B. Pan, Y. Xie, *Adv. Energy Mater.* **2016**, *6*, 1600437.
- [87] T. Soltani, A. Tayyebi, H. Hong, M. H. Mirfasihi, B.-K. Lee, *Sol. Energy Mater. Sol. Cells* **2019**, *191*, 39–49.
- [88] R. Solarska, R. Jurczakowski, J. Augustynski, *Nanoscale* **2012**, *4*, 1553–1556.

Manuscript received: July 14, 2021

Revised manuscript received: October 25, 2021

Version of record online: November 23, 2021

Dynamical Nature of Exciton-Polariton Coupling in WS₂ Nanoparticles

Sudarson Sekhar Sinha,^[a] Bojana Višić,^[b, c] Archana Byregowda,^[d] and Lena Yadgarov^{*,[d]}

Abstract: Semiconducting transition metal dichalcogenides can be synthesized in a wide range of structures and geometries, including closed cage nanostructures, such as nanotubes or fullerene-like nanoparticles (NSs). The latter is especially intriguing due to the stability, enhanced light-matter interactions, and ability to sustain exciton-polaritons (EPs) in ambient conditions, i. e., strong coupling of excitonic resonances to the optical cavity. Here we investigate the dynamics of EPs formation in WS₂ NPs in the time domain using femtosecond transient extinction spectroscopy. We develop a gamut of analytical methods and models with time-dependent parameters to extract the underlying non-equilibrium dynamics of EPs formation. We find that the

formation of EPs in WS₂ NPs is not instantaneous but a gradual process that occurs only after several picoseconds. Specifically, for the short delay times, the light-matter interaction is guided by excitonic absorption, whereas for the long delay times, the process is controlled by polaritonic scattering. We discover that the coupling strength is a time-dependent entity and not a constant as is usually defined. Namely, there is a nonlinear coupling between excitonic and external modes and a notable transition from weak to strong coupling limit. Our results show that the time-dependent phenomenological dynamical model quantitatively reproduces the nonlinear dynamical coupling as well as the effects of the pump fluence on the coupling strength.

Keywords: 2D materials · inorganic fullerene like nanoparticles · polaritons · excitons · femtosecond spectroscopy · strong coupling

Introduction

Extensive research efforts have been devoted to understanding and utilizing the unique optical properties of semiconductor nanostructures (NSs). Much effort has been placed on their ability to confine light into nanoscale dimensions,^[1] which subsequently increases the field strength. In turn, this effect enhances light-matter interactions and leads to nonlinearities, large photonic forces, and enhanced emission and absorption probabilities.^[2] In general, semiconductor NSs support cavity modes if their scales are comparable to the wavelength of light in vacuum. However, semiconductors with a refractive index that is much larger than that of their surroundings can also efficiently confine light into subwavelength dimensions.^[1b,2-3] The cavity modes are generated by the confinement of the light into small volumes and the Fabry-Perot recirculation.^[1b] The resonance conditions in nanocavities depend on the refractive index of the medium and the semiconductor, the nanostructure's dimensions, and geometry, as well as the polarization of the optical field. Together with their ability to sustain cavity-mode resonances, semiconductor NSs can generate excitons and can thus create quasi-particles known as exciton-polaritons (EPs).^[4] EPs are formed as a result of strong coupling between the excitons and the optical modes of the nanocavity (photon).

The interactions between excitons and cavity mode resonances are usually studied in the weak and strong coupling regimes. The energy spectrum of the coupled systems is modified such that the frequencies of the new modes are different from the original oscillator modes. The frequencies

shift or the spectral change depends on the strength of coupling.^[5] Typically, the weak coupling manifests itself as a narrow asymmetric dip and a negligible shift at the resonance frequency of the uncoupled oscillators.^[5] Under the weak coupling regime, the energy transfer rate between the two modes is lower than the relaxation rate of the system.^[6]

In the strong coupling regime, the interaction between the modes is strong enough and significantly modifies the energy levels. Strong coupling induces a significant spectral shift of

- [a] S. S. Sinha
Department of Materials and Interfaces, Weizmann Institute of Science, Rehovot, 7610001 Israel
- [b] B. Višić
Institute of Physics Belgrade, University of Belgrade, Pregrevice 118, 11080 Belgrade, Serbia
- [c] B. Višić
Solid State Physics Department, Jozef Stefan Institute, Jamova cesta 39, 1000 Ljubljana, Slovenia
- [d] A. Byregowda, L. Yadgarov
The Department Chemical Engineering, Ariel University, Ramat HaGolan St 65, 4077625 Ariel
E-mail: lenay@ariel.ac.il

Supporting information for this article is available on the WWW under <https://doi.org/10.1002/ijch.202100128>

© 2022 The Authors. *Israel Journal of Chemistry* published by Wiley-VCH GmbH. This is an open access article under the terms of the Creative Commons Attribution Non-Commercial NoDerivs License, which permits use and distribution in any medium, provided the original work is properly cited, the use is non-commercial and no modifications or adaptations are made.

Research Article

the resonances and manifests itself as well-separated peaks in the energy spectrum. Here, the new hybridized energies correspond to hybrids of the original modes of the interacting oscillators.^[5,7] The strong interaction between the coupled modes leads to an ultrafast oscillation between the two excited states.^[6b] The period of this oscillation is known as the Rabi oscillation period and should be much faster than the decoherence time of the excitation.^[8] The spectral splitting induced by the strong coupling is inferred as Rabi energy splitting.^[9] The hybrid nature of EPs opens possibilities for applications associated with information transfer, photonic and quantum technologies, and more.^[10]

Owing to their sizable bandgaps, strongly bound excitons, and high oscillator strength, the transition metal dichalcogenides (TMDs) are a promising platform to explore EP formation dynamics. Layered TMDs compounds are two-dimensional (2D) materials and have been studied intensively for a decade in the context of electrical, optical, and mechanical applications.^[11] The lattice of layered TMDs materials, e.g., MoS₂, consists of a 2D S–M–S sandwich structure, where M is the transition metal atom that binds to six chalcogen (S=S, Se or Te) atoms via strong covalent bonds. The MS₂ (M=Mo, W) layers are stacked together by weak van der Waals (vdW) forces.^[12] MS₂ exhibits a bandgap in the visible range, rendering it suitable for exploitation in solar cells, photodegradation of toxic materials, photovoltaics, and numerous other electronic applications. The indirect bandgap of bulk and multilayer MS₂ transforms into a direct bandgap in a single-layer material.^[12d] The properties of 2D-TMD semiconductors can be engineered through mechanical or structural changes. For instance, due to coupling between their mechanical and electrical properties,^[13] the electronic structures can be altered by introducing curvature to the 2D topology.^[14]

MS₂-type TMD materials feature A, B, and C exciton transitions in the visible light range. The excitonic transitions arise from the interlayer interactions and spin-orbit splitting, where the magnitude of the A–B splitting is independent of the number of layers (down to a few layers).^[15] Due to their sizable bandgaps, strongly bound excitons, and high oscillator strength, these materials can sustain stable polaritons under ambient conditions. Namely, the MS₂-type TMDs can trap optical cavity modes, resulting in a strong interaction of photonic modes and the excitons. Indeed, it was shown that MS₂ embedded in microcavities exhibited signatures of strong exciton-polariton coupling.^[16] The strong coupling in the Fabry-Perot microcavity configuration was observed for monolayer^[17] and multilayer systems.^[12a,16b,17–18] As these strong light-matter interactions occur at ambient conditions, TMDs polaritonic materials generate a considerable interest in the field of nanodevices.^[12c,19]

The fact that EP can exist in multilayered TMD materials under ambient conditions inspired a renewed interest in the optical properties of MX₂ closed-cage layered nanostructures, such as nanotubes (NTs) and fullerene-like nanoparticles (NPs). Nanotubes and fullerene-like nanoparticles have been

synthesized in substantial amounts and their properties were widely studied.^[20] These studies resulted in numerous applications, and led to their rapid commercialization.^[21] The multi-wall closed-cage MX₂ nanostructures preserve the semiconductor nature of their bulk counterparts and are usually indirect bandgap semiconductors.^[22] Using tight-binding model calculations, it was shown that the zig-zag (n,0) single-wall NTs exhibit a direct bandgap whereas the lowest transition of armchair (n,n) NTs exhibits indirect bandgap.^[23] The experimental results indicate that the bandgap of these closed-cage nanomaterials shrinks with the decrease in diameter.^[24] Moreover, due to the chiral nature of the NTs, the quasi 1D superconductivity, Little-Parks oscillations, photovoltaic effects, and the ambipolar transition behavior in ionic liquid and strong electroluminescence is observed.^[25]

Interestingly, MoS₂ and WS₂ closed-cage nanomaterials are emerged to be unique systems that support polaritonic features even when dispersed in aqueous solutions without an external cavity.^[12a,26] Moreover, the strong-coupling effects in WS₂ nanotubes (NTs) exist even when dispersed in aqueous solutions, where EPs modes occur due to strong coupling between excitons and cavity modes confined in the nanotubes.^[12a,18] The use of such closed-cage nanostructures allows remarkable tunability of light-matter interactions, such that by varying the diameter of the NTs we can shift from pure excitonic to polaritonic features.^[18b]

Although light-matter interaction of bulk and single layers of MS₂ materials is studied intensively, their closed-caged counterparts have not been thoroughly explored yet. Notwithstanding, the study of excitons coupled with light in multilayered closed-cage 3D materials could provide broader perspectives for the fundamental properties of EPs in sub-wavelength dimensions. Their ability to sustain 3D cavity modes, stability and the lack of the dangling bonds can suppress exciton capture at non-radiative recombination centers. Moreover, WS₂ NPs are expected to serve as an extraordinary platform for applications and fundamental research in the field of TMDs polaritonics.

Here, we provide a time-dependent study of the coupling between exciton resonances and intrinsic optical cavity modes. We employ femtosecond (fs) broadband optical pump-probe spectroscopy to examine the response of WS₂ NPs in aqueous dispersion and explore time-dependent coupled states formation between exciton resonances and an intrinsic cavity mode. Using a simplistic comparison of the steady-state absorbance and extinction derivatives with the transient extinction spectra, we find that in the fs time-limit, the light-matter interaction is guided by the excitonic absorption, whereas at picoseconds (ps) time-delays, the process is controlled by polaritonic scattering. Moreover, by expressing the transient signals as the difference of the transmission with and without pump, we discover temporal transition from weak to strong coupling limit as the excited excitons relax into the coupled (polaritonic) state. Namely, we find that the formation of EPs in WS₂ NPs is not instantaneous but a gradual process that occurs only after several ps. Using these findings, we propose a model for

the time-dependent coupling of exciton and cavity modes with phenomenological dynamics. The temporal evolution of the model parameters clarifies the nonlinear dynamical coupling and the effects of the pump fluence on the coupling strength. The gamut of proposed models can hereafter be utilized to guide the experimental observation of exciton-polariton formation and coupling evolution dynamics. Moreover, the obtained results can be applied in the field of TMDs polaritonics for exploring genuinely unique physical scenarios and exploiting these new phenomena in technology in areas such as nanoscale lasing, quantum optics, and nanomanipulation.

Results and Discussion

The studied WS₂ fullerene-like nanoparticles consist of 20-40 concentric shells and span diameters from 30 to 100 nm.^[27] This somewhat high size distribution can be narrowed down using a simple dispersion-fractionation technique.^[18b] Figures 1a present the SEM and TEM images of such nanoparticles. The size and high degree of crystalline order of the NPs can be appreciated from these figures. The absorbance was measured using an integrating sphere which allows excluding the scattering contribution. The absorbance spectra exhibit distinct resonances at 630 nm and 530 nm (Figure 1b, **red line**) assigned to the A and B excitonic transitions, respectively.^[28] In contrast to the absorbance, the extinction spectra of the dispersed WS₂ NPs (Figure 1b, **black line**) introduce maxima at 680, 580, 510 nm, which are red-shifted compared to the A, B, and C excitonic transitions of the WS₂ NPs and the bulk.^[28–29] The extinction measurements are performed by a standard UV-Vis spectrophotometer, hence the spectra include absorbance and scattering features.^[30] The difference between absorbance and extinction spectra can be assigned to the scattering related phenomena – polaritons. It

was shown that WS₂ nanostructures with a diameter > 60 nm, sustain cavity modes that are strongly coupled to the A and B excitons and generate polaritonic modes.^[18a,b, 19b, 31] Thus it can be concluded that the unusual extinction spectrum of the dispersed WS₂ NP is of polaritonic nature.

To study the formation of exciton-polariton (EP) quasiparticles, the ultrafast relaxation dynamics of WS₂ NP were investigated using femtosecond pump-probe optical spectroscopy. Here, the electron system is driven out of the equilibrium by the femtosecond pump pulse. The ultrafast motion is then captured by a broadband probe pulse with delay. This setup is used to determine the relative change in transmittance ($\Delta T/T$) as a function of pump-probe delay and wavelength. The ultrafast transient response of the states at 97 mW of pump is shown in Figure 2. The main features obtained from the femtosecond $\Delta T/T$ spectra are the two photo-bleaching and photo-induced absorption peaks. Photo-bleach (PB) and photo-induced absorption (PA) peaks correspond to decreased and increased transmittance ($PB = -\Delta T/T$; $PA = \Delta T/T$), respectively. The $\Delta T/T$ spectra of WS₂ NP at the short delay (0.3 ps) show PB at 625 and 525 nm and PA at 662 and 550 nm, corresponding to A and B excitonic resonances.^[32] At longer delays, most features are already significantly shifted, thus excitons can no longer be considered as the primary photoexcitation species. Specifically, from short (0.3 ps) to long (100 ps) delays, there is a 13 nm blue shift in the PB and PA states, i.e., the PA and PB shifted from 662 to 649 nm and 625 to 612 nm, respectively. (Figure S1, SI). The blue shift occurs mainly during the first 30 ps and is very high compared to the one reported for the few-layered WS₂ (~ 4 nm).^[32a] (Figure S2, SI) That considerable shift at shorter delay times, followed by decay at longer delays times, suggests two distinct processes and some coupling between them. Indeed, it was confirmed before that excitons in few-layered WS₂ are the primary photoexcitation species, dissociating into charge pairs with a time constant of ~1.3 ps.^[32a]

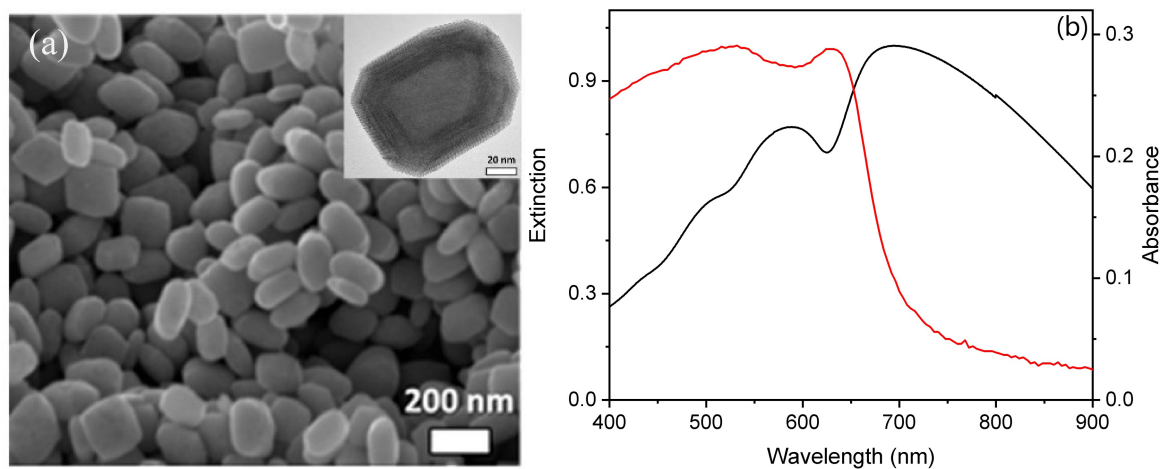


Figure 1. (a) SEM image of WS₂ NP; (inset) TEM image of WS₂ NP (b) extinction (black line) and absorbance (red line) spectra of the dispersed WS₂ NP.

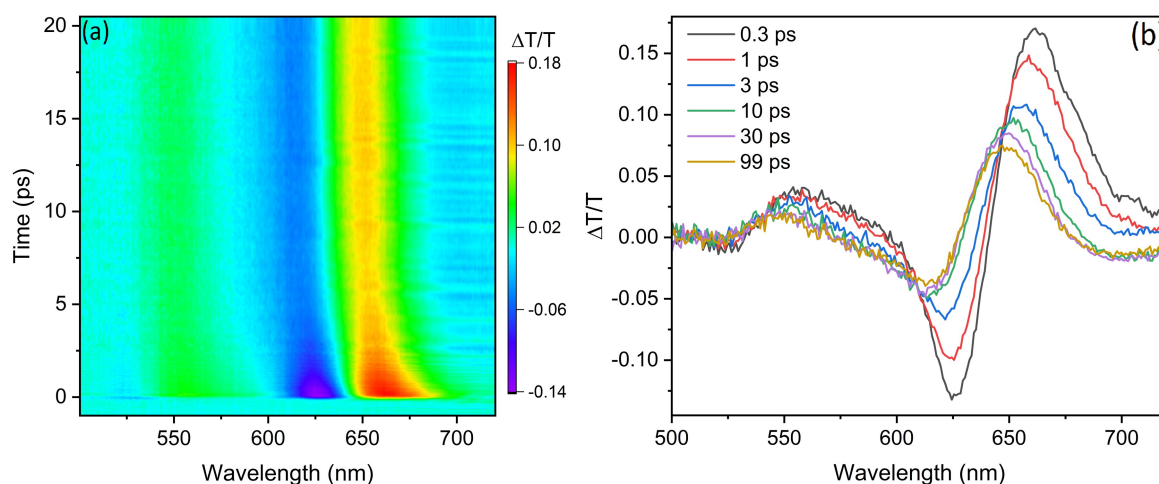


Figure 2. (a) Transient transmission trace ($\frac{\Delta T}{T}$) of WS₂ NPs for 97uW pump power. (b) Temporal evolution of transient spectra ($\frac{\Delta T}{T}$) at different pump-probe delay. Note the shift in photo-absorption and photo-bleach states in exciton (625 nm and 663 nm) to polariton (616 nm and 650 nm) states.

Moreover, it was found that in WS₂ nanotubes, the exciton resonances shift on the femto- and picosecond time scales due to the many-body effects of the photogenerated charge carriers and their population dynamics.^[18a] Generally, it was established that in WS₂ and MoS₂ nanotubes the transient spectra are dominated by the coupling of the exciton resonances to the cavity mode resonances.^[18a,c] In another work, it was shown that, while WS₂ nanotubes of an average diameter > 80 nm support polaritonic modes, the extinction of nanotubes with smaller diameter controlled mainly by excitonic features. [ref. Shina size] Note that the influence of the size distribution on the polariton dynamics is not discussed here, and will be presented in the future work. As most of the electro-optical properties of WS₂ NPs are comparable to their nanotubes counterparts, the dynamics of NP with diameter > 80 nm are expected to be similar to the latter, i.e., dominated by strong coupling of exciton resonances to the cavity mode resonances.

To understand the coupling between exciton and polariton, it is necessary to observe the photophysical processes on different time scales. The transient absorption spectroscopy produces a dynamical differential absorption spectrum, and the PB and PA processes are the main observables. Generally, the energy of the PB/PA processes is constant in time, except when intermediate dynamical processes occur. These processes are usually manifested by a spectral shift of the PB/PA picks.^[33] Intriguingly, in the case of dispersed WS₂ NP, the short time spectra (~0.3 ps) are very different from the long time (~100 ps) differential absorption spectra. To elucidate this phenomenon, let us calculate the differential spectra using steady-state extinction and absorbance measurements by Eq. 1 and 2, respectively.

$$\frac{dT_A}{d\lambda} = d(10^{-A(\lambda)})/d\lambda = -T_A \frac{d\alpha_A}{d\lambda} \quad (1)$$

$$\frac{dT_E}{d\lambda} = d(10^{-\epsilon(\lambda)})/d\lambda = -T_E \frac{d\alpha_E}{d\lambda} \quad (2)$$

Here α_E and α_A correspond to the extinction and absorption coefficient at wavelength λ , respectively. The T_E and T_A are the transmittances in extinction and absorption measurements. Note that extinction coefficients contain scattering and absorbance contribution, whereas the absorption coefficient is a pure absorption process with no scattering. The comparison of the steady-state derivatives to $\Delta T/T$ spectra at short and long delay times (0.03 ps and 98.9 ps) to the absorption and extinction derivatives are presented in Figure 3. The PB and PA peak positions at the shortest delays correspond to the maxima and minima of the absorbance derivatives. (Figure 3a, Eq. 1) Generally, the ground state bleaching and its absorption are the dominant processes at instantaneous excitation ($t \sim 0$), so the derivative of absorbance coefficient and the $\Delta T/T_{(t=0)}$ are expected to match. Indeed, there is a good overlap between $dT_A/d\lambda$ and $\Delta T/T_{(t=0)}$ at 660 nm. The PA is red-shifted by 15 nm compared to $dT_A/d\lambda$ minima (~610 nm). This shift can be explained by the response of the excitons or non-thermal hot electrons to the higher polar excited state.^[32a,34] At the longest delay ($t = 98.9$ ps), the PB and PA peaks do not match with the $dT_A/d\lambda$ but almost completely overlap with the features of the extinction derivative, $dT_E/d\lambda$. (Figure 3b, Eq. 2) The extinction features of the dispersed WS₂ NP are governed by the polaritonic modes.^[18a,19b,31a,b] Thus the match between the extinction derivative and the $\Delta T/T$ ($t = 98.9$ ps) implies that the latter is dominated by the polaritonic states.^[18a,b] In over words, the formation of EPs in WS₂ NPs is not instantaneous but a gradual process that occurs only after several ps. Moreover, the PA and PB of the coupled states are considerably shifted compared to the excitonic features. Interestingly, the somewhat simplistic comparison of the

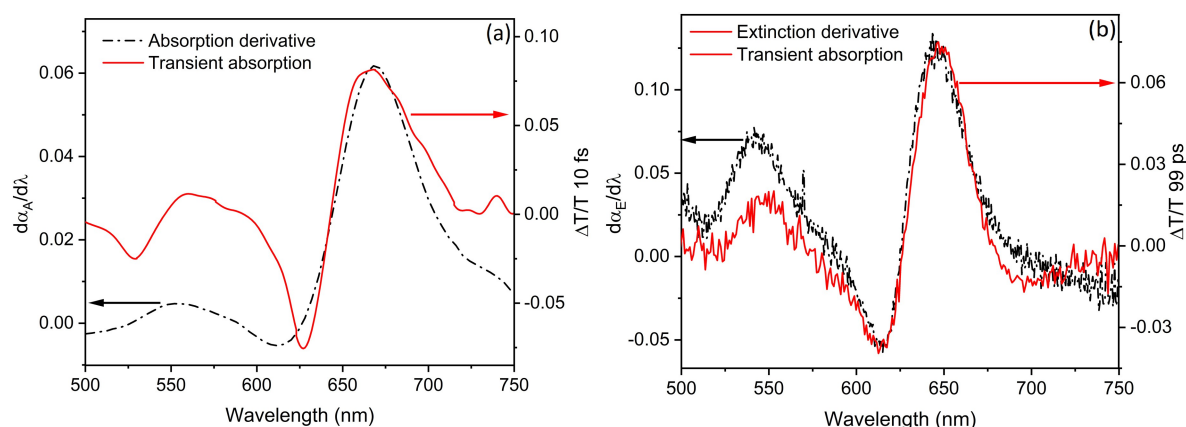


Figure 3. (a) A comparison plot of the short time (~ 10 fs, red solid line) experimental transient transmission ($\frac{\Delta T}{T}$) and absorption derivative ($\frac{d\alpha_{\lambda}}{d\lambda}$) of steady-state signal (dash-dotted black line) calculated using Equation 1 of WS_2 NPs. (b) A comparison plot of the long time (~ 99 ps, black solid line) experimental transient transmission ($\frac{\Delta T}{T}$) and the extinction derivative ($\frac{d\alpha_{\lambda}}{d\lambda}$) of steady-state signal (dash-dotted black line) calculated using Equation 2 of WS_2 NPs.

derivatives (Eq. 1, 2) with the $\Delta T/T$ spectra provides immediate assignment of the short- and long-delay processes. The results of the spectra comparison (Figure 3) infer that for the short delay times, the photophysical process is guided by the excitonic absorption, whereas for the long delay times, the process is controlled by polaritonic scattering. Furthermore, the matching of the derivatives with the ultrafast profile at short- and long-delay times reveals that the temporal dynamics of the quasi-systems strongly depend on the state of their coupling.

To comprehend the dynamics of exciton-polariton coupling, we consider the spectral shift and the change in spectral width observed in the transient absorption spectra of the dispersed WS_2 NP. (Figure 2b) These phenomena are not prevalent in pump-probe spectroscopy of molecules and semiconductors, yet they occur in WS_2 nanostructures due to many-body effects.^[18a,c,35] The blue shift of the PB and PA and the change in their spectral width can be considered as shifts of an individual exciton.^[36] Considering the spectral feature of the transitions as Gaussian, the transient signals from pump-probe spectroscopy can be expressed as the difference of the transmission in the presence and absence of the pump. (Eq. 3)

$$\Delta T(\lambda, t) = a_e(t) \exp \left[- \left(\frac{\lambda - \lambda_0 - \Delta\lambda(t)}{\gamma + \Delta\gamma(t)} \right)^2 \right] - a_g(t) \exp \left[- \left(\frac{\lambda - \lambda_0}{\gamma} \right)^2 \right] \quad (3)$$

where a , λ_0 , and γ are the amplitude, peak position of the exciton transition, and spectral width, respectively. The subscripts g and e represent the ground state and the excited state, respectively. The pre-exponential factors (a_e and a_g) indicate the temporal population for the excited and ground state. The shifts in spectral position and width from the steady-state values are denoted as $\Delta\lambda$ and $\Delta\gamma$, respectively. These fitting

parameters are varied to obtain the best fit of $\Delta T(\lambda, t)$ to the measured $\Delta T/T$. The time-dependent shifts of $\Delta\lambda$ and $\Delta\gamma$ are the indicators of the bandgap renormalization and the distribution of the excited electrons.^[18a]

Figure 4a represents the comparison between measured and the fitted spectral evolution of the transient spectra $\Delta T/T$ at the different pump-probe delays. The photo-absorption (PA) states are observed at 662 nm and 556 nm and correspond to the components of A and B excitons, respectively. The prominent photo-bleach (PB) state at 625 nm corresponds to the component of A exciton. The decay time relaxations of an individual A and B excitons are 1.2 and 2.1 ps, respectively. These values were derived from the fitting parameter – spectral shift ($\Delta\lambda(t)$). (Figure 4b, Eq. 3) The A exciton decays faster than the B exciton due to stronger coupling with the cavity modes of the former. The dynamical nature of the spectral shift is apparent here, indicating the relaxation of the excitons to the coupled (polaritonic) state. The change in spectral width ($\Delta\gamma(t)$) further emphasizes the mechanism of the A and B excitons' relaxation into the coupled state. (Figure 4b, inset) Note that the spectral width is directly correlated with the coupling constant (g). The approach used for Eq. 3 assumes that the shift of spectral width is constant with time. However, from the poor linear fit presented in the inset of Figure 4b, it is evident that this approach is not sufficient to describe the nonlinear change in spectral width. Thus, we consider an additional model to account for the unusual coupling in WS_2 NP further.

In order to understand the individual dynamics of PB and PA processes of polaritons and excitons, the temporal evolution dynamics have to be explored in detail. Driving by this requirement, the dynamics of different states were extracted by fitting the decay transients. To fit the photo-excitation dynamics, we recall that the recorded differential transmission of temporal dynamics can be represented as $\Delta T(\lambda, t) = T_p(\lambda, t) - T_{np}(\lambda, t)$. Where T_p and T_{np} are the

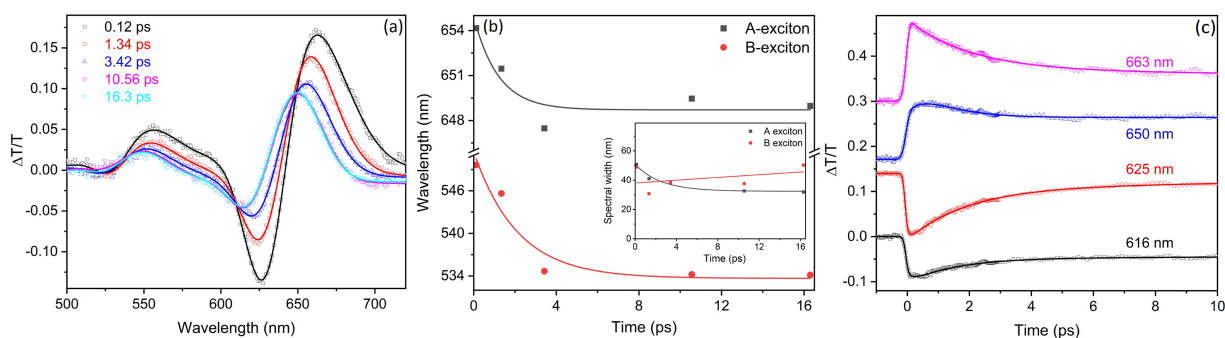


Figure 4. (a) Fitted plot of transient spectra ($\frac{\Delta T}{T}$) at different pump-probe delay presented in Figure 2. The symbols represent the experimental data points and the solid lines are the fitted curve using Eq. 3. (b) Plot of temporal variation spectral shift ($\Delta\lambda(t)$) of the A and B exciton with varied delay time, calculated from the fitting parameters of Eq. 3. The transition from A and B excitons to the polaritonic states can be realized from this shift. (Inset) Plot of temporal variation of spectral width ($\Delta\nu(t)$) with delay time. The spectral width of A exciton shows an exponential decay whereas B exciton shows a linear shift due to hybridization of upper and lower polaritons. (c) Transient dynamics of PB states and PA states of excitons and polaritons of WS_2 NPs for 97 μW pump power. The transients are fitted using Eq. 4 and presented as solid lines.

wavelengths (λ) dependent transmission signal at the different pump-probe delay (t) in the presence (p) and absence (np) of the pump laser, respectively. For each examined λ , the dynamics follow exponential decay or rise, thus the decay transients can be fitted as follows (Eq 4):^[37]

$$\frac{\Delta T(\lambda, t)}{T} = \sum_i a_i(\lambda, t) \exp\left(-\frac{t}{\tau_i}\right) \quad (4)$$

here a_i and τ_i are the pre-exponential factors (or the amplitude) and decay lifetime of the i^{th} decay process (a particular state at a specific λ). Due to the low signal-to-noise ratio, only the signal around the A exciton is considered. The comparison of the experimental and the fitted transient dynamics of PA and PB states, lifetimes, and amplitudes are presented in Figure 4c and S3. The free parameters of the fit results are presented in Table 1. There are two PA states, 662 nm for A exciton and 650 nm for polariton, and two PB states, 625 nm for A exciton and 616 nm for polariton. The fastest PA component ($\tau_{1,A}$) of the exciton A is due to coupling with the non-polaritonic state.^[32a] The PA of the polariton shows two distinct decay components. The longer component ($\tau_{2_{PB}}$) can be ascribed to the longer charge recombination processes or the effect of the strong cavity pumping.^[38] The long charge recombination process suggests that these polaritonic materials are suitable for photonic applications. The PB process presents two decay

components for the excitons, whereas the polaritons show a rise component along with two decay components. The rise component of the polaritons is induced by the coupling of the cavity modes to the excitons. The decay times can be assigned to the recombination processes.^[39] The result of the fitted decay dynamics reveals that both: the excitons and the polaritons have more than one lifetime. This finding suggests the existence of multiple coupled states associated with the exciton-polariton decays.

To understand the fascinating coupling dynamics, the experimental results of power-dependent dynamics were analyzed using the time-dependent coupling model.^[40] Here the exciton density in the excited state is considered to be proportional to the pump fluence. Therefore, the polariton density also increases with the pump power. The population of polaritons depends on the coupling constant between the exciton and the cavity modes. Thus, the polariton density also changes with time. However, the coupling between the exciton and the cavity shows time-dependent coupling and depends on the pump fluence.^[35b] The dynamical equations of these interacting systems are presented in Equation 5 a–c.^[40]

$$\frac{dN_{exc}(t)}{dt} = -k_1 N_{exc}(t) - g(t) N_{exc}(t) - \gamma N_{exc}^2(t) + I(t) \quad (5a)$$

Table 1. The summary of the fitting parameters of temporal dynamics presented in Figure 4b. The longer lifetime of the polaritonic states implies the longer recombination rate, the stability of the charged states.

		τ_1 (ps)	τ_2 (ps)	τ_3 (ps)
PA of the A exc.	662 nm	0.02 (67%)	2.04 (21%)	99.8 (12%)
PA of the polariton	650 nm	0.16	$> 10^4$	–
PB of the A exc.	616 nm	–0.18 (rise component)	1.6	233.1
PB of the polariton	625 nm	2.0	24.3	–

$$\frac{dN_P(t)}{dt} = -k_2 N_P(t) + g(t) N_{exc}(t) \quad (5b)$$

$$\frac{dg(t)}{dt} = \beta I_0 N_{exc}(t) (1 - e^{-k_{12}t}) e^{-k_3 t} \quad (5c)$$

Here N_{exc} , N_P and g represent the population density of excitons and polaritons and the coupling strength, respectively. I_0 represent the pump fluence (corelated to power). The constants k_1 and k_2 are the intrinsic decay of the exciton and polariton density, respectively. The constant k_{12} determines the strength of spatial coupling between exciton and cavity to form the polaritonic states. The increase in polariton density is controlled by the temporal coupling strength. The effect of the pump fluence on the dynamics of the coupling was modeled using Equation 5 d. Here $I(t)$ is the pump profile (pump shape) which is corelated to the intensity of an ultrafast pulsed electromagnetic source and can be considered as follows:^[41]

$$I(t) = \sqrt{\frac{4 \ln(2)}{\pi}} \frac{(1-R)\alpha I_0}{t_p} \exp\left[-4 \ln(2) \left(\frac{t-2t_p}{t_p}\right)^2\right] \quad (5d)$$

where R , α , and t_p are reflectance, absorbance, and pulse width, respectively. In this model, the coupling strength is not fixed but rather evolves with time. The temporal coupling of the excitons to the cavity modes infers the spatial dynamics of excitons and polaritons.^[42] Due to the low signal-to-noise ratio, only the interactions between the A exciton and the cavity mode are considered here.

The exciton decay and the formation of polariton due to the temporal coupling of exciton and the cavity modes is presented in Figure 5a for the pump fluence of 97 μJ and 26 μJ (inset). Using the temporal coupling approach, we learn that the saturation time of the polariton strongly depends on the pump fluence. Namely, the coupling strength of cavity and

exciton is much higher with pump power. The saturation time of the polariton is longer at lower pump fluence (I_0), and the cavity modes are more pronounced at higher I_0 . The dynamics of exciton and the polariton, and the transient transmission spectra at different pump power, are shown in Figure S4, 5. Figure 5b presents the evolution of the coupling strength (g) as a function of pump fluence at several delay times. For a shorter delay time, g linearly increases with the increase in the pump fluence. For longer delay times, the change in g is nonlinear and approaches saturation (constant value). Another insight drawn from the developed temporal coupling model is that at shorter delays, due to the low coupling strength only the excitonic behavior prevails. Thus, as the pump fluence increases, g increases, and the exciton decays into polariton much faster. For longer delay times, the dynamics are guided by polariton as the g becomes saturated.

Conclusions

In this work, we have reported on the ultrafast nonequilibrium light-matter interaction in WS_2 nanoparticles in aqueous dispersion, providing a time-dependent study of the coupled states formation between exciton resonances and an intrinsic cavity mode. We have shown that the simplistic comparison of the steady-state absorbance and extinction derivatives with the $\Delta T/T$ spectra provides an instantaneous assignment of the short- and long-delay decay processes. For short delay times (~ 0.3 ps), the transient spectra are related to the derivative of the absorbance while at long delay time (~ 100 ps) it is related to the derivative of the extinction. There is, for the short delay times, the light-matter interaction is guided by the excitonic absorption, whereas for the long delay times, the process is controlled by polaritonic scattering. In over words, the

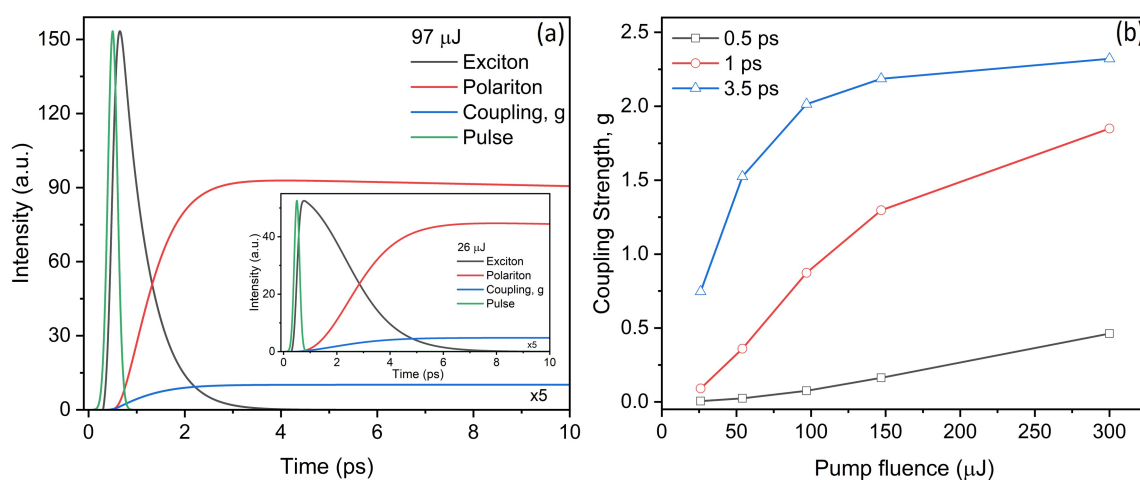


Figure 5. (a) The dynamics of exciton, polariton and the temporal coupling of exciton-cavity modes at the pump fluence of 97 μJ and 26 μJ (inset). The coupling strength is amplified (x5) for the presentation. (b) The pump-fluence dependence of coupling strength at different delay time. Note the nonlinear relation of coupling strength with pump fluence and the delay time.

Research Article

formation of EPs in WS₂ NPs is not instantaneous but a gradual process that occurs only after several ps.

We find an additional indication of the temporal nature of polariton formation when we observe the blue shift and broadening of the maxima in the transient spectra ($\Delta T/T$) at the different pump-probe delays. By expressing the transient signals as the difference of the transmission in the presence and absence of the pump, we discover the nonlinear coupling (Δg) between excitonic and external mode and eminent transition from weak to strong coupling limit. The dynamical nature of the spectral shift indicates the relaxation of the excitons to the coupled (polaritonic) state. The change in spectral width is an additional indication of the relaxation mechanism of EPs, where A and B excitons decay into the coupled state. Also, we found that the A exciton decays faster than the B exciton due to stronger coupling with the cavity modes of the former. Using the results of the fitted decay dynamics, we determined the existence of multiple coupled states associated with the exciton-polariton decays.

To elucidate the dynamic nature of the EPs formation further, we modeled the time-dependent coupling of exciton and cavity modes using the phenomenological dynamics. We found that the developed model explains the nonlinear dynamical coupling as well as the effects of the pump fluence on the coupling strength. We find that the saturation time of the polariton is longer at lower pump fluence (I_0), while the cavity modes are more pronounced at higher I_0 . Thus, as the pump fluence increases, g increases, and the exciton decays into polariton much faster. Namely, the coupling strength of cavity and exciton increases as the pump power increases. For the longer delay times, the dynamics are guided by the polariton as the g becomes saturated.

Our findings shed light on the dynamic and non-linear phenomena of the coupling processes in EPs. The methods and models developed in this work can hereafter be utilized to guide the experimental observation of exciton-polariton formation and coupling evolution dynamics. Moreover, the obtained knowledge can be readily utilized in the field of TMDs polaritonics for exploring genuinely unique physical scenarios and exploiting these new phenomena in technology in areas such as nanoscale lasing, quantum optics, and nanomanipulation.

Experimental

Materials

The multiwall WS₂ fullerene-like nanoparticles (NPs) were synthesized according to the procedure reported by Tenne et al.^[27b] The synthesis was carried out at 840 °C using WO₃ as a precursor and the resulted NPs were annealed for 20 hours at 840 °C to remove the remaining oxide.^[27] The XRD pattern of the annealed sample is presented in ref.^[27] and shows ~2% remaining oxide after the annealing process. The average size of these NPs is 50 to 200 nm and the number of WS₂ shells

depends on the synthetic conditions. TEM and SEM analyses reveal that the WS₂ NPs are somewhat oblate (Figure 1a). The solutions for all the current measurements were prepared using purified water (Milli-Q RG, Millipore).

Steady-State Absorption and Extinction Spectra

UV–vis extinction measurements were carried out on a Cary-5000 spectrometer (Varian). Samples were prepared by adding 0.6 mg of the WS₂ NP into 9 ml of purified water. The mixture was shaken by hand and then sonicated twice for 1–3 min using an ultrasonic bath. All suspensions were measured using quartz cuvettes. Scanning electron microscope (SEM) and Transmission electron microscope (TEM) analyses demonstrate that the WS₂ NPs remain unaffected by this mild sonication procedure.

Decoupled absorption spectra, used to separate scattering and absorption processes from the total extinction spectra, were measured using an integrated sphere (Hamamatsu Quantaurus absolute QY system).^[43] This instrument directly measures the amount of absorbed light by placing the sample inside an integrating sphere. The system was calibrated using a sample with known absorbance to extract the optical absorbance. A calibration for counting the single-pass absorption photons was performed to avoid the full extinction which also includes photons that are scattered a few times before being detected.

Femtosecond Pump-Probe Spectroscopy

Femtosecond (fs) pump-probe spectroscopy was used to resolve the character of polaritonic features as a function of excitation time. Here, the setup is driven by an amplified Ti:sapphire laser (Coherent Libra 2) producing 4 W, 150 fs, 800 nm pulses at a 2 kHz repetition rate. To generate a single filament white light continuum used as a probe, a fraction of the pulse energy is focused in a 3 mm thick sapphire plate. Another fraction of the pulse energy was doubled in a second harmonic (SH) crystal, serving as the pump pulse. Pump and probe are non-collinearly focused on the sample. The transmitted probe spectrum is detected by a spectrometer that is working at the full 2 kHz repetition rate of the laser. The spectra ($\Delta T/T$) of the dispersed NP were recorded with a time resolution of 150 fs set by the cross-correlation of pump and probe pulses and sensitivity of $1-2 \times 10^{-5}$. With the OPA one can reach a higher time resolution of 100 fs. The fs pump-probe measurements were carried out for WS₂ NP dispersed in H₂O (0.15 mg per ml). The dispersions were sonicated twice for two minutes before the measurement itself. The excited sample was probed at varying delays by a white-light continuum, covering the visible-near infrared (400–800 nm) region.

Glossary for Abbreviations and Acronyms

NSs	nanostructures
NPs	fullerene-like nanoparticles
2D	two-dimensional
NTs	nanotubes
EPs	exciton-polaritons
PA	photo-induced absorption
Fs	femtosecond
PB	photo-bleach
<i>G</i>	coupling strength
Ps	picosecond
<i>I</i> ₀	pump fluence
TMDs	transition metal dichalcogenides

Acknowledgements

The authors gratefully acknowledge Eva A. A. Pogna and Prof. Giulio Cerullo (Department of Physics, Politecnico di Milano) for the pump-probe measurements. BV acknowledges funding provided by the Institute of Physics Belgrade, through the grant by the Ministry of Education, Science, and Technological Development of the Republic of Serbia and the Slovenian Research Agency through contract P1-0099.

Data Availability Statement

The data that support the findings of this study are available on request from the corresponding author. The data are not publicly available due to privacy or ethical restrictions.

References

- a) A. P. Alivisatos, *Science* **1996**, *271*, 933; b) K. J. Vahala, *Nature* **2003**, *424*, 839–846; c) R. K. Chang, A. J. Campillo, in *Advanced Series in Applied Physics*, Vol. 3, World scientific, **1996**, p. 448.
- L. Cao, J. S. White, J.-S. Park, J. A. Schuller, B. M. Clemens, M. L. Brongersma, *Nat. Mater.* **2009**, *8*, 643–647.
- J. Hu, C. R. Menyuk, *Adv. Opt. Photonics* **2009**, *1*, 58–106.
- a) N. Rivera, I. Kaminer, *Nat. Rev. Phys.* **2020**, *2*, 538–561; b) E. J. Dias, F. J. G. de Abajo, *Optik* **2021**, *8*, 520–531.
- P. Törmä, W. L. Barnes, *Rep. Prog. Phys.* **2015**, *78*, 013901.
- a) R. R. Chance, A. Prock, R. Silbey, in *Adv. Chem. Phys.*, Vol. 37 (Eds.: I. Prigogine, S. A. Rice), **1978**, p. 65; b) L. Novotny, *Am. J. Phys.* **2010**, *78*, 1199–1202.
- S. Haroche, in *Les Houches Summer School Session* (Ed.: J. D. e. al), Amsterdam: North Holland, **1992**, pp. 767–940.
- J. Bellessa, C. Bonnand, J. C. Plenet, J. Mugnier, *Phys. Rev. Lett.* **2004**, *93*, 036404.
- B. Munkhbat, D. G. Baranov, M. Stührenberg, M. Wersäll, A. Bisht, T. Shegai, *ACS Photonics* **2019**, *6*, 139–147.
- a) C. Weisbuch, M. Nishioka, A. Ishikawa, Y. Arakawa, *Phys. Rev. Lett.* **1992**, *69*, 3314; b) H. Gibbs, G. Khitrova, S. Koch, *Nat. Photonics* **2011**, *5*, 273–273; c) F. Tassone, F. Bassani, L. Andreani, *Phys. Rev. B* **1992**, *45*, 6023.
- a) E. P. T. Tyndall, *Phys. Rev.* **1923**, *21*, 162–180; b) A. Zak, L. Sallacan-Ecker, A. Margolin, M. Genut, R. Tenne, *NANO* **2009**, *04*, 91–98; c) E. Hossain, A. A. Rahman, R. D. Bapat, J. B. Parmar, A. P. Shah, A. Arora, R. Bratschitsch, A. Bhattacharya, *Nanoscale* **2018**, *10*, 16683–16691; d) M. Nath, A. Govindaraj, C. N. R. Rao, *Adv. Mater.* **2001**, *13*, 283–286.
- a) L. Yadgarov, B. Višić, T. Abir, R. Tenne, A. Y. Polyakov, R. Levi, T. V. Dolgova, V. V. Zubyuk, A. A. Fedyanin, E. A. Goodilin, T. Ellenbogen, R. Tenne, D. Oron, *Phys. Chem. Chem. Phys.* **2018**, *20*, 20812–20820; b) R. Friend, A. Yoffe, *Adv. Phys.* **1987**, *36*, 1–94; c) Q. H. Wang, K. Kalantar-Zadeh, A. Kis, J. N. Coleman, M. S. Strano, *Nat. Nanotechnol.* **2012**, *7*, 699–712; d) L. Yuwen, F. Xu, B. Xue, Z. Luo, Q. Zhang, B. Bao, S. Su, L. Weng, W. Huang, L. Wang, *Nanoscale* **2014**, *6*, 5762–5769.
- A. H. Castro Neto, F. Guinea, N. M. R. Peres, K. S. Novoselov, A. K. Geim, *Rev. Mod. Phys.* **2009**, *81*, 109–162.
- a) N. Levy, S. Burke, K. Meaker, M. Panlasigui, A. Zettl, F. Guinea, A. C. Neto, M. F. Crommie, *Science* **2010**, *329*, 544–547; b) D. Allan, A. Kelsey, S. Clark, R. Angel, G. Ackland, *Phys. Rev. B* **1998**, *57*, 5106.
- a) R. Coehoorn, C. Haas, R. De Groot, *Phys. Rev. B* **1987**, *35*, 6203–6206; b) H. Zeng, G.-B. Liu, J. Dai, Y. Yan, B. Zhu, R. He, L. Xie, S. Xu, X. Chen, W. Yao, X. Cui, *Sci. Rep.* **2013**, *3*, 1608.
- a) X. Liu, T. Galfsky, Z. Sun, F. Xia, E.-c. Lin, Y.-H. Lee, S. Kéna-Cohen, V. M. Menon, *Nat. Photonics* **2015**, *9*, 30–34; b) K. F. Mak, J. Shan, *Nat. Photonics* **2016**, *10*, 216–226; c) S. Dufferwiel, T. Lyons, D. Solnyshkov, A. Trichet, F. Withers, S. Schwarz, G. Malpuech, J. Smith, K. Novoselov, M. Skolnick, *Nat. Photonics* **2017**, *11*, 497–501.
- X. Liu, T. Galfsky, Z. Sun, F. Xia, E.-c. Lin, Y.-H. Lee, S. Kéna-Cohen, V. M. Menon, *Nat. Photonics* **2014**, *9*, 30.
- a) B. Višić, L. Yadgarov, E. A. A. Pogna, S. Dal Conte, V. Vega-Mayoral, D. Vella, R. Tenne, G. Cerullo, C. Gadermaier, *Phys. Rev. Res.* **2019**, *1*, 033046; b) S. S. Sinha, A. Zak, R. Rose-ntsveig, I. Pinkas, R. Tenne, L. Yadgarov, *Small* **2020**, *16*, 1904390; c) S. S. Sinha, L. Yadgarov, S. B. Aliev, Y. Feldman, I. Pinkas, P. Chithaiah, S. Ghosh, A. Idelevich, A. Zak, R. Tenne, *J. Phys. Chem. C* **2021**, *125*, 6324–6340; d) A. Sedova, B. Višić, V. Vega-Mayoral, D. Vella, C. Gadermaier, H. Dodiuk, S. Kenig, R. Tenne, R. Gvishi, G. Bar, *J. Mater. Sci.* **2020**, *55*, 7612–7623.
- a) B. Radisavljevic, A. Radenovic, J. Brivio, V. Giacometti, A. Kis, *Nat. Nanotechnol.* **2011**, *6*, 147–150; b) Q. Wang, L. Sun, B. Zhang, C. Chen, X. Shen, W. Lu, *Opt. Express* **2016**, *24*, 7151–7157; c) Z. Fei, M. E. Scott, D. J. Gosztola, J. J. Foley, J. Yan, D. G. Mandrus, H. Wen, P. Zhou, D. W. Zhang, Y. Sun, J. R. Guest, S. K. Gray, W. Bao, G. P. Wiederrecht, X. Xu, *Phys. Rev. B* **2016**, *94*, 081402; d) A. A. Murthy, Y. Li, E. Palacios, Q. Li, S. Hao, J. G. DiStefano, C. Wolverton, K. Aydin, X. Chen, V. P. Dravid, *ACS Appl. Mater. Interfaces* **2018**, *10*, 6799–6804; e) Y. Li, E. C. Moy, A. A. Murthy, S. Hao, J. D. Cain, E. D. Hanson, J. G. DiStefano, W. H. Chae, Q. Li, C. Wolverton, X. Chen, V. P. Dravid, *Adv. Funct. Mater.* **2018**, *28*, 1704863; f) F. Hu, Y. Luan, M. E. Scott, J. Yan, D. G. Mandrus, X. Xu, Z. Fei, *Nat. Photonics* **2017**, *11*, 356–360.
- a) R. Tenne, L. Margulis, M. Genut, G. Hodes, *Nature* **1992**, *360*, 444–446; b) M. Hershinkel, L. Gheber, V. Volterra, J. Hutchison, L. Margulis, R. Tenne, *J. Am. Chem. Soc.* **1994**, *116*, 1914–1917; c) Y. Feldman, E. Wasserman, D. Srolovitz, R. Tenne, *Science* **1995**, *267*, 222.
- a) Y. Golan, C. Drummond, M. Homyonfer, Y. Feldman, R. Tenne, J. Israelachvili, *Adv. Mater.* **1999**, *11*, 934–937; b) L. Rapoport, V. Leshchinsky, I. Lapsker, Y. Volovik, O. Nepomnyashchy, M. Lvovsky, R. Popovitz-Biro, Y. Feldman, R. Tenne, *Wear* **2003**, *255*, 785–793; c) R. Rosentsveig, A. Gorodnev, N.

- Feuerstein, H. Friedman, A. Zak, N. Fleischer, J. Tannous, F. Dassenoy, R. Tenne, *Tribol. Lett.* **2009**, *36*, 175–182; d) R. Rosentsveig, A. Margolin, A. Gorodnev, R. Popovitz-Biro, Y. Feldman, L. Rapoport, Y. Novema, G. Naveh, R. Tenne, *J. Mater. Chem.* **2009**, *19*, 4368–4374; e) J. Tannous, F. Dassenoy, I. Lahouij, T. Le Mogne, B. Vacher, A. Bruhács, W. Tremel, *Tribol. Lett.* **2011**, *41*, 55–64; f) L. Yadgarov, V. Petrone, R. Rosentsveig, Y. Feldman, R. Tenne, A. Senatore, *Wear* **2013**, *297*, 1103–1110.
- [22] a) C. Ballif, M. Regula, P. Schmid, M. Remškar, R. Sanjines, F. Levy, *Appl. Phys. A* **1996**, *62*, 543–546; b) L. Yadgarov, R. Rosentsveig, G. Leitus, A. Albu-Yaron, A. Moshkovich, V. Perfilyev, R. Vasic, A. I. Frenkel, A. N. Enyashin, G. Seifert, *Angew. Chem. Int. Ed.* **2012**, *51*, 1148–1151; *Angew. Chem.* **2012**, *124*, 1174–1177.
- [23] a) G. Seifert, H. Terrones, M. Terrones, G. Jungnickel, T. Frauenheim, *Phys. Rev. Lett.* **2000**, *85*, 146–149; b) G. Seifert, H. Terrones, M. Terrones, G. Jungnickel, T. Frauenheim, *Solid State Commun.* **2000**, *114*, 245–248.
- [24] a) G. L. Frey, S. Elani, M. Homyonfer, Y. Feldman, R. Tenne, *Phys. Rev. B* **1998**, *57*, 6666–6671; b) L. Scheffer, R. Rosentzveig, A. Margolin, R. Popovitz-Biro, G. Seifert, S. R. Cohen, R. Tenne, *Phys. Chem. Chem. Phys.* **2002**, *4*, 2095–2098.
- [25] a) F. Qin, W. Shi, T. Ideue, M. Yoshida, A. Zak, R. Tenne, T. Kikitsu, D. Inoue, D. Hashizume, Y. Iwasa, *Nat. Commun.* **2017**, *8*, 14465; b) Y. J. Zhang, T. Ideue, M. Onga, F. Qin, R. Suzuki, A. Zak, R. Tenne, J. H. Smet, Y. Iwasa, *Nature* **2019**, *570*, 349–353; c) Y. J. Zhang, M. Onga, F. Qin, W. Shi, A. Zak, R. Tenne, J. Smet, Y. Iwasa, *2D Mater.* **2018**, *5*, 035002.
- [26] R. Verre, D. G. Baranov, B. Munkhbat, J. Cuadra, M. Käll, T. Shegai, *Nat. Nanotechnol.* **2019**, *14*, 679–683.
- [27] a) Y. Feldman, G. Frey, M. Homyonfer, V. Lyakhovitskaya, L. Margulis, H. Cohen, G. Hodes, J. Hutchison, R. Tenne, *J. Am. Chem. Soc.* **1996**, *118*, 5362–5367; b) L. Rapoport, Y. Bilik, Y. Feldman, M. Homyonfer, S. Cohen, R. Tenne, *Nature* **1997**, *387*, 791–793; c) L. Rapoport, Y. Feldman, M. Homyonfer, H. Cohen, J. Sloan, J. Hutchison, R. Tenne, *Wear* **1999**, *225*, 975–982.
- [28] G. L. Frey, R. Tenne, M. J. Matthews, M. S. Dresselhaus, G. Dresselhaus, *J. Mater. Res.* **1998**, *13*, 2412–2417.
- [29] C. Ballif, M. Regula, F. Levy, *Sol. Energy Mater. Sol. Cells* **1999**, *57*, 189–207.
- [30] C. F. Bohren, D. R. Huffman, *Absorption and Scattering of Light by Small Particles*, John Wiley & Sons, Hoboken, NJ, USA, **2007**.
- [31] a) B. Munkhbat, D. G. Baranov, M. Stührenberg, M. Wersäll, A. Bisht, T. Shegai, *ACS Photonics* **2019**, *6*, 139–147; b) L. Yadgarov, B. Višić, T. Abir, R. Tenne, A. Y. Polyakov, R. Levi, T. V. Dolgova, V. V. Zubyuk, A. A. Fedyanin, E. A. Goodilin, *Phys. Chem. Chem. Phys.* **2018**, *20*, 20812–20820; c) L. C. Flatten, Z. He, D. M. Coles, A. A. Trichet, A. W. Powell, R. A. Taylor, J. H. Warner, J. M. Smith, *Sci. Rep.* **2016**, *6*, 1–7.
- [32] a) V. Vega-Mayoral, D. Vella, T. Borzda, M. Prijatelj, I. Temptra, E. A. A. Pogna, S. D. Conte, P. Topolovsek, N. Vujicic, G. Cerullo, D. Mihailovica, C. Gadermaier, *Nanoscale* **2016**, *8*, 5428–5434; b) J. Wilson, A. Yoffe, *Adv. Phys.* **1969**, *18*, 193–335.
- [33] a) T. Arlt, S. Schmidt, W. Kaiser, C. Lauterwasser, M. Meyer, H. Scheer, W. Zinth, *Proc. Natl. Acad. Sci. USA* **1993**, *90*, 11757–11761; b) J. T. Kennis, A. Y. Shkuropatov, I. H. Van Stokkum, P. Gast, A. J. Hoff, V. A. Shuvalov, T. J. Aartsma, *Biochemistry* **1997**, *36*, 16231–16238.
- [34] C. Reichardt, *Chem. Rev.* **1994**, *94*, 2319–2358.
- [35] a) M. M. Brister, L. E. Piñero-Santiago, M. Morel, R. Arce, C. E. Crespo-Hernández, *J. Phys. Chem. Lett.* **2016**, *7*, 5086–5092; b) K. Tvrđy, P. A. Frantsuzov, P. V. Kamat, *Proc. Natl. Acad. Sci. USA* **2011**, *108*, 29–34.
- [36] A. Mondal, J. Aneesh, V. K. Ravi, R. Sharma, W. J. Mir, M. C. Beard, A. Nag, K. Adarsh, *Phys. Rev. B* **2018**, *98*, 115418.
- [37] R. Sharma, J. Aneesh, R. K. Yadav, S. Sanda, A. Barik, A. K. Mishra, T. K. Maji, D. Karmakar, K. Adarsh, *Phys. Rev. B* **2016**, *93*, 155433.
- [38] M. Zürich, H.-T. Chang, L. J. Borja, P. M. Kraus, S. K. Cushing, A. Gandman, C. J. Kaplan, M. H. Oh, J. S. Prell, D. Prendergast, C. D. Pemmaraju, D. M. Neumark, S. R. Leone, *Nat. Commun.* **2017**, *8*, 15734.
- [39] K. E. Knowles, M. D. Koch, J. L. Shelton, *J. Mater. Chem. C* **2018**, *6*, 11853–11867.
- [40] A. Stokes, A. Nazir, *Phys. Rev. Res.* **2021**, *3*, 013116.
- [41] J. K. Chen, D. Y. Tzou, J. E. Beraun, *Int. J. Heat Mass Transfer* **2006**, *49*, 307–316.
- [42] Note: The nonlinear Auger effects only for very high pump fluence can be considered by the parameter γ , but can be neglected for $97 \mu\text{J}$. The higher order polaritonic modes are beyond the scope of the article.
- [43] K. Suzuki, *Nat. Photonics* **2011**, *5*, 247.

Manuscript received: November 20, 2021
 Revised manuscript received: January 20, 2022
 Version of record online: February 18, 2022

Subject: [Nanomaterials, IF 5.076] Paper Promotion —Editor's Choice

From: "olivia.sun@mdpi.com" <olivia.sun@mdpi.com>

Date: 23/09/2021, 16:46

To: bojana.visic@ipb.ac.rs

CC: nanomaterials@mdpi.com

Dear Dr. Visic ,

It is our pleasure to inform you that your recently published paper in Nanomaterials has so far proven quite popular, having to date been viewed 453 times and downloaded 340 times.

As you might already be aware, our Editorial Board recently created a new section called "Editor's Choice". The purpose of this section is to promote papers which we believe are of considerable value to the scientific community, and we are pleased to share with you that your paper has been selected to be added to this section. You can view your paper at the following link:

https://www.mdpi.com/journal/nanomaterials/editors_choice
10.3390/nano11081985

This will help your paper to attract even more attention than it already has and reach an even wider audience.

Allow us to take this opportunity to thank you for choosing to publish with us. It is papers like yours that contribute to our journal's continued growth and success, and you are of course always welcome to submit new works for peer review and rapid publication in Nanomaterials.

We wish you all the best in your research and look forward to further collaboration. Please feel free to contact us with any questions.

--

Best Regards,

Ms.Olivia Sun , M.Sc.

Special Issue Editor

[Email:olivia.sun@mdpi.com](mailto:olivia.sun@mdpi.com)

Nanomaterials (IF: 5.076, <http://www.mdpi.com/journal/nanomaterials>)

Twitter: @Nano_MDPI

Nanomaterials 2021 Young Investigator Awards

<https://www.mdpi.com/journal/nanomaterials/awards>

3rd International Online-Conference on Nanomaterials

<https://iocn2021.sciforum.net/>

Companion journal: Nanomanufacturing

<https://www.mdpi.com/journal/nanomanufacturing>

MDPI Branch Office, Beijing

Floor 4, Building 7, Yard 13, Huayuan Rd, Haidian District, 100088 Beijing, China

[E-Mail:erika.zhao@mdpi.com](mailto:erika.zhao@mdpi.com)

Tel.: +86 10 6280 0830

MDPI

Postfach, CH-4020 Basel, Switzerland

Office: St. Alban-Anlage 66, 4052 Basel, Switzerland

<http://www.mdpi.com/>

Disclaimer: MDPI recognizes the importance of data privacy and protection. We treat personal data in line with the General Data Protection Regulation (GDPR) and with what the community expects of us. The information contained in this message is confidential and intended solely for the use of the individual or entity to whom they are addressed. If you have received this message in error, please notify me and delete this message from your system. You may not copy this message in its entirety or in part, or disclose its contents to anyone.

Editorial

Jaroslav Drellich

Department of Materials Science and Engineering, Michigan Technological University, Houghton, MI, USA

Ludmila Boinovich

A.N. Frumkin Institute of Physical Chemistry and Electrochemistry, Russian Academy of Sciences, Russia

Ziqi Sun

Queensland University of Technology, Brisbane, Australia

We are delighted to report another increase in the journal impact factor for *Surface Innovations*, which rose from 2.845 in 2020 to 3.016 this year. This is the fourth year in a row that the journal has experienced an increase in its impact factor as demonstrated in Figure 1.

The top three most-cited papers that contributed to this year impact factor include:

1. M.R. Derakhshandeh, M.J. Eshraghi, M.M. Hadavi, M. Javaheri, S. Khamseh, M.G. Sari, P. Zarrintaj, M.R. Saeb, and M. Mozafari, Diamond-like carbon thin films prepared by pulsed-DC PE-CVD for biomedical applications, *Surface Innovations* 6(3), 2018, 167–175.
2. M.R. Derakhshandeh, M.J. Eshraghi, M. Javaheri, S. Khamseh, M.G. Sari, P. Zarrintaj, M.R. Saeb, and M. Mozafari, Diamond-like carbon-deposited films: a new class of biocorrosion protective coatings, *Surface Innovations* 6(4-5), 2018, 266–276.
3. M. Sadeghi-Kiakhani, S. Khamseh, A. Rafie, S.M.F. Takieh, P. Zarrintaj, and M.R. Saeb, Thermally stable antibacterial wool fabrics surface-decorated by TiON and TiON/Cu thin films, *Surface Innovations* 6(4-5), 2018, 258–265.

We would like to take this opportunity to express our appreciation to Professors Masoud Mozafari, and Mohammad Reza Saeb for submitting the above-listed quality leading contributions on cutting-edge research to *Surface Innovations*. These papers serve as examples of quality that the journal seeks in every new submission.

We also thank all other contributors who submitted manuscripts to *Surface Innovations*, to external reviewers for their hard voluntary work and their valuable comments, and to everyone who reads and cites the *Surface Innovations* papers.

The number of submissions continues to rise, allowing us to be more selective in choosing contributions that are more appealing to innovators. Additionally, as a result of the impact of the growing pool of submissions, the publisher has decided to expand the content of the journal from 5 to 6 issues in 2022. We hope to fill the additional issue with interesting reports on surface and interfacial innovations and discoveries.

In this closing issue of 2021 we offer seven original research reports on antimicrobial coating, magnetic membranes,

photocatalytic nanoparticles, the use of iron phosphide as an energy-storage material, low-reflectivity coating for surgical instrumentation, inhibitor of corrosion, and the use of expired medication in lithium-based batteries.

In the first contribution, selected as the feature article for this issue, Centa *et al.* (2021) describe a novel active nanostructured antimicrobial composite coating made of poly(vinylidene fluoride-co-hexafluoropropylene) and polyvinylpyrrolidone as a matrix and molybdenum trioxide nanowire as a filler. The antimicrobial activity of the coating is demonstrated against Gram-positive and Gram-negative bacteria, yeasts, and molds. This novel nanocomposite coating is especially appealing for contact surfaces as it is activated by moisture, preventing colonization of the surface by microorganisms.

Polymeric magnetic membranes are used in cell culture studies to mediate and investigate the behavior of cells. In a new contribution, the research team from Turkey demonstrates fabrication of magnetic polydimethylsiloxane membranes with uniformly distributed embedded magnetite particles. Superparamagnetic magnetite particles with a diameter of 6–10 nm were synthesized using iron (II) chloride tetrahydrate and iron (III) chloride hexahydrate, and then homogenized uniformly into a silicone elastomer with its curing agent. Such fabricated chemical agent-free membranes were successfully tested for osteoblast cell proliferation and morphology studies.

Silver chloride surface doped with silver (Ag@AgCl) is a plasmonic photocatalyst that acts within the visible-light range and can be used to degrade hazardous organics from water and wastewater. A team of researchers from China invented a novel simple method of synthesizing Ag@AgCl nanoparticles with dimensions of 40–100 nm using silver nitrate and lithium chloride solutions and additions of dimethylacetamide and polyvinylpyrrolidone. The photocatalytic activity of synthesized nanoparticles is exhibited through degradation tests of methyl orange.

Sodium ion-batteries are considered a high specific energy, low cost and high safety alternative to current lithium ion-batteries, if the large diffusion resistance of the sodium ions between the cathode and the anode is significantly reduced. Therefore, current research in the field of sodium ion batteries concentrates heavily on development of new electrode materials such as transition metal phosphides. The research team from Zhengzhou University

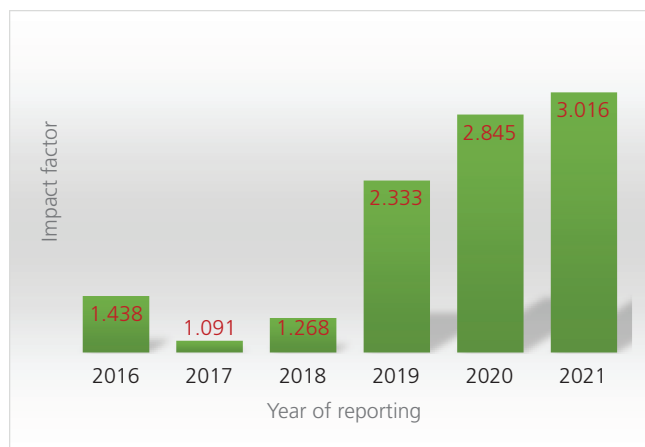


Figure 1. Impact factor for *Surface Innovations*

in China describes a unique composite electrode made of a hollow sea-urchin-like iron phosphide on a carbon substrate (FeP@C). This novel electrode material, with high integrity and cycling performance, effectively alleviates volume expansion during sodium ion intercalation and demonstrates high electrical conductivity.

High surface reflectivity of surgical instrumentation that reduces the surgeons' field of vision during interventional procedures is a common problem in the medical field and dentistry. In a new paper, researchers from Colombia tackle this challenge by depositing a low-reflectivity titanium aluminum nitride (TiAlN) coating on stainless steel using the direct-current magnetron sputtering technique. The study demonstrates that the columnar grain morphology of a TiAlN coating not only reduces reflectivity of the surface but also improves the corrosion resistance of stainless steel used for manufacturing surgical and dental instruments.

In the next contribution, an international China-USA team describes the corrosion inhibition performance of an imidazoline quaternary ammonium salt (IM) and octylphenol polyoxyethylene ether (OP) to combat carbon dioxide corrosion of pipeline steel in a sodium chloride solution. The study shows that the mixture of IM and OP molecules promote the formation of a thick, compact adsorption inhibitor layer, which performs significantly better than

when each material is applied separately, revealing synergistic inhibition performance. Fundamental studies also revealed that the IM-OP mixture enhanced interactions between inhibitor molecules and the metal surface, with OP promoting electrons to the metal and IM molecules accepting electrons from the metal surface.

In the last contribution to this issue, the research team led by Prof. Hou from Kunming University of Science and Technology describes their newest invention in their program of utilization of medical waste materials. They converted expired aminocaproic acid, commonly used in the treatment of acute bleeding due to elevated fibrinolytic activity, to zinc aminocaproate with mint-leaf-like flower morphology structures. Fabricated electrodes decorated with these zinc aminocaproate flowers exhibit high electrochemical lithium-storage performance with significant reversible discharge specific capacities.

We are looking forward to your feedback on the content of this issue, as well as other issues of *Surface Innovations*, and we encourage you to submit your exciting new reports on discoveries and innovations.

REFERENCES

1. Gradišar Centa U, Sterniša M, Višić B *et al.* (2021) Novel nanostructured and antimicrobial PVDF-HFP/PVP/MoO₃ composite. *Surface Innovations* **9(5)**: 256–266, <https://doi.org/10.1680/jsuin.20.00073>.
2. Erenay B, Garipcan B and Odabaş S (2021) Fabrication of homogeneous magnetic PDMS membranes to mediate cell behavior. *Surface Innovations* **9(5)**: 267–276, <https://doi.org/10.1680/jsuin.20.00085>.
3. Guo X, Mahmud S, Zhang X, Yu N and Faridul Hasan KM (2021) One-pot green synthesis of Ag@AgCl nanoparticles with excellent photocatalytic performance. *Surface Innovations* **9(5)**: 277–284, <https://doi.org/10.1680/jsuin.20.00089>.
4. Liu X, Zhang W, Zhong S *et al.* (2021) Hierarchical carbon-coated FeP derived from FeOOH with enhanced sodium-storage performance. *Surface Innovations* **9(5)**: 285–292, <https://doi.org/10.1680/jsuin.20.00083>.
5. Mejia VHD, Echavarría AM and Bejarano GG (2021) Detailed study of the electrochemical behavior of low-reflectivity TiAlN coatings. *Surface Innovations* **9(5)**: 293–307, <https://doi.org/10.1680/jsuin.20.00079>.
6. Han P, Wang X, Yang X *et al.* (2021) Synergistic effect of inhibitor mixture based on enhanced electron transfer. *Surface Innovations* **9(5)**: 308–316, <https://doi.org/10.1680/jsuin.20.00095>.
7. Hou H, Lan J, Yao Y *et al.* (2021) The recycling of expired aminocaproic acid injection for mint-leaf-like zinc aminocaproate. *Surface Innovations* **9(5)**: 317–323, <https://doi.org/10.1680/jsuin.21.00005>.

9-10 June 2022, Institute of Physics Belgrade

<http://strainedfesc.ipb.ac.rs/workshop-in-strongly-correlated-electron-systems/>

WORKSHOP IN STRONGLY CORRELATED ELECTRON SYSTEMS

Special focus of the conference will be devoted to Iron-chalcogenide superconductors and research performed during StrainedFeSC project.

"Workshop in strongly correlated electron systems" will be held in honor of Academician Zoran V. Popovic.

TOPICS

- Strongly correlated materials
- Iron-chalcogenide superconductors
- Layered and (quasi)2D materials
- Inelastic Light Scattering experiments for strongly correlated materials
- Spin-Orbit Coupled systems
- Strong Correlations on the Nanoscale
- Quantum Magnetism
- Unconventional Superconductivity
- Computational and analytical techniques for condensed matter systems
- Quantum phases and critical phenomena

INVITED SPEAKERS

Dr Alberto Pomar
Dr Rudi Hackl
Dr Milorad Milošević
Dr Qingming Zhang
Dr Jonas Bekaert
Dr Darko Tanasković
Dr Milos Radonjić
Dr Nenad Vukmirović
Dr Borislav Vasić
Dr Luka Pirker
Dr Marko Opačić
Dr Efthymios Liarokapis

Dr Valentin Ivanovski
Dr Rajdeep Adhikari
Dr Bojana Višić
Dr Jelena Mitrić
Dr Božidar Nikolić
Dr Novica Paunović
Dr Snežana Lazić
Dr Nenad Lazarević
Dr Jelena Pešić

....more to confirm

ORGANIZERS

Dr Nenad Lazarević
Dr Jelena Pešić
Dr Borislav Vasić
Dr Ana Milosavljević
Dr Sanja Đurđić Mijin
MSc Andrijana Šolajić

This workshop is supported by the Science Fund of the Republic of Serbia under the grant number 6062656 at Institute of Physics Belgrade Serbia.



WORKSHOP IN STRONGLY CORRELATED ELECTRON SYSTEMS,
BELGRADE JUNE 9–10, 2022

CONFERENCE PROGRAMME

Thursday, June 9, 2022

10⁰⁰ – 10³⁰ Welcome speech by the director of Institute of Physics Dr. Aleksandar Bogojević

10³⁰ – 11⁰⁰ Honorary speech, Zoran V. Popović, *Serbian Academy of Sciences and Arts, Belgrade, Serbia*

11⁰⁰ – 11³⁰ **Raman scattering study of the FeSe_{1-x}S_x**, Nenad Lazarević, *Institute of Physics Belgrade, University of Belgrade, Belgrade, Serbia*

11³⁰ – 12⁰⁰ **Light scattering in Fe pnictides and chalcogenides**, Rudi Hackl, *IFW Dresden, Dresden, Germany*

12⁰⁰ – 12³⁰ **Spin-lattice correlations at elevated temperatures in EuTiO₃**, Efthymios Liarokapis, *Department of Physics, National Technical University of Athens, Greece*

LUNCH BREAK

14⁰⁰ – 14³⁰ **Symmetries of layered structures**, Božidar Nikolić, *NanoLab, Faculty of Physics, University of Belgrade, Belgrade, Serbia*

14³⁰ – 15⁰⁰ **Nanoscale resistive switching in iridates and manganites**, Borislav Vasić, *Center for Solid State Physics and New Materials, Institute of Physics Belgrade, Serbia*

15⁰⁰ – 15³⁰ **Interplay of anomalous Hall angle and magnetic anisotropy in ferromagnetic topological crystalline insulator thin films**, Rajdeep Adhikari, *Institut für Halbleiter-und-Festkörperphysik, Johannes Kepler University, Linz, Austria*

15³⁰ – 16⁰⁰ **First Principle study of Evolution of Vibrational Modes of FeSe Under Uniaxial Strain**, Jelena Pešić, *Center for Solid State Physics and New Materials, Institute of Physics Belgrade, Serbia*

16⁰⁰ – 16³⁰ **Steps towards ab-initio predictions of electron mobility in materials with strong electron-phonon interaction**, Nenad Vukmirović, *Institute of Physics Belgrade, University of Belgrade, Belgrade, Serbia*

COFFEE BREAK

16⁴⁵ – 17¹⁵ **Infrared and Raman Study FeGa₃**, Darko Tanasković, *Institute of Physics University of Belgrade, Belgrade, Serbia*

17¹⁵ – 17⁴⁵ **Effective Medium Theory in Maxwell Garnett Approximation for Structural and Optical Characterization of some Chalcogenide – based Semiconducting Nanomaterials**, Jelena Mitrić, *Institute of Physics University of Belgrade, Belgrade, Serbia*

17⁴⁵ – 18¹⁵ **Suppression of superconductivity and nematic order in FeSe_{1-x}S_x (0 ≤ x ≤ 1)**, Cedomir Petrovic, *Condensed Matter Physics and Materials Science Department, Brookhaven National Laboratory, Upton, USA*

WORKSHOP IN STRONGLY CORRELATED ELECTRON SYSTEMS,
BELGRADE JUNE 9–10, 2022

Friday, June 10, 2022

10⁰⁰ – 10³⁰ **A new family of Kitaev materials**, Qingming Zhang, *Lanzhou University, Institute of Physics, Chinese Academy of Sciences, Lanzhou, Gansu, China*

10³⁰ – 11⁰⁰ **Complex oxide heterostructures for efficient spin to charge conversion**, Alberto Pomar, *Instituto de Ciencia de Materiales de Barcelona, Barcelona, Spain*

11⁰⁰ – 11³⁰ **DFT+ Σ 2 method for electron correlation effects at transition metal surfaces and nano-devices**, Miloš Radonjić, *Institute of Physics Belgrade, University of Belgrade, Belgrade, Serbia*

COFFEE BREAK

11⁴⁵ – 12¹⁵ **Dynamic tuning of quantum light emission from GaN/InGaN nanowire quantum dots by surface acoustic waves**, Snežana Lazić, *Departamento de Física de Materiales, Instituto 'Nicolás Cabrera' and Instituto de Física de Materia Condensada (IFIMAC), Universidad Autónoma de Madrid, Madrid, Spain*

12¹⁵ – 12⁴⁵ **First-principles exploration of superconducting 2D materials for emerging quantum technologies**, Jonas Bekaert, *Condensed Matter Theory (CMT), Department of Physics & NANOlaboratory Center of Excellence, University of Antwerp, Antwerp, Belgium*

12⁴⁵ – 13¹⁵ **The electric field gradient at ⁵⁷Fe in Fe_{1- δ} Te₂**, Valentin N. Ivanovski, *Department of Nuclear and Plasma Physics, Vinca Institute of Nuclear Sciences, National Institute of the Republic of Serbia, University of Belgrade, Belgrade, Serbia*

LUNCH BREAK

15⁰⁰ – 15³⁰ **Nonlinear and dynamic behaviour of exciton-polariton coupling processes in WS₂ nanostructures**, Bojana Višić, *Institute of Physics Belgrade, University of Belgrade, Belgrade, Serbia, Solid State Physics Department, Jozef Stefan Institute, Ljubljana, Slovenia*

16⁰⁰ – 16³⁰ **Synthesis and characterization of ternary Van der Waals MoxWx-1S2 nanotubes for advanced field emission application**, Luka Pirker, *Condensed Matter Physics Department, Jozef Stefan Institute, Ljubljana, Slovenia, Department of Electrochemical Materials, J. Heyrovský Institute of Physical Chemistry, Praha, Czech Republic*

16³⁰ – 17⁰⁰ **Influence of magnetism and electron-phonon interaction on lattice dynamics of pure and Co-doped K_xFe_{2-y}Se₂ single crystals**, Marko Opačić, *Institute of Physics Belgrade, University of Belgrade, Belgrade, Serbia*

COFFEE BREAK

17¹⁵ – 17⁴⁵ **Suppression of inherent ferromagnetism in Pr-doped CeO₂ nanocrystal**, Novica Paunović, *Institute of Physics Belgrade, University of Belgrade, Belgrade, Serbia*

17⁴⁵ – 18¹⁵ **Fluctuating hexamer precursor to a two-stage electronic transition in RuP**, Emil Bozin, *Condensed Matter Physics and Materials Science Division, Brookhaven National Laboratory, Upton, USA*

18¹⁵ **Closing Ceremony**

Znanost prinaša rezultate. Ko opraviš meritve ali poskus, je rezultat jasen

Bojana Višić raziskuje nove nanomateriale in njihovo uporabo.



[Odpri galerijo](#)

Znanstvenik se ne sme trmasto držati svojih metod ali tehnik, stopiti mora tudi iz cone udobja in poskusiti nove stvari. FOTO: Blaž Samec/Delo

Najnovjše | Najbolj brano

- 12:04** **FOTOGALERIJA /**
Fotografije dneva (21. 3.)
 - 10:00** **ANTICA MARIJANAC / V**
razredu sem pozabila na vse težave zunanjega sveta
 - 09:42** **MARTINA NAVRATILOVA /**
Mislila je, da ne bo dočkala naslednjega božiča
 - 09:00** **KNJIGA / Vsaka kratka**
zgodba ima svoje lastno življenje
 - 08:50** **METKA PARAGI PROTI**
NLZOH / Preobrat v
primeru odpuščene mikrobiologinje
 - 08:43** **ODŠLA LEGENDA PLANICE /**
Umrli je Janez Gorišek
- [Več...](#)

Top novice





Saša Senica

11.08.2022 ob 09:00

POSLUŠAJTE



Čas branja: 6:31 min.

DELITE



Dr. **Bojana Višić** dela na Institutu Jožef Stefan, na odseku za fiziko trdne snovi, in na Inštitutu za fiziko v Beogradu.

Predstavite nam instrument, ki ga najpogosteje ali najraje uporabljate pri delu.

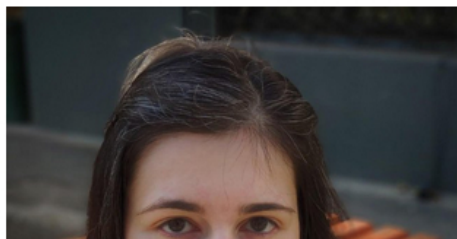
Osnova mojega raziskovanja je sinteza in karakterizacija nanomaterialov. Mislim, da ni veliko stvari, ki bi presegle moje navdušenje, ko sintetiziramo nov material in grem v temno mikroskopsko sobo ter postavim vzorec v komoro za vrstični ali transmisijski elektronski mikroskop, da si ga ogledam. Res lahko ure in ure mikroskopiram, ne da bi mi postalo dolgčas, čeprav nisem »prava« mikroskopistka, ampak le uporabnica mikroskopa.

Kako bi povprečno razgledanemu v največ sto besedah razložili, kaj raziskujete?

Moja znanstvena pot me je pripeljala v svet anorganskih nanodelcev, predvsem nanocev in nanožic. Med diplomskim in magistrskim delom sem jih proučevala kot teoretičarka, nato pa kot eksperimentalistka, ko sem se pridružila skupini prof. **Maje Remškar** kot doktorska študentka. Sintetizirati poskušamo nove nanomateriale, iščemo načine za optimizacijo sinteze, te materiale potem karakteriziramo z različnimi tehnikami, poleg tega pa raziskujemo, kako bi jih lahko uporabili v praktičnih aplikacijah, pa naj bo to v optiki, katalizi, kot del polimernih kompozitov ali celo v nanoelektromehaniki. Zame je najbolj zanimiv del raziskave karakterizacija, to je ugotavljanje stehiometrije nanocevke, kristalne strukture, razporeditve atomov, prisotnosti defektov in nečistoč, potem pa raziskava študija optičnih lastnosti.

Zakaj imate radi znanost?

Znanost prinaša rezultate. Ko opraviš meritev ali poskus, je rezultat jasen. Seveda ga lahko nato vse življenje poskušate razložiti in razumeti, ampak ni možnosti, da bi z njim manipulirali ali da bi nekdo trdil, da ste dobili nekaj drugega. Znanost sicer ni povsem črna-bela, ampak bližje temu ne moremo. Všeč so mi stvari, ki so logične.



Preobrat v primeru odpuščene mikrobiologinje



Istra letos ne bo deležna niti kapljice več



Dvoličnost koalicije, ki prisega na pravno državo



Umrli je Janez Gorišek

Mnenja



Damjan Kobal
Sabotaža (javnega) solstva



Dino Bauk
Pol mehkega č vredna bolečina



Blaž Podobnik
Multipolarnost kot spoštovanje različnosti



Boris Šuligoj
Mama jim je kupila traktorje

[Več...](#)

Kaj dobrega bi vaše delo lahko prineslo človeštvu?

Sem velika zagovornica načela *l'art pour l'art*, ampak za znanost. Do veliko prelomnih odkritij so se prebili znanstveniki, ki so enostavno raziskovali, ne da bi mislili na končno uporabo tega, kar počnejo. Zato mi ni všeč sodoben pristop k pridobivanju projektov in objavi člankov, ko si moraš že čisto na začetku izmisliti končni izdelek, to je povsem umetno. Menim, da negativni rezultati in poskusi, ki niso potrdili začetne hipoteze, prispevajo k zakladnici znanja in bi jih bilo treba objaviti. Kdo ve koliko ubogih študentov ta trenutek zapravlja čas za nekaj, kar so drugi že poskušali, namesto da bi porabili svoj čas in energijo za stvari, ki lahko prinesejo rezultate.



Bojana Vistić. FOTO: Osebni arhiv

Kdaj ste vedeli, da boste znanstvenica?

Sliši se kot kliše, ampak to sem vedela že od malega. Ko smo se v osnovni šoli prvič srečali s fiziko, je bila moja pot začrtana.

Kaj zanimivega poleg raziskovanja še počnete?

Po dveh podoktorskih projektih imam veliko prijateljev po vsem svetu. Tako imam zdaj vedno dober razlog za potovanje. Zelo rada tečem in upam, da bom lahko tekla tudi, ko bom že zelo stara.

Kaj je ključna lastnost dobrega znanstvenika?

Odprtost za novosti. Znanstvenik se ne sme trmasto držati svojih metod ali tehnik, stopiti mora tudi iz cone udobja in poskusiti nove stvari. Srečo imam, da sem bila vedno obkrožena s sodelavci, ki niso le odlični znanstveniki, ampak odlični ljudje, ki svoje znanje radi delijo in ga ne zadržujejo zase. Bistvo znanstvenika bi moralo biti deljenje odkritja.

Katero bo najbolj prelomno odkritje ali spoznanje v znanosti, ki bo spremenilo tok zgodovine v času vašega življenja?

Marsikaj bi rada vedela, vendar resnično upam, da bomo še v času mojega življenja razumeli, kaj je

Ne spreglejte



S toplotno črpalko do najučinkovitejšega načina ogrevanja doma



Ustanavljate podjetje? Veste, kje iskati podatke o podjetjih?



Investirajte preprosto – kjer koli in kadar koli



Nova vrsta zobnih vsadkov navdušuje tudi Slovence

temna energija.

Bi odpotovali na Mars, če bi se vam ponudila priložnost?

Instinktivno bi najprej rekla: »Seveda, kje se prijavim?« A če bolje premislim, sem prepričana, da bi na koncu raje ostala na Zemlji. Velika verjetnost je, da bi bilo potovanje enosmerno, tu pa bi še rada videla toliko stvari.

Na kateri vir energije bi stavili za prihodnost?

Karkoli bo, moralo bo biti zeleno. Spremeniti moramo način porabe energije, pa že zamujamo. Realno gledano bo šlo za hibrid med obnovljivimi viri energije, kot sta sonce in veter, in najverjetneje fuzijo. Upam, da kmalu.

S katerim znanstvenikom v vsej zgodovini človeštva bi šli na kavo?

Izredno me zanima zgodovina kvantne mehanike in kopenhavskega kroga **Nielsa Bohra**. Čeprav nisem zagovornica njihove interpretacije kvantne teorije, so ti znanstveniki živeli v najbolj zanimivem obdobju teoretične fizike. Niels Bohr je bil karizmatična in prepričljiva oseba. Z njim bi rada spila kavo, čeprav sem prepričana, da bi bil to prej monolog kot pogovor.

Katero knjigo, film, predavanje, spletno stran s področja znanosti priporočate bralcu?

Knjige **Seana Carrola**, enega vodilnih sodobnih kozmologov, njegov podkast Mindscape je moje obvezno ponedeljkovo poslušanje. Moja najljubša knjiga o temeljih in zgodovini kvantne mehanike je delo **Adama Beckerja** *What is Real? The Unfinished Quest for the Meaning of Quantum Physics*.

Česa ne vemo o vašem področju, pa bi nas presenetilo?

Anorganski nanodelci se komercialno najpogosteje uporabljajo kot dodatki v oljih za zmanjšanje trenja na velikih ladjah.

Hvala, ker berete Delo.

Brati več. Razumeti več. Vedeti več.